Creation and detection of majorana states

Rubbert, Sebastian

DOI
10.4233/uuid:e3e035b1-b9b9-4376-8a3c-45b4f37783d0

Publication date
2018

Document Version
Final published version

Citation (APA)
Rubbert, S. (2018). *Creation and detection of majorana states*. [Dissertation (TU Delft), Delft University of Technology]. https://doi.org/10.4233/uuid:e3e035b1-b9b9-4376-8a3c-45b4f37783d0

CREATION AND DETECTION OF MAJORANA STATES

CREATION AND DETECTION OF MAJORANA STATES

Dissertation

for the purpose of obtaining the degree of doctor
at Delft University of Technology
by the authority of the Rector Magnificus, Prof. dr. ir. T.H.J.J. van der Hagen,
chair of the Board for Doctorates
to be defended publicly on Friday 16th March 2018 at 15:00 o'clock

by

Sebastian RUBBERT
Master of Science in Physics, RWTH Aachen University, Germany
born in Engelskirchen, Germany.

This dissertation has been approved by the promotor and the copromotor.

Composition of the doctoral committee:

Rector Magnificus,	chairperson
Prof. dr. Y. Nazarov,	Delft University of Technology, promotor
Dr. A.R. Akhmerov,	Delft University of Technology, copromotor

Independent members:

Prof. dr. Y. M. Blanter,	Delft University of Technology
Prof. dr. F. Hassler,	RWTH Aachen University, Germany
Prof. dr. ir. A. Brinkman,	University of Twente
Dr. X. Waintal,	University of Grenoble Alps, CEA INAC PHELIQS, France
Dr. M. Titov,	Radboud University Nijmegen
Prof. dr. ir. L.M.K. Vandersypen,	Delft University of Technology, reserve member

This research was supported by the Netherlands Organization for Scientific Research (NWO/OCW), as part of the Frontiers of Nanoscience program, and an ERC Starting Grant.

Printed by: Gildeprint

Cover: "Majorana Fermion in the Fermi Sea" by Alexey Dryahlov © 2012, CC-BY-SA

Casimir PhD Series, Delft-Leiden 2018-07

ISBN 978-90-8593-339-7

An electronic version of this dissertation is available at
`http://repository.tudelft.nl/`.

CONTENTS

SUMMARY

Majorana bound states (MBS) have non-Abelian exchange statistics, which means exchanging the position of two MBS changes the state of the system. This attracted attention for multiple reasons: It is a quantum effect without a classical analogue, it introduces topology to condensed matter physics and the non-Abelian exchange processes allow quantum computing with intrinsic error protection.

For a long time research on MBS was purely theoretical, because there was no experimentally accessible idea how to create them. This changed with the appearance of a recipe combining conventional superconductivity, semiconductors and a magnetic field. Now such setups exist and their conductance indicates the successful creation of MBS, but challenges regarding their quality, conclusive detection and control remain. In this thesis I propose different strategies for avoiding open experimental problems when creating MBS, and identify new pathways for detecting them.

Most proposals for creating MBS are similar in two regards: They confine electrons to lower dimensional systems, for example a 1-dimensional wire, and they use magnetic field to couple to the electron spin. I start this thesis by developing a system where the magnetic field forces electrons onto cyclotron orbits, thereby spatially confining them without relying on the system's geometry. This leads to an increased resilience against imperfections.

Imperfections in real systems are not the only technical problem. One example is the combination of superconductivity and a magnetic field. Superconductors expel weak magnetic fields, while strong magnetic fields induce vortices in the superconductor which have a nonsuperconducting region in their core. In order to avoid these problems I turn to a completely different regime and develop a system that does not require a magnetic field to create MBS. Instead the role of the magnetic field is taken by a combination of supercurrents and spin-orbit coupling in the semiconductor.

Then I turn to the detection of MBS, which is always a competition between two goals: finding a unique signature only caused by MBS and relying on a simple setup. One well-established signature of MBS is single electron transport through a superconductor, because without MBS a superconductor only transports electrons in pairs. Of course single electron transport is not a unique signature at all: it happens in most conductors. That makes it hard to distinguish MBS from undesired side effects. I develop a setup that adds falsifiability to this signature. In addition to detecting single electron transport, my scheme allows to block it if it is due to MBS, therefore making MBS and a normal conduction channel distinguishable.

In the last part of my thesis I do not propose a system, but instead I analyze and simulate an unexpected outcome of an experiment. My colleagues were studying a driven superconducting resonator coupled to a Josephson junction (two superconductors separated by a short barrier) with the goal of using it to detect MBS. Completely unexpectedly

it turned out to be a high quality microwave laser. In a collaborative effort we explain this previously overlooked phenomenon.

SAMENVATTING

Majorana bound states (MBS) hebben niet-Abelse omwisselingsstatistiek, waarmee bedoeld wordt dat het omwisselen van de positie van twee MBS de toestand van het systeem verandert. Dit trok de aandacht om meerdere redenen: het is een quantumeffect zonder een klassieke analoog, het introduceert topologie in de vaste-stoffysica en de niet-Abelse omwisselingsprocessen bieden mogelijkheid voor quantumberekeningen met een intrinsieke bescherming tegen fouten.

Lange tijd was het onderzoek naar MBS uitsluitend theoretisch, omdat er geen experimenteel uitvoerbaar idee was om hen te creëren. Dit veranderde met de verschijning van een recept waarin conventionele supergeleiding, halfgeleiders en een magnetisch veld worden gecombineerd. Zulke opstellingen bestaan nu, en hun geleiding wijst op succesvolle creatie van MBS, maar uitdagingen wat betreft hun kwaliteit, onweerlegbare detectie en controle blijven bestaan. In deze dissertatie stel ik verschillende strategieën voor om openstaande experimentele problemen bij de creatie van MBS te ontwijken, en bepaal ik nieuwe manieren om hen te detecteren.

De meeste voorstellen voor het creëren van MBS komen in twee opzichten overeen: ze begrenzen elektronen in laag-dimensionale systemen, zoals een 1-dimensionale draad, en ze gebruiken een magnetisch veld om te koppelen aan de elektronspin. Ik begin deze dissertatie met het ontwikkelen van een systeem waarin het magnetisch veld de elektronen in cyclotronorbitalen dwingt waarbij ze ruimtelijk worden begrensd zonder dat de geometrie van het systeem hiervoor benodigd is. Dit resulteert in een toegenomen weerstand tegen onzuiverheden.

Onzuiverheden in echte systemen zijn niet het enige technische probleem. Een voorbeeld is de combinatie van supergeleiding en een magnetisch veld. Supergeleiders sluiten zwakke magnetische velden buiten, terwijl sterke magnetische velden vortexen opwekken in de supergeleider met een niet-supergeleidend gebied in hun kern. Om deze problemen te omzeilen beschouw ik een volledig verschillend regime en ontwikkel ik een systeem dat geen magnetisch veld nodig heeft om MBS te creëren. In plaats daarvan wordt de rol van het magnetisch veld overgenomen door een combinatie van superstromen en spin-baankoppeling in de halfgeleider.

Daarna richt ik me op de detectie van MBS, die altijd een competitie is tussen twee doelstellingen: het vinden van een uniek kenmerk uitsluitend veroorzaakt door MBS, en het kunnen gebruikmaken van een simpele opstelling. Eén algemeen erkend kenmerk van MBS is enkel-elektrontransport door een supergeleider, omdat zonder MBS elektrontransport in een supergeleider uitsluitend in paren plaatsvindt. Natuurlijk is enkel-elektrontransport geen uniek kenmerk: het vindt plaats in de meeste geleiders. Dat bemoeilijkt het onderscheiden van MBS en ongewenste bijeffecten. Ik ontwikkel een opstelling die falsificeerbaarheid toevoegt aan dit kenmerk. Aanvullend op het detecteren van enkel-elektrontransport biedt mijn schema de mogelijkheid het te blokkeren als het

veroorzaakt wordt door MBS, waarmee onderscheid kan worden gemaakt tussen MBS en een normaal geleidingskanaal.

In het laatste deel van mijn dissertatie maak ik geen voorstel voor een systeem, maar analyseer en simuleer ik in plaats daarvan een onverwachte uitkomst van een experiment. Mijn collega's bestudeerden een aangedreven supergeleidende resonator gekoppeld aan een Josephson-junctie (twee supergeleiders gescheiden door een smalle barrière) met als doel het te gebruiken om MBS te detecteren. Volledig onverwacht bleek het een hoogkwalitatieve microgolflaser te zijn. In een gezamelijke bijdrage leggen we dit tot nu toe over het hoofd geziene fenomeen uit.

1

INTRODUCTION

PREFACE

Topology in condensed matter physics [1–4] classifies Hamiltonians with a spectral gap into subgroups. Continuously transforming a Hamiltonian from one subgroup into that of another subgroup requires closing the spectral gap. As a physical consequence of these abstract classifications zero energy edge states arise between regions described by Hamiltonians of different subgroups. Majorana bound states (MBS) [5–7] are such topological edge states. The name expresses that it is locally bound and that it is represented by a Hermitian operator, hence a Majorana fermion.

Exchanging two MBS [8–10] does not multiply the wave function by a phase factor, but instead acts as a many-body operator. In systems with more than two MBS, this operator depends on the pair that exchanges its positions. This is different from an exchange of two fermions or two bosons, that only multiplies the wave function by an unobservable phase factor. The operators corresponding to the exchange of different pairs of MBS do not commute trivially, therefore giving rise to non-Abelian exchange statistics. In opposition to most systems with non-Abelian exchange statistics [11–15], MBS arise from non-interacting Hamiltonians and therefore are simpler to understand and to work with.

Non-Abelian exchange statistics are not only of academic interest, but they are also candidates for the implementation of fault tolerant quantum computation [16–18]. They can store quantum information that is protected against (local) noise. In addition to their advantages in storing data, non-Abelian exchanges may be used as an operation on the information stored in the system. As a main advantage over conventional systems, the exchange statistics in a certain kind of system does not depend on details (or on noise). Therefore, these gates would also be 'topologically protected' against errors. In the case of the MBS, the exchange statistics are represented by the Clifford gates, which only lack a CNOT-gate and a $\pi/8$-gate for universal quantum computation. Therefore, using MBS would allow building a quantum computer in which data storage and most gate types are topologically protected against errors.

1

CREATION OF MAJORANA BOUND STATES

KITAEV CHAIN

The first problem one faces about MBS is the question how they arise from a system of normal fermions. The simplest example of a system hosting MBS is the Kitaev chain [19], which is a 1-dimensional tight binding system, with spinless electrons and p-wave coupling of electrons and holes. The Hamiltonian is

$$H = \sum_{j=1}^{N} -t\left(a_j^\dagger a_{j+1} + a_{j+1}^\dagger a_j\right) - \mu\left(a_j^\dagger a_j + \frac{1}{2}\right) + \Delta a_j a_{j+1} + \Delta^* a_{j+1}^\dagger a_j^\dagger, \tag{1.1}$$

where t is the hopping amplitude, μ the chemical potential, Δ the p-wave coupling and N the number of sites.

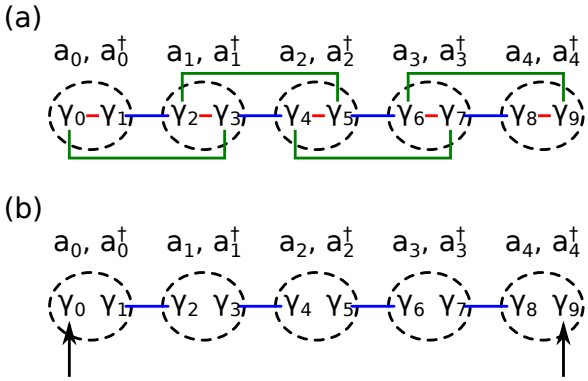

Figure 1.1: (a) A visual representation of Kitaev's Hamiltonian in Majorana basis (eq. 1.4). Each site denoted by the dashed ovals includes two Majorana operators γ_i. The chemical potential couples Majorana operators on the same site (red lines). The electron-hole coupling and the hopping, couple Majorana operators on different sites denoted by the blue and green lines. (b) A visual representation of the same Hamiltonian in the case $t = |\Delta|$ and $\mu = 0$. In this case only one type of the sketched couplings remains and the Majorana operators at the edges of the system are not coupled to any others; hence the system hosts MBS.

A transformation of the creation and annihilation operators to Majorana operators directly shows the MBS for one parameter choice. The transformation is

$$\gamma_{2j-1} = e^{i\theta/2} a_j + e^{-i\theta/2} a_j^\dagger, \tag{1.2}$$

$$\gamma_{2j} = -ie^{i\theta/2} a_j + ie^{-i\theta/2} a_j^\dagger, \tag{1.3}$$

where θ is the complex phase of Δ. In terms of these operators, the Hamiltonian reads

$$H = \frac{i}{2} \sum_{j=1}^{N} -\mu\gamma_{2j-1}\gamma_{2j} + (t + |\Delta|)\gamma_{2j}\gamma_{2j+1} + (-t + |\Delta|)\gamma_{2j-1}\gamma_{2j+2}. \tag{1.4}$$

In the case of $t = |\Delta|$ and $\mu = 0$ all Majorana operators, except for one at each edge, are coupled pairwise with the amplitude $(t + |\Delta|)$ (Fig. 1.1). Therefore, the quasi-particles in

the bulk have the energies $\pm(t+|\Delta|)$ and there is one zero energy eigenstate at each edge of the system. These zero energy states are MBS.

While it is straightforward to see zero energy edge states at $t=|\Delta|$ and $\mu=0$, they also exist for other parameter choices. Their existence is characterized by a topological invariant $I \equiv \text{sign}\big(\text{Pf}[iH(k=0)]\text{Pf}[iH(k=\pi)]\big)$, where Pf is the Pfaffian of the Hamiltonian in Majorana basis, $H(k)$ is the Hamiltonian subblock with fixed momentum k, and the momentum $k=\pi$ denotes the edge of the Brillouin zone. MBS arise at the edge of two systems with different topological invariants I. Since most natural systems (including vacuum) have $I=1$, we speak of systems hosting MBS if $I=-1$. Since the Pfaffian is not conserved under unitary transformations, the value of I is only meaningful in connection with the basis in which it was calculated. We assume the Majorana basis introduced in eq. 1.3. The definition of the topological invariant I allows us to calculate the parameter

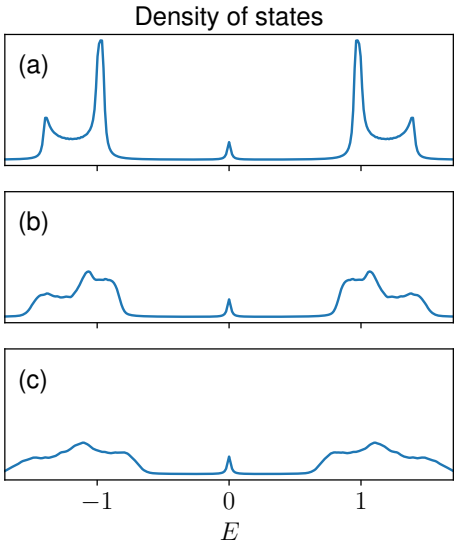

Figure 1.2: The density of states of a 50 site Kitaev chain with Lorentzian broadening to create continuous bands (a) without disorder, (b) with disorder and (c) with stronger disorder. The density of states is rearranged randomly since disorder shifts the energy levels. Only the peak at zero energy remains unchanged, since the edge states are symmetry protected zero energy modes and therefore do not respond to disorder.

regime where MBS arise

$$\begin{aligned} I &= \text{sign}\left(\text{Pf}\left(\begin{bmatrix} 0 & -\mu+2t \\ \mu-2t & 0 \end{bmatrix}\right)\text{Pf}\left(\begin{bmatrix} 0 & -\mu-2t \\ \mu+2t & 0 \end{bmatrix}\right)\right) \\ &= \text{sign}\left((-\mu+2t)(-\mu-2t)\right) \\ &= \begin{cases} 1, & \text{for } |\mu|>2|t|, \\ -1, & \text{for } |\mu|<2|t|. \end{cases} \end{aligned} \tag{1.5}$$

The values of the topological invariant show that in Kitaev's model MBS arise if $|\mu|<2|t|$.

Since MBS are topological edge states, they are symmetry protected zero energy states. More precisely, applying the particle-hole symmetry operator does not change them, therefore their energy E must fulfill $E = -E \Rightarrow E = 0$ if the system is particle-hole invariant. We illustrate the symmetry protection in a Kitaev chain with disorder, where the disorder randomly rearranges all energy levels, except for the energy of the MBS (Fig. 1.2).

CREATING MAJORANA BOUND STATES IN EXPERIMENTS

The path to experimentally realizable MBS is long and possibly not yet completed. While the Kitaev chain is helpful in understanding MBS better by introducing a minimal model, it is not meant as a proposal to create MBS in an experiment since it requires inaccessible elements such as unconventional superconductivity and spinless electrons. Similarly a related system, the 2-dimensional chiral p-wave superconductor [8] has yet to be demonstrated in an experiment, but it does help to understand the exchange statistics of MBS. In the development of MBS in experiments, one important step was the proposition to combine topological insulators with conventional superconductors [20]. This proposition demonstrates that unconventional superconductivity is not an unavoidable requirement for MBS. Later came the realization that a topological insulator is also not required, but a combination of conventional superconductivity induced into a semiconductor with spin-orbit interaction and a Zeeman splitting also allows the creation of MBS [21–24]. Since all these elements are experimentally accessible, this proposal sparked experimental efforts, which have already led to first signs of success [25–30].

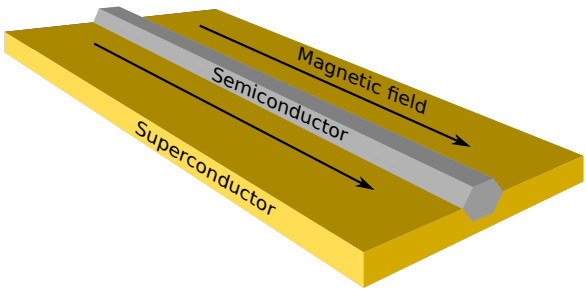

Figure 1.3: A sketch of a semiconductor nanowire on top of a superconductor and a magnetic field along the wire. The nanowire is effectively a 1-dimensional system with spin-orbit interaction.

The first experiments combining these effects used a semiconductor nanowire in proximity to a superconductor, which induces the electron-hole coupling of the superconductor into the wire. Then a magnetic field is applied along the wire to induce the Zeeman effect (Fig. 1.3). The effective Hamiltonian describing this system is

$$H = \left(\frac{p_x^2}{2m} - \mu\right)\sigma_0\tau_z + \alpha p_x \sigma_y \tau_z + g\mu_B B\sigma_z\tau_0 + \Delta\sigma_0\tau_x, \tag{1.6}$$

where p_x is the momentum, m the effective electron mass, μ the chemical potential, α the spin-orbit coupling constant, g the Landé g-factor, μ_B the Bohr magneton, and B the magnetic field. The identity/Pauli matrices are denoted by $\sigma_{0,x,y,z}$ in spin space and $\tau_{0,x,y,z}$ in particle-hole space.

All three effects combined in this proposal play an important role. Superconductivity breaks charge conservation and instead introduces particle-hole symmetry. The magnetic field breaks time-reversal symmetry, therefore breaking Kramers degeneracy. In a system with Kramers degeneracy, eigenstates at any energy only come in pairs (hence degeneracy). These pairs of eigenstates cannot be locally separated because the time-reversal operator is a local operator. Therefore, Kramers degeneracy prohibits the existence of exactly one zero energy mode at each edge of a system. Spin-orbit interaction, breaks the conservation of the spin σ_z. This is important because it creates a spectral gap around zero energy; the superconducting coupling only does that if $\mu_B B < \Delta$. Otherwise, at larger magnetic fields, the systems would not have a topological classification and could not host MBS.

This system is transversally invariant, hence the momentum is conserved, allowing to block diagonalize the Hamiltonian with one subblock for each momentum. Since the spin-orbit interaction is linear in the momentum, it acts in all blocks except for the one with $p_x = 0$. In the $p_x = 0$ block, spin is still a conserved quantity and zero energy states are possible. Since changing the topological invariant sign $\left(i\mathrm{Pf}[H(p_x)]\right)$ requires closing the spectral gap, it can only change at $p_x = 0$. When this happens the system undergoes a topological phase transition. To find these transition points consider the Hamiltonian subblock

$$H(p_x = 0) = -\mu\sigma_0\tau_z + g\mu_B B\sigma_z\tau_0 + \Delta\sigma_0\tau_x. \tag{1.7}$$

It has zero energy states, and therefore the topological phase transitions, at the critical magnetic field $B_C = \pm\sqrt{\Delta^2 + \mu^2}/\left(g\mu_B\right)$.

At these transition points, the system switches between hosting MBS and not hosting MBS. Now the question remains whether they arise at large magnetic fields $|B| > B_C$ or at small magnetic fields $|B| < B_C$. Since creating MBS requires broken time-reversal symmetry, it can not host MBS at $B = 0$ and therefore within the whole regime of $|B| < B_C$. Thus, MBS must arise at large magnetic fields $|B| > B_C$.

A different system showing signs of a successful, experimental creation of MBS uses a chain of magnetic atoms on a superconductor [31–35]. Even though the system seems quite different at first, it functions similarly to the nanowire. It also combines the required superconductivity with a Zeeman effect in order to break time-reversal symmetry. The main difference is that it has the option to avoid using spin-orbit interaction for breaking spin-conservation, instead a spatially inhomogeneous magnetic field with varying direction is used.

Even though there are already systems that show signs of successfully created MBS in experiment, the development of such setups is still an ongoing challenge. There are different technical issues to be addressed, ranging from more fundamental problems such as the nonzero density of states in the superconducting gap ('soft gap') in early experiments [25–28] to technical issues such as the constraint that a nanowire needs to be aligned parallel with the magnetic field to host MBS, which makes the creation of networks out of these systems difficult. An example for ongoing (theoretical) work is the development of systems that need lower magnetic fields for the creation of MBS either in wires [36] or in 2-dimensional electron gasses [37, 38] (2DEGs), to prevent the magnetic fields from inducing vortices into the superconductors.

1

DETECTION OF MAJORANA BOUND STATES

MESOSCOPIC SUPERCONDUCTING CIRCUITS

The key ingredient in detecting or manipulating MBS [39–41] are superconducting circuits [42–46]. In addition to elements that are well known from normal electrical circuits, such as capacitors and inductors, many superconducting circuits have a nonlinear element called a Josephson junction. A Josephson junction consists of two superconductors connected by a normal material, for example, an insulator or a normal conductor. Supercurrent still flows through the junction, if the superconductors are close enough to each other to still be coupled.

There is a fundamental difference between a Josephson junction and a dissipative conductor: Supercurrent flowing through the Josephson junction does not imply a voltage drop. Instead a constant voltage leads to a time dependent current. This follows from the Josephson relations[1]

$$U = \frac{\hbar\dot{\phi}}{2e}, \quad I = I_c \sin(\phi), \tag{1.8}$$

with U the voltage, I the current, $\hbar$ the Planck constant, e the electron charge, I_c a system dependent constant, and ϕ the phase difference of the superconducting order parameters on both sides of the junction.

Josephson junctions are similar to (dissipationless) inductors, since both are able to carry DC current indefinitely without an applied voltage. Their similarity is also formally visible since the current through both depend directly on ϕ. For an inductance L

$$U = L\dot{I}, \quad \text{therefore} \quad I = \frac{\hbar\phi}{2eL}. \tag{1.9}$$

Here we dropped an integration constant, since it is a gauge degree of freedom.

Capacitors, on the other hand, act differently: current is only caused by a change in voltage. Therefore expressing the current in terms of ϕ requires time derivatives

$$Q = CU, \quad \text{therefore} \quad I = \dot{Q} = C\frac{\hbar\ddot{\phi}}{2e}, \tag{1.10}$$

where Q is the charge and C the capacity.

There are different possibilities to derive the equations of motion for a superconducting circuit: either one uses Kirchhoff laws, or one uses a Lagrangian formalism. For the first option the current-phase relations are sufficient. A Lagrangian formulation requires expressions of the energy stored in each of the elements in terms of ϕ:

$$\begin{aligned} E &= \int UI\,dt = \int \frac{\hbar\dot{\phi}}{2e} I\,dt, \\ \text{therefore} \quad E &= \begin{cases} -(\hbar I_c/2e)\cos(\phi) & \text{for Josephson junctions,} \\ \left(\hbar^2/8e^2L\right)\phi^2 & \text{for inductors,} \\ \left(\hbar^2 C/8e^2\right)\dot{\phi}^2 & \text{for capacitors.} \end{cases} \end{aligned} \tag{1.11}$$

[1] The form of the current-phase relation depends on the details of the junction. Here we assume a superconductor-insulator-superconductor) junction.

The energy stored in a capacitor acts like kinetic energy, since it depends on $\dot{\phi}$, while inductors and Josephson junctions act like potentials.

Superconducting circuits also give a good framework to demonstrate quantum behavior. The conjugate variables are ϕ and Q:

$$[Q,\phi] = -2ie, \quad Q = -2ie\partial_\phi. \tag{1.12}$$

As a minimal example of a quantum mechanical superconducting circuit, consider a 'Cooper-pair box', which is a superconducting island coupled to ground by a Josephson junction. The island has a capacitive coupling to ground, in addition to the Josephson coupling (Fig. 1.4). The Hamiltonian is the sum of the energies stored in both elements, where we express the capacitor's energy in terms of Q with an induced charge offset q. Then the time independent Schrödinger equation

$$E|\Psi\rangle = \left[\frac{1}{2C}\left(-2ie\partial_\phi - q\right)^2 + E_J\cos(\phi)\right]|\Psi\rangle \tag{1.13}$$

yields a discrete spectrum (Fig. 1.5).

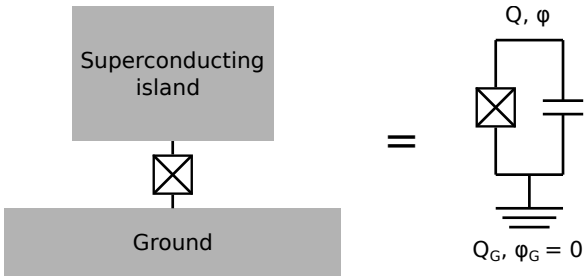

Figure 1.4: Sketch of a superconducting island coupled to a (superconducting) ground via a Josephson junction and a circuit diagram representing the same system.

The energy levels are periodic in q with the period of one Cooper-pair charge $2e$, because the system conserves charge modulo $2e$. In the case of Fig. 1.5(a) the Hamiltonian is dominated by charging energy, which is why the spectrum looks mostly parabolic. In (b) the Josephson coupling dominates the low energy states, suppressing their energy dependence on q.

Bigger circuits are more complex, but finding the Hamiltonian or classical equations of motion works in the same way as for the Cooper-pair box. Therefore we now move on to include MBS into superconducting circuits.

MAJORANA BOUND STATES IN SUPERCONDUCTING CIRCUITS

Any two Majorana operators γ_i, γ_j combined form a fermionic mode with the annihilation operator $b = \frac{1}{2}(\gamma_i + i\gamma_j)$. In the case of two combined MBS, this fermionic mode is a zero-energy eigenstate of the (interaction free) Hamiltonian, which is partly localized at both edges of the system. It affects the spectrum by causing a degeneracy of all levels, since this mode can be either filled or empty without changing the energy in the system.

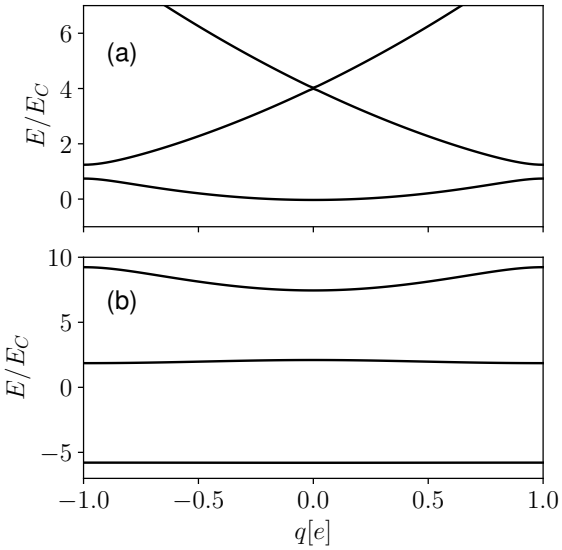

Figure 1.5: The lowest energy levels of a Cooper-pair box as a function of the offset charge q at (a) $E_J/E_C = 0.5$ and (b) $E_J/E_C = 10$, with $E_C = \frac{e^2}{2C}$.

The sought-after topological protection of this mode also makes it hard to manipulate/measure its state, because there is no local operator that distinguishes between the two ground states. A nonlocal operator that distinguishes them is the fermion parity $p = -1^n$, with n the number of fermions in the system, since the groundstates differ by the occupation number of exactly one fermionic mode. Physically that means, manipulating/measuring the fermion parity allows to manipulate/measure the state of the zero energy mode.

For an actual measurement, the fermion parity is not directly accessible, since one cannot easily count all particles in a condensed matter system. A related quantity that is measurable though is the charge of the system. That includes the charge parity $-1^{Q/e}$, which is equal to the fermion parity, because both change when adding an electron/hole.

The charge parity is an accessible physical quantity even though it is nonlocal, because the charging energy is caused by an interaction. In the example of a Cooper-pair box hosting MBS (Fig. 1.6), the charge parity acts as a charge offset in the capacitor

$$H = \frac{1}{2C}(Q - q + ep/2)^2 + E_J \cos(\phi). \tag{1.14}$$

Absorbing charge from Q into q allows to rewrite

$$H = \frac{1}{2C}(Q - q + ei\gamma_1\gamma_2/2)^2 + E_J \cos(\phi). \tag{1.15}$$

If the ground state energy of a Cooper-pair box is sensitive to the offset charge, it is also sensitive to the fermion parity (Fig. 1.7), unless $Q - q = ne$, with n an integer. The

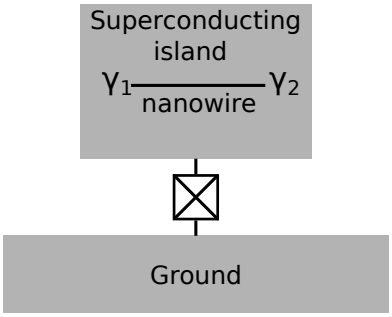

Figure 1.6: A Cooper-pair box with a wire hosting MBS on top. The MBS allow the Cooper-pair box to have either even or odd fermion parity.

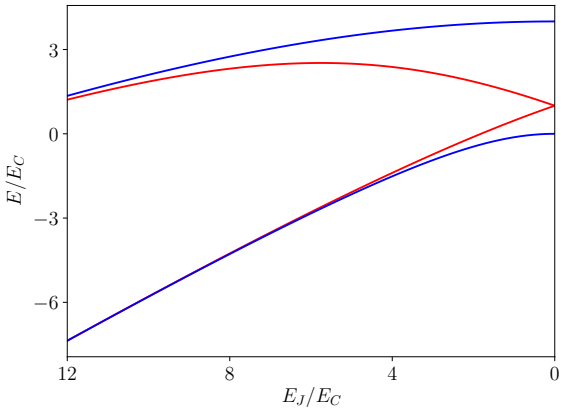

Figure 1.7: The lowest two energy levels of the Cooper pair box for $-q+ei\gamma_1\gamma_2/2 = 0$ (blue) and $-q+ei\gamma_1\gamma_2/2 = e$ (red) as a function of the Josephson energy. At large Josephson energies, the states with different parities are (almost) degenerate, but at low Josephson energies there is an energy splitting between them.

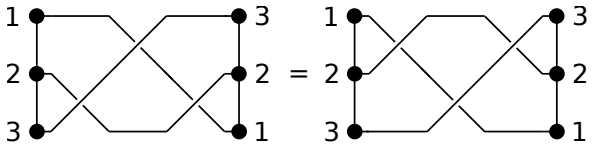

Figure 1.8: A visual representation of the braid group property in Eq. 1.22. Each operation in the braid group is sketched by two lines crossing. One distinguishes which line is on top and which one is on the bottom (denoted as an interupted line), since one is the inverse of the other. The two sketches only differ by a deformation of the lines, which does not require cutting any of them; therefore the represented operations are equal.

energy splitting between the states with different parities effectively acts as a nonlocal coupling between the MBS [47]. This allows effects like charge transport through the MBS or a spectral readout of the fermionic mode formed by the MBS, making it an important effect for the detection of MBS.

BRAIDING

MBS are not only interesting for a topologically protected zero energy mode, but also for their non-Abelian exchange statistics [8–10]. These are visible during an adiabatic exchange of two MBS where the parity $i\gamma_j\gamma_k$ is conserved.

In terms of the time evolution operator $U(t)$, switching their positions implies:

$$U(T)\gamma_j U^\dagger(T) = \alpha\gamma_k, \tag{1.16}$$

$$U(T)\gamma_k U^\dagger(T) = \beta\gamma_j, \tag{1.17}$$

where T is a point in time after switching the positions of the two MBS and α, β are variables with an absolute value of one. Since the parity $i\gamma_j\gamma_k$ is conserved during this process, $U(t)$ only contains terms with even numbers of fermionic operators; therefore

$$U(T) = \exp(i\phi)\left(\lambda + i\sqrt{1-|\lambda|^2}\gamma_j\gamma_k\right). \tag{1.18}$$

Here $\exp(i\phi)$ is an unphysical global phase factor; therefore is henceforth dropped. The constraint from eq. 1.16 defines λ, such that

$$U(T) = \frac{1}{\sqrt{2}}\left(1 \pm i\gamma_j\gamma_k\right) = \exp\left(\pm i\pi\gamma_j\gamma_k/4\right). \tag{1.19}$$

This is a $\pi/4$-gate on the ground state manifold. The sign in $U(T)$ depends on the direction of the switching process, so on the path of the MBS creating either a right- or left-handed loop.

In systems with more than two MBS, there are exchange operations that do not commute trivially:

$$\left[U_{i,j}, U_{i,k}\right] = \sqrt{2}\gamma_j\gamma_k. \tag{1.20}$$

Therefore, MBS have non-Abelian exchange statistics. Furthermore they fulfill the braid relations

$$U_{i,j}U_{k,l} = U_{k,l}U_{i,j}, \tag{1.21}$$

$$U_{i,j}U_{i,k}U_{i,j} = U_{i,k}U_{i,j}U_{i,k}, \tag{1.22}$$

with $i \neq j,k,l$ and $j \neq k,l$ and $k \neq l$. Fulfilling the braid relations makes the exchange of MBS a physical implementation of the braid group (Fig. 1.8), hence the name braiding.

The calculation leading to eq. 1.19 also works conversely: applying the operator $U_{i,j}$ always implies braiding the two corresponding MBS. This makes the quantum state resilient to noise, because exchanging two spatially separated MBS is not possible using local perturbations.

THIS THESIS

We briefly summarize each of the following chapters.

CHAPTER 2: MAJORANA BOUND STATES IN THE BULK OF A QUANTUM HALL EFFECT

A known strategy for creating MBS is to couple a quantum Hall edge state with a superconductor. We consider an alternative approach, where the Majorana bound states are created by coupling the superconductor to the gapped bulk of the quantum Hall effect. We demonstrate that this approach allows to simplify the geometry for creating MBS, and allows to use spin-orbit coupling instead of Zeeman effect to open the topological gap.

CHAPTER 3: CREATING MAJORANA BOUND STATES USING SUPERCONDUCTING PHASE DIFFERENCES

Creating Majorana bound states is possible by combining conventional superconductivity, Zeeman effect and spin-orbit interaction in one dimension. The magnetic field required for the Zeeman effect is detrimental to superconductors. We develop an alternative system hosting Majorana bound states based on a Josephson junction with spin-orbit interaction and supercurrents parallel to that junction. These supercurrents break time reversal symmetry and make magnetic fields unnecessary.

CHAPTER 4: DETECTING MAJORANA NONLOCALITY USING STRONGLY COUPLED MAJORANA BOUND STATES

Pairs of Majorana bound states (MBS) differ from the regular zero energy Andreev bound states in their nonlocal properties. We design strategies for detection of this nonlocality by using the phenomenon of Coulomb-mediated Majorana coupling in a setting which still retains falsifiability and does not require locally separated MBS. Focusing on the implementation of MBS based on the quantum spin Hall effect, we also design a way to probe Majoranas without the need to open a magnetic gap in the helical edge states. In the setup that we analyze, long range MBS coupling manifests in the h/e magnetic flux periodicity of tunneling conductance and supercurrent. While h/e is also the periodicity of Aharonov-Bohm effect and persistent current, we show how to ensure its Majorana origin by verifying that switching off the charging energy restores $h/2e$ periodicity conventional for superconducting systems.

1

CHAPTER 5: THE AC JOSEPHSON LASER

Superconducting electronic devices have reemerged as contenders for both classical and quantum computing due to their fast operation speeds, low dissipation, and long coherence times. An ultimate demonstration of coherence is lasing. We use one of the fundamental aspects of superconductivity, the ac Josephson effect, to demonstrate a laser made from a Josephson junction strongly coupled to a multimode superconducting cavity. A dc voltage bias applied across the junction provides a source of microwave photons, and the circuit's nonlinearity allows for efficient down-conversion of higher-order Josephson frequencies to the cavity's fundamental mode. The simple fabrication and operation allows for easy integration with a range of quantum devices, allowing for efficient on-chip generation of coherent microwave photons at low temperatures.

REFERENCES

[1] S. D. Huber, *Topological mechanics,* Nat Phys **12**, 621 (2016).

[2] N. Goldman, J. C. Budich, and P. Zoller, *Topological quantum matter with ultracold gases in optical lattices,* Nat Phys **12**, 639 (2016).

[3] S.-Q. Shen, *The family of topological phases in condensed matter†,* Natl Sci Rev **1**, 49 (2014).

[4] M. Z. Hasan and C. L. Kane, *Colloquium,* Rev. Mod. Phys. **82**, 3045 (2010).

[5] R. F. Service, *Search for Majorana fermions nearing success at last?* Science **332**, 193 (2011).

[6] F. Wilczek, *Majorana returns,* Nat Phys **5**, 614 (2009).

[7] C. Beenakker and L. Kouwenhoven, *A road to reality with topological superconductors,* Nat Phys **12**, 618 (2016).

[8] D. A. Ivanov, *Non-Abelian statistics of half-quantum vortices in p-wave superconductors,* Phys. Rev. Lett. **86**, 268 (2001).

[9] N. Read and D. Green, *Paired states of fermions in two dimensions with breaking of parity and time-reversal symmetries and the fractional quantum Hall effect,* Phys. Rev. B **61**, 10267 (2000).

[10] S. D. Sarma, M. Freedman, and C. Nayak, *Majorana zero modes and topological quantum computation,* npj Quantum Information **1**, npjqi20151 (2015).

[11] A. Stern, *Non-Abelian states of matter,* Nature **464**, 187 (2010).

[12] J. Fröhlich and F. Gabbiani, *Braid statistics in local quantum theory,* Rev. Math. Phys. **02**, 251 (1990).

[13] G. Moore and N. Read, *Nonabelions in the fractional quantum hall effect,* Nuclear Physics B **360**, 362 (1991).

[14] S. Trebst, M. Troyer, Z. Wang, and A. W. W. Ludwig, *A short introduction to Fibonacci anyon models,* Prog Theor Phys **176**, 384 (2008).

[15] A. Stern, *Anyons and the quantum Hall effect—A pedagogical review,* Annals of Physics **323**, 204 (2008).

[16] A. Y. Kitaev, *Fault-tolerant quantum computation by anyons,* Annals of Physics **303**, 2 (2003).

[17] M. H. Freedman, *P/NP, and the quantum field computer,* PNAS **95**, 98 (1998).

[18] C. Nayak, S. H. Simon, A. Stern, M. Freedman, and S. Das Sarma, *Non-Abelian anyons and topological quantum computation,* Rev. Mod. Phys. **80**, 1083 (2008).

[19] A. Y. Kitaev, *Unpaired Majorana fermions in quantum wires,* Phys.-Usp. **44**, 131 (2001).

[20] L. Fu and C. L. Kane, *Superconducting proximity effect and Majorana fermions at the surface of a topological insulator,* Phys. Rev. Lett. **100**, 096407 (2008).

[21] J. D. Sau, R. M. Lutchyn, S. Tewari, and S. Das Sarma, *Generic new platform for topological quantum computation using semiconductor heterostructures,* Phys. Rev. Lett. **104**, 040502 (2010).

[22] J. Alicea, *Majorana fermions in a tunable semiconductor device,* Physical Review B **81** (2010), 10.1103/PhysRevB.81.125318, arXiv: 0912.2115.

[23] R. M. Lutchyn, J. D. Sau, and S. Das Sarma, *Majorana fermions and a topological phase transition in semiconductor-superconductor heterostructures,* Phys. Rev. Lett. **105**, 077001 (2010).

[24] Y. Oreg, G. Refael, and F. von Oppen, *Helical liquids and Majorana bound states in quantum wires,* Phys. Rev. Lett. **105**, 177002 (2010).

[25] V. Mourik, K. Zuo, S. M. Frolov, S. R. Plissard, E. P. a. M. Bakkers, and L. P. Kouwenhoven, *Signatures of Majorana fermions in hybrid superconductor-semiconductor nanowire devices,* Science **336**, 1003 (2012).

[26] A. Das, Y. Ronen, Y. Most, Y. Oreg, M. Heiblum, and H. Shtrikman, *Zero-bias peaks and splitting in an Al-InAs nanowire topological superconductor as a signature of Majorana fermions,* Nat Phys **8**, 887 (2012).

[27] A. D. K. Finck, D. J. Van Harlingen, P. K. Mohseni, K. Jung, and X. Li, *Anomalous modulation of a zero-bias peak in a hybrid nanowire-superconductor device,* Phys. Rev. Lett. **110**, 126406 (2013).

[28] M. T. Deng, C. L. Yu, G. Y. Huang, M. Larsson, P. Caroff, and H. Q. Xu, *Anomalous zero-bias conductance peak in a Nb–InSb nanowire–Nb hybrid device,* Nano Lett. **12**, 6414 (2012).

[29] S. M. Albrecht, A. P. Higginbotham, M. Madsen, F. Kuemmeth, T. S. Jespersen, J. Nygård, P. Krogstrup, and C. M. Marcus, *Exponential protection of zero modes in Majorana islands,* Nature **531**, 206 (2016).

[30] H. Zhang, Ö. Gül, S. Conesa-Boj, K. Zuo, V. Mourik, F. K. de Vries, J. van Veen, D. J. van Woerkom, M. P. Nowak, M. Wimmer, D. Car, S. Plissard, E. P. A. M. Bakkers, M. Quintero-Pérez, S. Goswami, K. Watanabe, T. Taniguchi, and L. P. Kouwenhoven, *Ballistic Majorana nanowire devices,* arXiv:1603.04069 (2016), arXiv: 1603.04069.

[31] S. Nadj-Perge, I. K. Drozdov, B. A. Bernevig, and A. Yazdani, *Proposal for realizing Majorana fermions in chains of magnetic atoms on a superconductor,* Phys. Rev. B **88**, 020407 (2013).

[32] M. Kjaergaard, K. Wölms, and K. Flensberg, *Majorana fermions in superconducting nanowires without spin-orbit coupling,* Phys. Rev. B **85**, 020503 (2012).

[33] T.-P. Choy, J. M. Edge, A. R. Akhmerov, and C. W. J. Beenakker, *Majorana fermions emerging from magnetic nanoparticles on a superconductor without spin-orbit coupling,* Phys. Rev. B **84**, 195442 (2011).

[34] S. Nadj-Perge, I. K. Drozdov, J. Li, H. Chen, S. Jeon, J. Seo, A. H. MacDonald, B. A. Bernevig, and A. Yazdani, *Observation of Majorana fermions in ferromagnetic atomic chains on a superconductor,* Science **346**, 602 (2014).

[35] B. E. Feldman, M. T. Randeria, J. Li, S. Jeon, Y. Xie, Z. Wang, I. K. Drozdov, B. Andrei Bernevig, and A. Yazdani, *High-resolution studies of the Majorana atomic chain platform,* Nat Phys **13**, 286 (2017).

[36] A. Romito, J. Alicea, G. Refael, and F. von Oppen, *Manipulating Majorana fermions using supercurrents,* Phys. Rev. B **85**, 020502 (2012).

[37] F. Pientka, A. Keselman, E. Berg, A. Yacoby, A. Stern, and B. I. Halperin, *Topological superconductivity in a planar Josephson junction,* Phys. Rev. X **7**, 021032 (2017).

[38] M. Hell, M. Leijnse, and K. Flensberg, *Two-Dimensional platform for networks of Majorana bound states,* Phys. Rev. Lett. **118**, 107701 (2017).

[39] T. Hyart, B. van Heck, I. C. Fulga, M. Burrello, A. R. Akhmerov, and C. W. J. Beenakker, *Flux-controlled quantum computation with Majorana fermions,* Phys. Rev. B **88**, 035121 (2013).

[40] D. Aasen, M. Hell, R. V. Mishmash, A. Higginbotham, J. Danon, M. Leijnse, T. S. Jespersen, J. A. Folk, C. M. Marcus, K. Flensberg, and J. Alicea, *Milestones toward Majorana-based quantum computing,* Phys. Rev. X **6**, 031016 (2016).

[41] J. Manousakis, A. Altland, D. Bagrets, R. Egger, and Y. Ando, *Majorana qubits in a topological insulator nanoribbon architecture,* Phys. Rev. B **95**, 165424 (2017).

[42] G. Wendin, *Quantum information processing with superconducting circuits: a review,* arXiv:1610.02208 [quant-ph] (2016), arXiv: 1610.02208.

[43] M. H. Devoret and R. J. Schoelkopf, *Superconducting circuits for quantum information: An outlook,* Science **339**, 1169 (2013).

[44] R. J. Schoelkopf and S. M. Girvin, *Wiring up quantum systems,* Nature **451**, 664 (2008).

[45] J. Clarke and F. K. Wilhelm, *Superconducting quantum bits,* Nature **453**, 1031 (2008).

[46] J. Q. You and F. Nori, *Superconducting circuits and quantum information,* Physics Today **58**, 42 (2005).

[47] L. Fu, *Electron teleportation via Majorana bound states in a mesoscopic superconductor,* Phys. Rev. Lett. **104**, 056402 (2010).

2

MAJORANA BOUND STATES IN THE BULK OF A QUANTUM HALL EFFECT

INTRODUCTION

Superconductivity, owing its robust nature to the time-reversal symmetry [1], is in a direct competition with the quantum Hall effect (QHE), requiring a strong breaking of that symmetry. Consequently, coupling a superconductor with QHE edge states modifies the physics of proximity superconductivity and results in unusual phenomena. Because Andreev reflection within a QHE edge state couples an electron to a hole propagating in the same direction, it becomes maximally nonlocal [2–4] and leads to supercurrents carried by trajectories enclosing the complete sample area [5, 6]. While theoretical analysis of such systems extends to the fractional QHE regime [7–11], the experimental progress despite showing promise now mostly focuses on the integer QHE states [12–14] well-approximated by single particle physics.

Because these systems combine strong breaking of time reversal symmetry with superconductivity, they serve as a natural platform for creating Majorana bound states [15–19] (MBS), the simplest non-Abelian anyons. Beyond single-particle physics, the fractional QHE combined with superconductivity was studied theoretically as a potential host system for more exotic types of non-Abelian anyons [20–26]. The approach common to most of these to inducing superconductivity in these systems is to couple the couter-propagating edge states by a superconductor, and to either rely on the crossed Andreev reflection between two edges, or to engineer an edge containing decoupled counter-propagating modes. A new strategy of creating a topological phase explored in the recent works [26, 27] relies on coupling the superconductor with the bulk gapped phase of the QHE instead of interfacing the edge states.

Here we present a study of MBS in the bulk of a 2D quantum well with a Rashba spin-orbit coupling. While our overall conclusions agree with those of the recent related work Ref. [27], we provide an analytical construction of the topological band structure. We also extend the previous analysis to the higher Landau levels, and we show that depending

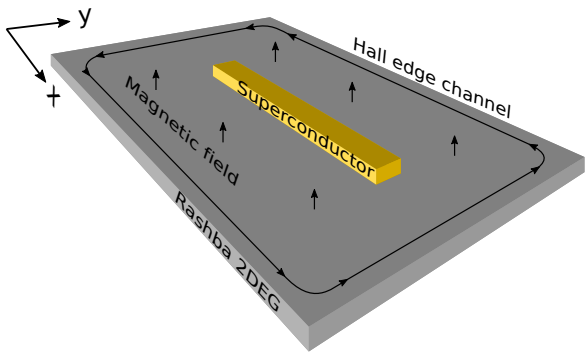

Figure 2.1: A 2DEG with spin-orbit interaction and a superconducting wire on top. The magnetic field through the 2DEG causes a quantum Hall effect, making the bulk insulating but giving rise to edge channels.

on the microscopic details, the Zeeman field and spin-orbit can be either competing or complementing each other in opening the topological gap.

SETUP

We consider a 2D electron gas (2DEG) with Rashba spin-orbit interaction and a magnetic field inducing a QHE. A superconducting wire deposited on top of the 2DEG (Fig. 2.1) provides the electron-hole coupling in the 2DEG via the superconducting proximity effect. As long as the wire is sufficiently separated from the sample edges, all the quasiparticle states influenced by the wire are localized in its proximity by magnetic field. We consider the typical situation when the induced superconducting gap Δ is comparable or smaller than the Landau level (LL) separation $\hbar\omega_c = eB/m_e$, with $\hbar$ the Planck constant, ω_c the cyclotron frequency, e the electron charge, B magnetic field, and m_e the effective electron mass in the semiconductor. Additionally, in order to avoid the creation of vortices inside the superconducting wire, we focus on the case when its width w_{sc} is comparable to the magnetic length $l_B = \sqrt{\hbar/eB}$. In this regime the superconductor acts as a localized perturbation of the Landau level Hamiltonian, instead of separating the two sides of the wire by a region with a superconducting gap.

Because the superconductor has to withstand quantizing magnetic fields, our choice is limited to several type-II superconductors, such as NbN, that have sufficient upper critical fields ($B_{c2} \approx 25\,\mathrm{T}$). Reducing the width w_{sc} of the superconducting wire further reduces its sensitivity to the magnetic field, increasing its lower critical field B_{c1} [28]. On the other hand, when the superconducting wire is thinner than the extent of the QHE edge states $w_{\mathrm{sc}} \ll l_B$, the proximity gap becomes suppressed because the quasiparticles spend a large fraction of time outside of the reason covered by a superconductor. We therefore focus on the regime when $w_{\mathrm{sc}} \sim l_B$ and consider the superconducting gap Δ constant.

MODEL

The effective Hamiltonian for the 2DEG is

$$H = \left(\frac{p_x^2 + p_y^2}{2m_e} - \mu\right)\sigma_0\tau_z + \frac{g\mu_B B}{2}\sigma_z\tau_0 + \alpha(p_x\sigma_y - p_y\sigma_x)\tau_z + \Delta(x,y)\sigma_0\tau_x, \tag{2.1}$$

with $(p_x, p_y) \equiv \boldsymbol{p} = -i\hbar\boldsymbol{\nabla} + e\boldsymbol{A}(x,y)$, $\boldsymbol{A}(x,y)$ the vector potential, g the Landé g-factor, μ_B the Bohr magneton, μ the chemical potential, α the coupling constant of the Rashba spin-orbit interaction and $\Delta(x,y)$ the induced electron-hole coupling. The Pauli matrices in spin space are $\sigma_{x,y,z}$ and in particle-hole space $\tau_{x,y,z}$, while σ_0 and τ_0 are the identity matrices.

We disregard the position dependence of the induced gap, and choose a gauge where the superconducting gap is real: $\Delta(x,y) = \Delta_0\Theta(w_{\text{sc}}/2 - |y|)$, with Θ the Heaviside function, and Δ_0 is the induced electron-hole coupling under the superconductor. We assume that the magnetic field penetration length is much larger than w_{sc}, and therefore the magnetic field is approximately homogeneous. We futher choose the Landau gauge due to its translational invariance, and require that there is no net supercurrent flowing through the superconducting wire. These conditions together constrain $\boldsymbol{A} = By\hat{x} + \boldsymbol{c}$, with $\hat{x}$ the unit vector in x-direction, and $\boldsymbol{c}$ a constant vector. Because the supercurrent density $I_{\text{sc}} \propto \boldsymbol{A}$, the net supercurrent vanishes when $\boldsymbol{c} = 0$. Due to the translational invariance, the k_x component of momentum is conserved. In addition in this gauge, the inversion symmetry of Eq. (2.1) assumes the form $[H, I] = 0$, with the inversion symmetry operator $I = \delta(x + x')\delta(y + y')\sigma_z$.

TOPOLOGICAL PHASE TRANSITIONS

In order to understand the topological phase transitions of the 2DEG under the superconducting wire, we first diagonalize the Hamiltonian disregarding the electron-hole coupling, and then use the resulting LLs as a basis for further calculations.

The electron Hamiltonian H_e simplifies when expressed in terms of ladder operators $a, a^\dagger$ [29]:

$$H_e = \hbar\omega_c\left(a^\dagger a + \frac{1}{2}\right) + \frac{g\mu_B B}{2}\sigma_z + \frac{\sqrt{2}\alpha}{l_B}\begin{pmatrix} 0 & ia \\ -ia^\dagger & 0 \end{pmatrix}. \tag{2.2}$$

Diagonalizing this Hamiltonian we obtain the following basis of eigenenergies and corresponding eigenstates:

$$E_{n,\pm} = \hbar\omega_c\left(n + \frac{1}{2} \pm \frac{1}{2}\right) \mp \frac{1}{2}\sqrt{\left(\hbar\omega_c - g\mu_B B\right)^2 + \frac{8\alpha^2}{l_B^2}\left(n + \frac{1}{2} \pm \frac{1}{2}\right)} \tag{2.3a}$$

$$\Psi_{e,n,+}(y, k_x) = \begin{pmatrix} a_n h_n(y/l_B + k_x l_B) \\ b_n h_{n-1}(y/l_B + k_x l_B) \end{pmatrix}, \tag{2.3b}$$

$$\Psi_{e,n,-}(y, k_x) = \begin{pmatrix} b_{n+1} h_{n+1}(y/l_B + k_x l_B) \\ -a_{n+1} h_n(y/l_B + k_x l_B) \end{pmatrix}, \tag{2.3c}$$

with

$$a_n = \sqrt{\frac{1+c_n}{2l_B}}, \quad b_n = i\sqrt{\frac{1-c_n}{2l_B}}, \quad c_n = \frac{\hbar\omega_c - g\mu_B B}{\sqrt{\left(\hbar\omega_c - g\mu_B B\right)^2 + 8n\alpha^2/l_B^2}}, \tag{2.3d}$$

and h_n the normalized n-th Hermite function. To obtain the hole states we apply the particle-hole symmetry operator $P = \sigma_y\tau_y K$, with K complex conjugation, to the electron states:

$$\Psi_{h,n,\pm}(y,k_x) = P\Psi_{e,n,\pm}(y,-k_x), \tag{2.4}$$

thereby generating a full basis of particle and hole states. We observe a dependence of the spectrum on the relative sign of g and the chirality of the spin-orbit interaction.

Since we consider the regime where the coupling between different LLs caused by the superconductor is small, we project the Hamiltonian onto the LL closest to the Fermi energy. That results in an electron-hole coupling that has the form

$$H_{\mathrm{LL}}(k_x) = \begin{pmatrix} E_{n,+}-\mu & 0 & -\tilde{\Delta}_{e,n}(k_x) & -\tilde{\Delta}_{o,n}(k_x) \\ 0 & E_{n,-}-\mu & -\tilde{\Delta}_{o,n+1}(k_x) & \tilde{\Delta}_{e,n}(k_x) \\ -\tilde{\Delta}_{e,n}(k_x) & \tilde{\Delta}_{o,n+1}(k_x) & -E_{n,-}+\mu & 0 \\ \tilde{\Delta}_{o,n}(k_x) & \tilde{\Delta}_{e,n}(k_x) & 0 & -E_{n,+}+\mu \end{pmatrix}, \tag{2.5a}$$

$$\tilde{\Delta}_{e,n} = \Delta_0 \int dy\Theta(w_{sc}/2-|y|)\left(a_n a_{n+1}h_n^+h_n^- - b_n b_{n+1}h_{n-1}^+h_{n+1}^-\right), \tag{2.5b}$$

$$\tilde{\Delta}_{o,n} = \Delta_0 \int dy\Theta(w_{sc}/2-|y|)2a_n b_n h_n^+h_{n-1}^-, \tag{2.5c}$$

with the shorthand notation $h_n^\pm \equiv h_n(y/l_B \pm k_x l_B)$. This shows two qualitatively different kinds of couplings that the superconductor induces into the 2DEG. The first one, $\tilde{\Delta}_{e,n}$ is an even function in k_x and conserves the chirality of the state. The second coupling, $\tilde{\Delta}_{o,n}$ is odd in k_x and couples particles to their inversion-symmetric antiparticle. Since the Hamiltonian is inversion- and particle-hole symmetric, this coupling acts between states at opposite energies; in other words it couples states at energy E to states at $-E$.

Combining these two couplings causes topological phase transitions. The key is that the coupling $\tilde{\Delta}_{e,n}$ does not open a spectral gap around zero energy, since it does not couple states of opposite energies. If the superconducting coupling is sufficiently strong, it even closes this gap, since it creates a bump in the originally flat bands of the QHE (Fig. 2.3). This is where the second coupling $\tilde{\Delta}_{o,n}$ shows its effect. Since it does couple states at opposite energies, it reopens the gap. However, because it is odd in k_x it does not create a gap at $k_x = 0$, therefore allowing topological phase transitions, when the first coupling causes zero energy states at $k_x = 0$.

To find an analytic expression for the topological invariant consider the spectrum of $H_{\mathrm{LL}}(0)$:

$$E = \pm\left[\frac{E_{n,+}-E_{n,-}}{2} \pm \sqrt{\frac{(E_{n,+}+E_{n,-}-2\mu)^2}{4} + \tilde{\Delta}_{e,n}^2(0)}\right]. \tag{2.6}$$

Zero energy states indicating topological phase transitions arise at $-(E_{n,+}-\mu)(E_{n,-}-\mu) = \tilde{\Delta}_{e,n}^2(0)$. In addition to the phase transition at $k_x = 0$, another phase transition happens

at $(E_{n,+}-\mu)(E_{n,-}-\mu)=0$ when the unperturbed LL crosses zero energy. Combined that yields the topological invariant

$$\mathcal{Q}=\begin{cases}-1 & 0<-(E_{n,+}-\mu)(E_{n,-}-\mu)<\tilde{\Delta}_{e,n}^2(0),\\ 1 & \text{otherwise.}\end{cases} \tag{2.7}$$

Therefore, creating MBS requires the chemical potential to be tuned inside the gap of the spin-split LL.

BAND STRUCTURES AND TOPOLOGICAL INVARIANTS

SIMULATED SYSTEM

The setup presented here uses the bulk and does not require quantum Hall edge states coupling to the wire. We use KWANT [30] to simulate the system using a tight binding approximation. To prevent the quantum Hall edge states from entering the calculation we create a system without them. Therefore we roll the system up into a cylinder (Fig. 2.2) to impose periodic boundary conditions, and remove the quantum Hall edge states by setting the flux penetrating each unit cell to an integer number of flux quanta ($h/2e$).

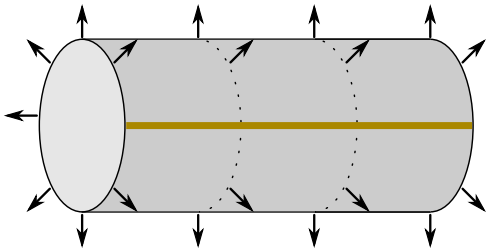

Figure 2.2: The same system as in Fig. 2.1, but width periodic boundary conditions in y-direction and infinitely long. The periodic boundary conditions remove the quantum Hall edge states, therefore preventing them from coupling to the superconducting wire.

In order to evaluate the topological invariant $\mathcal{Q}$ we attach a normal lead to the proximitized region, and evaluate the reflection block r of the scattering matrix in the basis where the electron and hole modes are related to each other by the particle-hole symmetry operator. We then evaluate the topological invariant $\mathcal{Q}=\operatorname{sign}\det r$ following the scattering formalism [31].

Unless otherwise specified we use the following parameters in all simulations. We assume an InAs/GaSb 2DEG [32] resulting in the effective electron mass $m_e=0.04m$, with m the free electron mass, $g=-11.5$ and $\alpha=8\,\text{meV nm}$. In addition, we choose $\Delta_0=1\,\text{meV}$, $w_{\text{sc}}=50\,\text{nm}$ and $B=1\,\text{T}$.

MBS IN THE LOWEST LANDAU LEVEL

After discussing the possibility of topological phase transitions, we now take a more detailed look at band structures. Our starting point is the lowest Landau level.

The first band structure shows how the coupling conserving the spin, $\tilde{\Delta}_{e,n}$ acts on a normal QHE. In Fig. 2.3a, there is a Gaussian bump in the band structure. At this point we

set $g = 0$ and $\alpha = 0$ preventing any coupling to spins; therefore the level repulsion is still around zero energy.

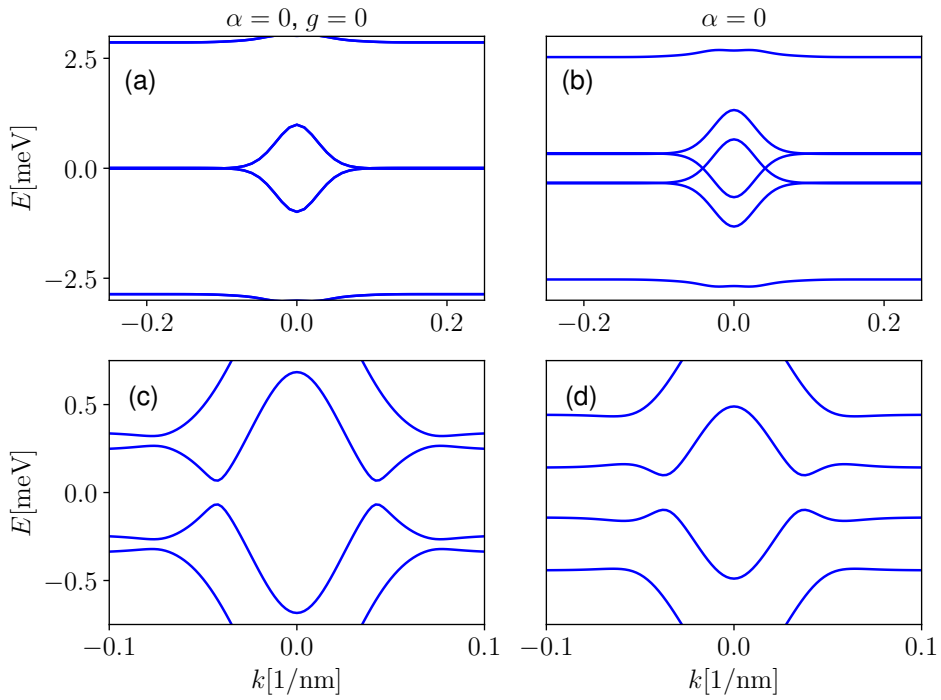

Figure 2.3: (a) A band structure, with the chemical potential such that the lowest Landau Level is at zero energy and $g = 0$, $\alpha = 0$. The superconducting wire causes the level repulsion between the electron and the hole band around $k = 0$. (b) The same as in (a) plus Zeeman effect. In this example the superconductor makes the QHE a gapless system. (c) The same as in (b) with Rashba spin-orbit interaction. The gap reopens and the system is topologically nontrivial, therefore a finite wire hosts MBS at the edges. (d) The same as in (c) with changed chemical potential, in order to increase the gap around zero energy.

Then we add the Zeeman effect into the simulation ($g \neq 0$ in Fig. 2.3 b). This illustrates how the coupling conserving the spin, $\tilde{\Delta}_{e,n}$, does not open a gap around zero energy, but closes it.

In order to reopen the spectral gap, we reintroduce spin-orbit interaction (Fig. 2.3 c), therefore making the coupling $\tilde{\Delta}_{o,n}$ nonzero. Because of Eq. 2.7, we expect a topologically nontrivial system and the numerical calculation of the topological invariant confirms that. Changing the chemical potential allows us to increase the spectral gap (Fig. 2.3 d).

So far we have demonstrated MBS in a system with a Zeeman effect and negative g. In Fig. 2.4 we show a band structure with positive g. As expected, changing the sign of g without changing the chirality of the spin-orbit effect has an effect on the bandstructure. Since the combination of spin-orbit interaction with a magnetic field also causes a spin-splitting, it is also possible to create a topologically nontrivial system with $g = 0$, also Fig. 2.4. Therefore this setup is realizable using 2DEGs that have an arbitrarily low g-factor.

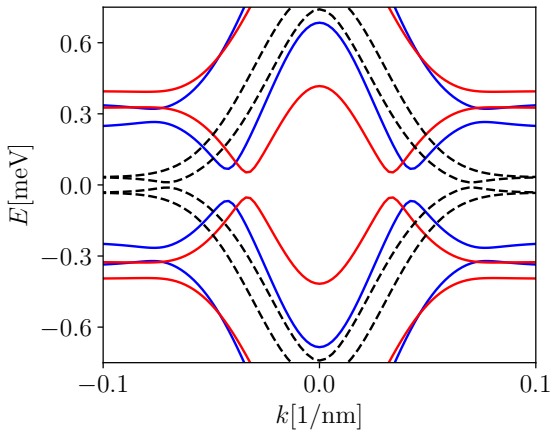

Figure 2.4: Three band structures with negative g (blue), positive g and $g = 0$ (dashed black). All three band-structures are topologically nontrivial.

MBS IN HIGHER LANDAU LEVELS

Going beyond the lowest LL increases the effect of the spin-orbit interaction. We investigate whether this increases the spectral gap of the topologically nontrivial system.

Using higher LLs has one main problem: in higher LLs with $\alpha = 0$, the band structure has more crossings at zero energy (Fig. 2.5 a, b, c). More precisely, they have $2n + 1$ crossings (again, plus their symmetric partners), with n the number of the Landau level. Optimizing parameters to maximize the level repulsion in one avoided crossing does not necessarily optimize the level repulsion in the other crossings.

Another less problematic effect is a weaker coupling to the superconductor, caused by the wider spread of the wave functions in higher LLs. For visibility, the superconducting gap is increased to $\Delta_0 = 2$meV in Fig. 2.5.

In principle it is possible to create MBS using higher LLs (Fig. 2.5 d, e, f), but creating a large spectral gap is more complex than in the lowest LL. Therefore we do not see an advantage to using higher LLs.

DISORDER AND LEADS

We conclude the numerical analysis by investigating the resilience of the proposed setup against disorder and the possibility to use the quantum Hall edge states as leads coupling to the MBS.

In order to simulate disorder we modify the system that we simulated before. We still make a cylindrical system, but this time a finite one to which we add disorder in the form of a random potential. Then we attach leads from both sides, which are also penetrated by the magnetic field. Since a cylinder would then not have propagating modes, we leave a cut in the lead, giving rise to (propagating) edge states (Fig. 2.6).

We compare the topological invariant to the Hall conductance of the underlying QHE; therefore we additionally simulate this system with a cut in the cylinder and without

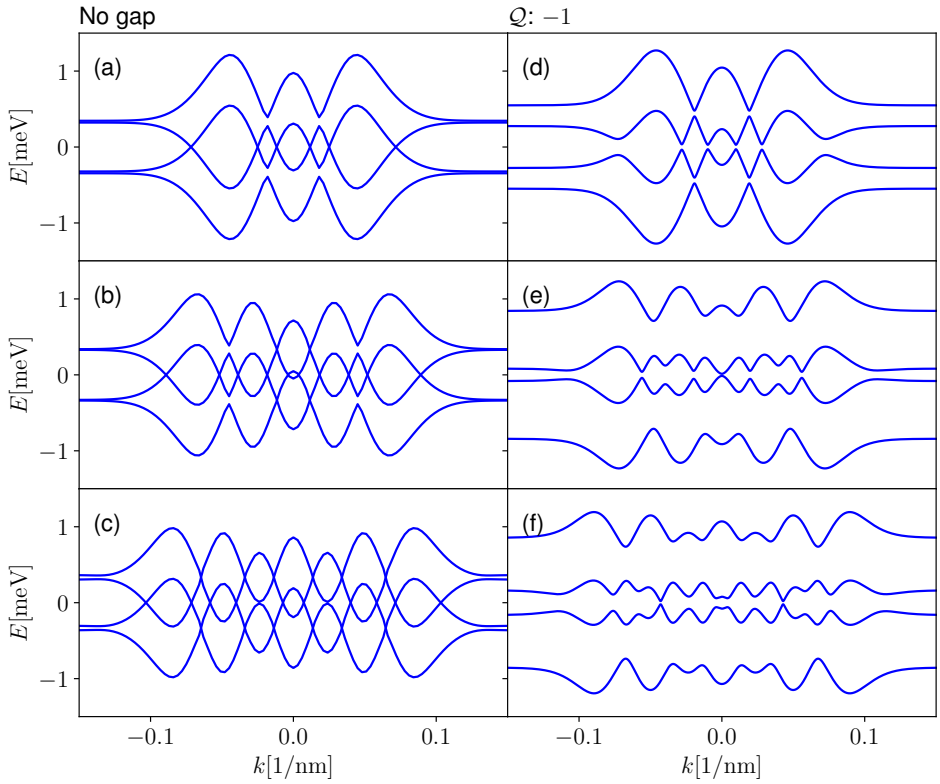

Figure 2.5: Left panel: The same as Fig. 2.3(b), but with the (a) second, (b) third, (c) fourth LL tuned near zero energy by changing μ. Right panel: topologically nontrivial band structure using the (d) second, (e) third, (f) fourth LL. Some anti-crossings have a very small gap and are hardly visible on this scale, but the calculation of the topological invariant shows that all band structures in the right panel do have a spectral gap around zero energy.

superconductivity.

We sweep the disorder strength (in terms of the mean free path λ) and the chemical potential, and for each of these parameter sets calculate I, the determinant of the scattering matrix' reflection block for one lead. If all quasiparticles are reflected by the scattering region, then $|I| = 1$. Since the disordered system has two leads with propagating modes attached to this scattering region, tunneling between the leads is possible, therefore allowing $|I| \neq 1$. For a long scattering region with a spectral gap, $|I|$ must still approach one though. Therefore we consider the sign of I as an indicator of the existence of MBS and its absolute value an indicator of the quasiparticle decay length compared to the system size. The absolute value of I is then also an indicator of the quality of the setup, since a large gap results in a short decay length. We compare I to the Hall conductance of the 2DEG (Fig. 2.7), where we use the lowest LL to create MBS.

MBS arise in the region where the Hall conductance is one. Increasing disorder destroys the effect. At disorder strength where the Hall conductance G is well quantized,

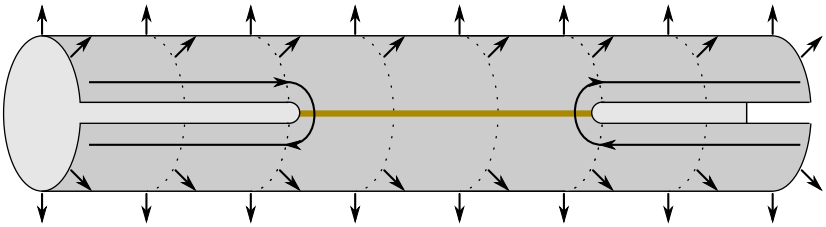

Figure 2.6: A system similar to Fig. 2.2, but with two leads and disorder in the scattering region. The leads are clean 2DEGs with the same magnetic field as in the scattering region. They are not full cylinders but are cut, therefore quantum Hall edge states arise.

it is possible to tune the chemical potential such that I is close to -1, which means that the system hosts MBS and their decay length is small compared to the system size (5μm). In the region where G is not well quantized, the QHE is broken and MBS do not arise.

We do the same comparison using the second LL (Fig. 2.8). Then the system's resilience to disorder is smaller. Even in the region where the Hall conductance is well quantized to $3e^2/h$ it is not always hosting MBS [1]. Therefore we again suggest to use the lowest Landau level.

DISCUSSION AND OUTLOOK

In summary, we have shown both analytically and numerically how a narrow superconducting wire placed on top of a 2DEG can support MBS in quantizing magnetic fields in presence of Rashba spin-orbit coupling. We showed that unlike in semiconductor nanowires, the cyclotron motion of electrons makes the spin-orbit coupling contribute to the splitting between the different spin bands and allows to create MBS without relying on the Zeeman effect. Our analytical and numerical checks show that odd integer quantization of the Hall conductance is a necessary condition to create a topologically nontrivial phase when the superconducting wire is sufficiently small, and that the topological phase is desctroyed by disorder together with the odd integer quantization of the Hall conductance.

Because this system relies on using the magnetic field as a tool for both confining electron trajectories and a source of time-reversal symmetry breaking, we avoid the need to use an additional gate pattern to control the geometry of the setup. Unlike the nanowire-based proposals [33, 34], this setup does not rely on the alignment of magnetic field parallel to the 1D system supporting MBS. It is therefore more easily extended to more complex structures like T-junctions that are required for braiding. Because the path of the quantum Hall edge states can be controlled using a gated constriction, our setup also allows to embed Majorana devices inside interferometers or other transport setups.

[1] This improves when using a larger gap Δ_0, but even with a larger Δ_0 the second LL still yields a smaller resilience to disorder.

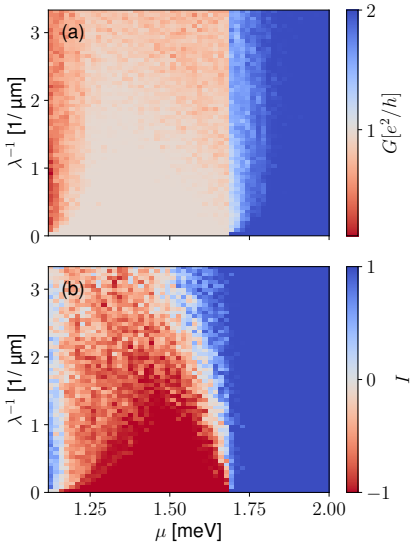

Figure 2.7: (a) Hall conductance as a function of the chemical potential and disorder strength. This is an average over ten disorder realizations in each point. (b) The determinant of the scattering matrix' reflection block I as a function of chemical potential and disorder strength, with the same disorder realizations as in (a).

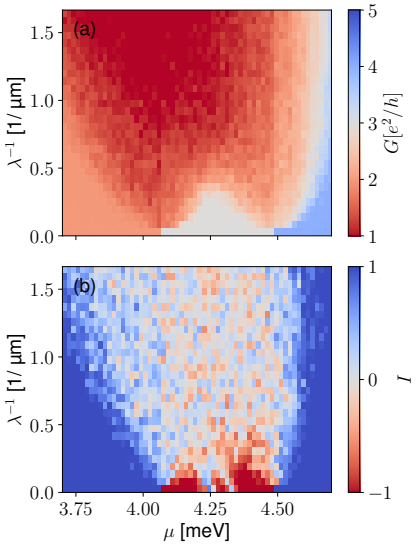

Figure 2.8: Like Fig. 2.7, but using the second Landau level.

REFERENCES

[1] P. W. Anderson, *Theory of dirty superconductors,* Journal of Physics and Chemistry of Solids **11**, 26 (1959).

[2] H. Hoppe, U. Zülicke, and G. Schön, *Andreev reflection in strong magnetic fields,* Phys. Rev. Lett. **84**, 1804 (2000).

[3] F. Giazotto, M. Governale, U. Zülicke, and F. Beltram, *Andreev reflection and cyclotron motion at superconductor normal-metal interfaces,* Phys. Rev. B **72**, 054518 (2005).

[4] A. R. Akhmerov and C. W. J. Beenakker, *Detection of Valley Polarization in Graphene by a Superconducting Contact,* Phys. Rev. Lett. **98**, 157003 (2007).

[5] A. Y. Zyuzin, *Superconductor normal-metal superconductor junction in a strong magnetic field,* Phys. Rev. B **50**, 323 (1994).

[6] J. A. M. van Ostaay, A. R. Akhmerov, and C. W. J. Beenakker, *Spin-triplet supercurrent carried by quantum Hall edge states through a Josephson junction,* Phys. Rev. B **83**, 195441 (2011).

[7] M. P. A. Fisher, *Cooper-pair tunneling into a quantum Hall fluid,* Phys. Rev. B **49**, 14550 (1994).

[8] J. E. Moore and X.-G. Wen, *Critical points in edge tunneling between generic fractional quantum Hall states,* Phys. Rev. B **66**, 115305 (2002).

[9] E.-A. Kim, S. Vishveshwara, and E. Fradkin, *Cooper-pair tunneling in junctions of singlet quantum Hall states and superconductors,* Phys. Rev. Lett. **93**, 266803 (2004).

[10] Z.-W. Zuo, L. Sheng, and D. Y. Xing, *Crossed Andreev reflections in superconductor and fractional quantum Hall liquids hybrid system,* Solid State Communications **184**, 17 (2014).

[11] Z. Wan, A. Kazakov, M. J. Manfra, L. N. Pfeiffer, K. W. West, and L. P. Rokhinson, *Induced superconductivity in high-mobility two-dimensional electron gas in gallium arsenide heterostructures,* Nature Communications **6**, ncomms8426 (2015).

[12] P. Rickhaus, M. Weiss, L. Marot, and C. Schönenberger, *Quantum Hall effect in graphene with superconducting electrodes,* Nano Lett. **12**, 1942 (2012).

[13] F. Amet, C. T. Ke, I. V. Borzenets, J. Wang, K. Watanabe, T. Taniguchi, R. S. Deacon, M. Yamamoto, Y. Bomze, S. Tarucha, and G. Finkelstein, *Supercurrent in the quantum Hall regime,* Science **352**, 966 (2016).

[14] G.-H. Lee, K.-F. Huang, D. K. Efetov, D. S. Wei, S. Hart, T. Taniguchi, K. Watanabe, A. Yacoby, and P. Kim, *Inducing superconducting correlation in quantum Hall edge states,* Nat Phys **13**, 693 (2017).

[15] A. Y. Kitaev, *Unpaired Majorana fermions in quantum wires,* Phys.-Usp. **44**, 131 (2001).

[16] F. Wilczek, *Majorana returns,* Nat Phys **5**, 614 (2009).

[17] R. F. Service, *Search for Majorana fermions nearing success at last?* Science **332**, 193 (2011).

[18] N. Read and D. Green, *Paired states of fermions in two dimensions with breaking of parity and time-reversal symmetries and the fractional quantum Hall effect,* Phys. Rev. B **61**, 10267 (2000).

[19] C. Beenakker and L. Kouwenhoven, *A road to reality with topological superconductors,* Nat Phys **12**, 618 (2016).

[20] A. Stern, *Anyons and the quantum Hall effect—A pedagogical review,* Annals of Physics **323**, 204 (2008).

[21] A. Stern, *Non-Abelian states of matter,* Nature **464**, 187 (2010).

[22] D. J. Clarke, J. Alicea, and K. Shtengel, *Exotic non-Abelian anyons from conventional fractional quantum Hall states,* Nature Communications **4**, ncomms2340 (2013).

[23] A. Vaezi, *Fractional topological superconductor with fractionalized Majorana fermions,* Phys. Rev. B **87**, 035132 (2013).

[24] A. Vaezi, *Superconducting analogue of the parafermion fractional quantum Hall states,* Phys. Rev. X **4**, 031009 (2014).

[25] J. Alicea and P. Fendley, *Topological phases with parafermions: Theory and blueprints,* Annual Review of Condensed Matter Physics **7**, 119 (2016), arXiv:1504.02476 .

[26] C. Repellin, A. M. Cook, T. Neupert, and N. Regnault, *Numerical investigation of gapped edge states in fractional quantum Hall-superconductor heterostructures,* arXiv:1707.08579 [cond-mat] (2017), arXiv:1707.08579 .

[27] F. Finocchiaro, F. Guinea, and P. San-Jose, *Topological π-junctions from crossed Andreev reflection in the quantum Hall regime,* arXiv:1708.08078 [cond-mat] (2017), arXiv:1708.08078 .

[28] G. Stan, S. B. Field, and J. M. Martinis, *Critical field for complete vortex expulsion from narrow superconducting strips,* Physical Review Letters **92**, 097003 (2004).

[29] R. Winkler, *Spin-Orbit Coupling Effects in Two-Dimensional Electron and Hole Systems* (Springer, Berlin; New York, 2003) 928796151.

[30] C. W. Groth, M. Wimmer, A. R. Akhmerov, and X. Waintal, *Kwant: A software package for quantum transport,* New J. Phys. **16**, 063065 (2014).

[31] I. C. Fulga, F. Hassler, and A. R. Akhmerov, *Scattering theory of topological insulators and superconductors,* Phys. Rev. B **85**, 165409 (2012).

[32] A. J. A. Beukman, F. K. de Vries, J. van Veen, R. Skolasinski, M. Wimmer, F. Qu, D. T. de Vries, B.-M. Nguyen, W. Yi, A. A. Kiselev, M. Sokolich, M. J. Manfra, F. Nichele, C. M. Marcus, and L. P. Kouwenhoven, *Spin-orbit interaction in a dual gated InAs/GaSb quantum well,* arXiv:1704.03482 [cond-mat] (2017), arXiv:1704.03482 .

[33] R. M. Lutchyn, J. D. Sau, and S. Das Sarma, *Majorana fermions and a topological phase transition in semiconductor-superconductor heterostructures,* Phys. Rev. Lett. **105**, 077001 (2010).

[34] Y. Oreg, G. Refael, and F. von Oppen, *Helical liquids and Majorana bound states in quantum wires,* Phys. Rev. Lett. **105**, 177002 (2010).

3

CREATING MAJORANA BOUND STATES USING SUPERCONDUCTING PHASE DIFFERENCES

INTRODUCTION

Creating Majorana bound states (MBS) [1–4], the topologically protected zero energy states, remains a major challenge. While it is possible to create MBS in spin liquids [5] or in fractional quantum Hall systems [6, 7], the most actively explored strategy relies on induced superconductivity. Specifically, breaking time-reversal symmetry (and therefore Kramers degeneracy) in a semiconductor that has superconducting correlations induced by a conventional superconductor drives the system through a topological phase transition and creates isolated MBS [8–10].

One way of breaking time-reversal symmetry is an exchange interaction with a ferromagnet [11, 12]. However, that admits no tunability, and therefore leads to the need to optimize the constituent materials and may lead to low energy states that are hard to distinguish from MBS [13]. Another commonly used approach relies on the Zeeman effect created by an external magnetic field to break the time reversal symmetry in a semiconducting nanowire [14–21]. In these systems MBS require strong magnetic fields, since the resulting electron spin splitting must exceed the induced superconducting gap. The disadvantage of this approach is the suppression of superconducting gap by the magnetic field, and the potential creation of Abrikosov vortices, both detrimental to MBS properties.

Supercurrents, and the superconducting phase differences generating them, likewise break time-reversal symmetry. Because of this property they were proposed as an auxiliary tool for lowering the minimal magnetic field required for creating MBS in different geometries [22–24]. In our work we improve these previous results and eliminate the requirement for the magnetic field altogether. The only magnetic field is then created by supercurrents, and is negligible in a mesoscopic superconductor. In order to achieve this,

we utilize the idea of Ref. [25], that showed that more than two distinct values of superconducting phase are necessary to create a topological phase transition. A known recipe for MBS creation that only uses the superconducting phase as a source of time-reversal symmetry breaking is a topological insulator-superconductor heterojunction [26, 27]. We show that the creation of MBS using phase differences is possible without using an uncommon band structure or a 3D geometry, but in a conventional 2D electron gas (2DEG).

3

SETUP

We consider a 2DEG with spin-orbit interaction covered by two superconductors with a junction in between. The superconductors carry supercurrents in opposite directions along the junction (Fig. 3.1), creating a vortex-like current pattern which couples electrons and holes with different orbital angular momenta. Because of this coupling, we expect all eigenstates of the Hamiltonian to have a nonzero orbital angular momentum. Since spin-orbit interaction couples spin to the orbital angular momentum, a nonzero angular momentum leads to an effective Zeeman field lifting spin degeneracy of all Hamiltonian eigenstates. The junction therefore becomes similar to Majorana nanowires [14, 15], because it combines a quasi-one-dimensional semiconductor with spin-orbit interaction, effective Zeeman interaction, and induced superconductivity.

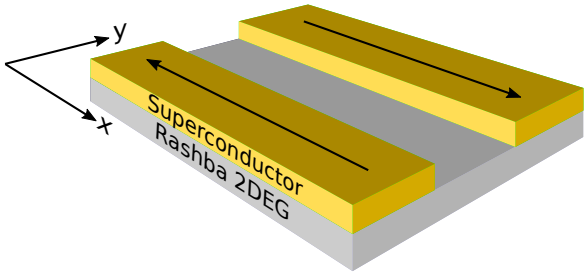

Figure 3.1: A 2DEG covered by superconductors leaving a junction. The superconductors on both sides of the junction carry currents in opposite directions, indicated by arrows. We assume the critical current of the junction to be negligible compared to the current carried by the superconducting electrodes. Otherwise the current could flow through the junction instead of the electrodes.

We model this system using a 2-dimensional Hamiltonian combining parabolic dispersion and Rashba spin-orbit interaction. Following Ref. [28] we consider the limit of large chemical potential in the superconductor and model it by neglecting the spin-orbit interaction and motion parallel to the junction. We then arrive at the effective Hamiltonian:

$$\begin{aligned} H = &\left(\frac{\xi(y) p_x^2 + p_y^2}{2m} - \mu + \frac{m\xi(y)\alpha^2}{2\hbar^2} \right) \sigma_0 \tau_z \\ &+ \xi(y)\alpha(p_x \sigma_y - p_y \sigma_x)\tau_z \\ &+ \mathrm{Re}\left(\Delta(x,y)\right)\sigma_0\tau_x + \mathrm{Im}\left(\Delta(x,y)\right)\sigma_0\tau_y, \end{aligned} \tag{3.1}$$

with $p_{x/y} = -i\hbar\partial_{x/y}$, m the effective electron mass, μ the chemical potential, α the Rashba spin-orbit interaction strength and $\Delta(x, y)$ the superconducting gap. The indicator function $\xi(y) = 0$ under the superconductor, and $\xi(y) = 1$ otherwise. Finally, σ_i and τ_i are the Pauli matrices in the spin and the electron-hole space. Since the superconductors carry current, their phase depends linearly on x, resulting in the induced gap:

$$\Delta(x,y) = \begin{cases} \Delta_0 \exp(-2\pi i x/\lambda_T) & y > W/2, \\ 0 & |y| < W/2, \\ \Delta_0 \exp(2\pi i x/\lambda_B) & y < -W/2, \end{cases} \tag{3.2}$$

(3.3)

with W the width of the Josephson junction, λ_T and λ_B the winding lengths of the superconducting phase in the two superconductors, and Δ_0 the magnitude of the induced superconducting gap.

To characterize the topological properties of the setup, we consider a quasi-1D translationally invariant system with a period equal to the smallest length commensurate with both λ_T and λ_B. We apply the tight-binding approximation to the Hamiltonian (2.5a), and study the band structure of the resulting tight-binding Hamiltonian as a function of the Bloch momentum κ using the Kwant software package [29].

CREATING A TOPOLOGICAL PHASE

We illustrate the appearance of the topological phase by including the necessary ingredients one by one.

PHASE WINDING AND INVERSION SYMMETRY

For a qualitative illustration we choose the following parameter values, unless specified otherwise. The effective electron mass is $m = 0.04m_e$, with m_e the free electron mass, $W = 150\,\text{nm}$, $\lambda_T = \lambda_B = 370\,\text{nm}$, the width of the superconductors equals 100 nm. The chemical potential $\mu = 0.125\,\text{meV}$ results in the Fermi wavelength $\lambda_F = 550\,\text{nm}$, the coherence length inside the superconductor is 100 nm, at this chemical potential that implies $\Delta_0 = 0.22\,\text{meV}$, and finally $\alpha = 10\,\text{peVm}$ corresponds to the spin-orbit length $l_{so} \equiv \hbar^2/(\alpha m) = 190\,\text{nm}$.

To confirm the presence of an effective Zeeman splitting we compute an example band structure Fig. 3.2 using the Fermi-wavelength $\lambda_F = 710\text{nm}$. It does have the expected avoided crossing at $\kappa = 0$. Further, this band structure has reflection symmetry around $\kappa = 0$, because of the inversion symmetry of the Hamiltonian $[H, I] = 0$, with the inversion symmetry operator $I = \delta(x + x')\delta(y + y')\sigma_z$. Since choosing $\lambda_T \neq \lambda_B$ breaks the inversion symmetry, it may may close the band gap at finite momentum, as illustrated in Fig. 3.3, where we chose $2\lambda_T = \lambda_B = 700\text{nm}$. Therefore, in order to maximize the parameter range supporting gapped spectrum, we only consider the case $\lambda_T = \lambda_B \equiv \lambda$, so that I is preserved.

BREAKING THE CHARGE-MOMENTUM CONSERVATION LAW

The band structure in Fig. 3.2 resembles that of a nanowire with spin-orbit interaction and Zeeman field [14, 15]. Therefore by analogy it is natural to expect that tuning the

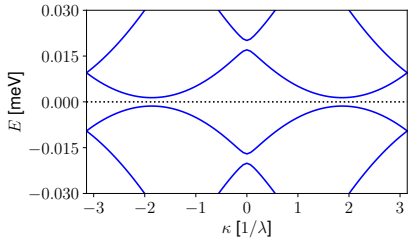

Figure 3.2: Band structure with spin-orbit interaction: the bands are shifted in momentum space. The direction of the shift depends on the spin. In addition there is an avoided crossing at zero momentum, showing the effective Zeeman interaction.

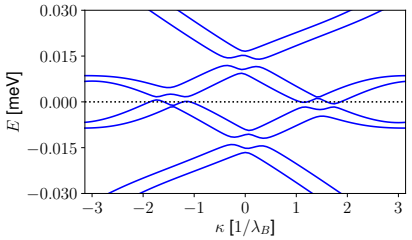

Figure 3.3: Band structure with broken inversion symmetry, because $2\lambda_T = \lambda_B$. Physically this means that the supercurrent densities in the two superconductors are different, such that there is a net supercurrent flowing parallel to the junction.

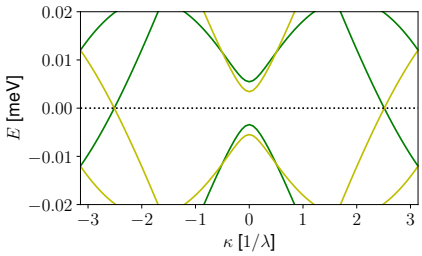

Figure 3.4: Band structure with the Fermi level tuned inside the avoided crossing at $\kappa = 0$. The bands are colored according to the eigenvalue of O (eq. 3.4).

chemical potential such that the two spin states at $\kappa = 0$ have opposite energies should result in a topologically nontrivial band structure supporting MBS. Instead we observe a gapless band structure shown in Fig. 3.4, where the band gap closes at a finite κ.

In order to identify the reason for the absence of a gap in the topologically nontrivial regime it is instructive to visualize the Hamiltonian at a fixed Bloch momentum. We distinguish groups of states by their charge and their discrete dimensionless momentum $n \equiv \lambda(k-\kappa)/2\pi$, where k is the momentum. We represent the Hamiltonian as a graph with nodes corresponding to states with different charge and n, and edges corresponding to nonzero matrix elements. The Hamiltonian of Eq. (2.5a) then corresponds to the graph shown in Fig. 3.5. The two disconnected subgraphs correspond to the two eigenspaces of the charge-momentum parity operator:

$$O = (-1)^n \tau_z, \tag{3.4}$$

which commutes with the Hamiltonian.

The importance of the charge-momentum parity conservation becomes apparent

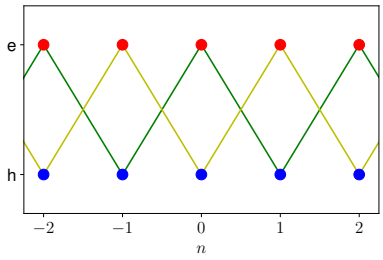

Figure 3.5: Visual representation of the Hamiltonian. The dots are groups of states, the lines denote couplings between members of these groups. The two disconnected graphs imply a conservation law.

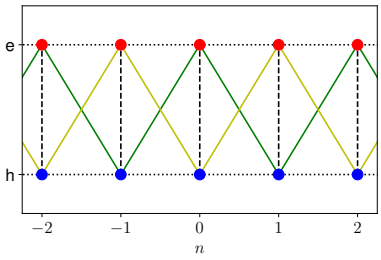

Figure 3.6: Visualization of the Hamiltonian like Fig. 3.5, with added couplings that break the charge-momentum conservation law. The dashed lines correspond to the coupling a superconductor without supercurrent would introduce. The dotted lines represent the coupling that a periodic potential induces.

from the symmetry relation

$$\{PI, O\} = 0, \tag{3.5}$$

with the particle-hole symmetry operator $P = \tau_y \sigma_y K$ and K complex conjugation. For each eigenstate $|\Psi\rangle$ of the Hamiltonian with given energy E and charge-momentum parity O, there is an eigenstate $PI|\Psi\rangle$ with $-E$ and $-O$. Topological phase transitions occur whenever such a pair of states crosses zero energy at $\kappa = 0$ or $\kappa = \pi$. In the topologically nontrivial regime the difference of the number of states with positive E and O at $\kappa = 0$ and those at $\kappa = \pi$ is odd. Therefore the topological phase requires at least one band with positive O (and its particle-hole symmetric partner with negative O) to cross zero energy between $\kappa = 0$ and $\kappa = \pi$. This prohibits a gapped topologically nontrivial phase as long as O is conserved. We confirm our argument by checking that the bands crossing at $E = 0$ in Fig. 3.4 have opposite charge-momentum parities.

Since a gap is required for topologically protected MBS, the Hamiltonian requires additional terms breaking the charge-momentum parity conservation. This is achieved by adding a periodic potential

$$\delta V = V \cos(2\pi x/\lambda)\sigma_0 \tau_z, \tag{3.6}$$

with V the amplitude of the additional periodic modulation to the Hamiltoanian. An alternative option is adding an extra superconductor carrying no supercurrent. In order to preserve the inversion symmetry, we add the additional superconductor in the middle of the junction, as sketched in Fig. 3.7, so that $\Delta(x, y)$ becomes:

$$\Delta(x, y) = \begin{cases} \Delta_0 \exp(-2\pi i x/\lambda) & y > W/2, \\ \Delta' & w/2 > |y|, \\ 0 & w/2 < |y| < W/2, \\ \Delta_0 \exp(2\pi i x/\lambda) & y < -W/2, \end{cases} \tag{3.7}$$

where w is the width of the middle superconductor and Δ' its gap. These Hamiltonian terms couple the eigensubspaces of O, as depicted in Fig. 3.6.

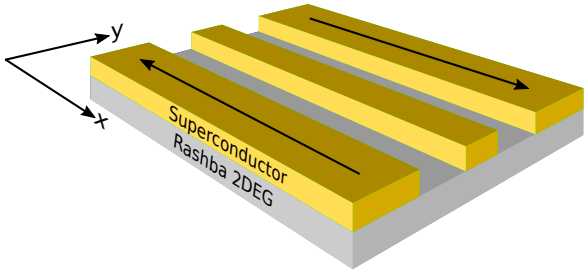

Figure 3.7: Sketch of the system like Fig. 3.1, but with an additional superconductor in the middle of the junction.

We verify that adding either coupling reopens the gap and makes the system topologically nontrivial. Specifically choosing $V = 0.08\,\text{meV}$, or $\Delta' = 0.04\,\text{meV}$ and $w = 10\,\text{nm}$, results in the band structures shown in Fig. 3.8. We verify that in both cases the system is topologically nontrivial by attaching a normal lead and using the scattering formalism to compute the topological invariant [30].

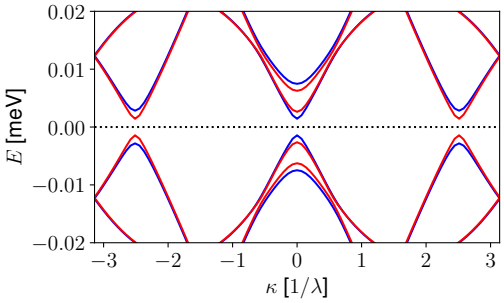

Figure 3.8: Example band structures of topologically nontrivial systems. The band structure plotted in blue corresponds to a system with a periodic potential. The red lines are a band structure of a system with a third superconductor.

OPTIMIZING THE TOPOLOGICAL GAP

After proving that the supercurrents may support a topological phase, we proceed by identifying the parameter regime corresponding to the largest topological gap and by discussing the experimental limitations.

SHORT JUNCTION FORMALISM

In order to further simplify the optimization procedure we focus on the strong coupling or *short junction* regime, when the superconducting gap only enters the quasiparticle

spectrum as an overall prefactor [28] and approximate the superconductors on both sides of the junction as infinitely wide.

Within the scattering formalism [28], the spectrum of a Josephson junction is obtained as a solution of the bound state condition

$$r_A(E=0)S(E)\Psi = \chi\Psi, \tag{3.8}$$

with S the junction's scattering matrix describing the scattering between the two superconducting terminals, the Andreev reflection matrix $r_A(E) = \chi^*(\tau_x \cos\phi + \tau_y \sin\phi)$, and the energy-dependent phase factor $\chi \equiv \exp[-i \arccos(E/\Delta_0)]$. Here Ψ is the vector of the amplitudes of the electron and hole waves incoming into the scattering region from the superconducting terminals. Because we neglect the motion parallel to the interface in the superconductor and because ϕ is position-dependent, the Andreev reflection matrix contains a mode-dependent phase shift. In the short junction regime the Thouless energy $E_T \gg \Delta_0$, and therefore $S(E) \approx S(0)$ for $E \lesssim \Delta_0$, making Eq. (3.8) a conventional eigenvalue problem in χ, with $\mathrm{Re}\,\chi = E/\Delta_0$.

The short junction formalism is a good approximation of aluminium-based hybrid setups because the typical value of $E_{\mathrm{Th}} \sim 2\,\mathrm{meV} \gg \Delta_0$. Since this formalism does not require explicit simulation of the superconducting electrodes, it is also more numerically efficient. Finally, because in the short junction limit, the superconducting gap enters the spectrum exclusively as an overall prefactor, this approximation provides additional insight in the optimization procedure.

PROTOCOL FOR TUNING THE SYSTEM PARAMETERS

With the superconducting gap dropping out of the topological phase diagram, we turn to optimize the remaining parameters: the spin-orbit length l_{so}, W, λ and μ, as well as the strength of the terms breaking O, controlled by either the width of the middle superconductor w and its gap Δ', or the amplitude V of the periodic potential.

Because in an experiment it is impossible to modify the spin-orbit length within a single sample, we do not search for the optimal value of l_{so}, but instead use a qualitative argument. Similarly to using Δ_0 as an energy scale, l_{so} can act as a length scale. Therefore we can choose it arbitrarily and optimize the other parameters with respect to it. This includes μ and Δ' since they can be translated into length scales, namely the Fermi-wavelength and the coherence length.

Starting from a gapless topologically nontrivial band structure and gradually increasing the strength of the O-breaking terms, the topological gap should initially increase. After that, when the O-breaking terms become too strong, they will close the gap again, because the O-breaking terms do not only cause level repulsions between the conduction band and its antiparticle band, but also between the conduction band and higher bands. Therefore, we expect to find the largest topological gap starting from a system where E_{max}, the energy window around zero energy that only contains one band and its antiparticle band, is maximal Fig. 3.9.

We use this criterion to find the optimal values of W, μ and λ. Especially the relation $l_{so} \approx W$ is important, because the width of the junction is also not adjustable after creating the probe and therefore has to be taken into account during the fabrication process. The other two parameters μ and λ on the other hand can be tuned by varying an overall

backgate voltage and the supercurrent passed through the superconducting electrodes. In addition to the tuneability of these parameters, maximizing $E_{\max}$ requires the ability to measure it, which is possible using a conductance measurement along the junction.

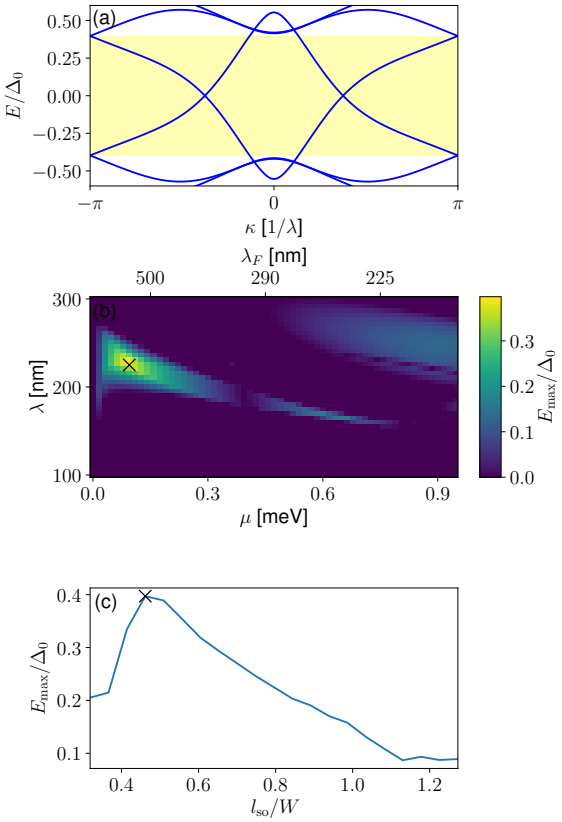

Figure 3.9: (a) The band structure with the maximal $E_{\max}$. The single channel window is highlighted in yellow. (b) Size of the single channel window for different μ and λ at the optimal width ($W \approx 2l_{so}$, in this case $W = 150\,\text{nm}$ and $l_{so} = 70\,\text{nm}$), with a marker at the maximum. (c) Size of the single channel window for different spin-orbit length with μ and λ optimized for each value of l_{so} individually. The maximum is at $W \approx 2l_{so}$.

Finally we optimize the topological gap Δ_T by varying the terms breaking O. Therefore, we either vary the amplitude of the periodic potential, or the width w of the middle superconductor, while keeping $\Delta' = 0.22\,\text{meV}$. In agreement with our expectations, the topological gap exhibits a nonmonotonous behavior, reaching the maximum of $0.015\Delta_0$ at $w = 15\,\text{nm}$ or a maximum of $0.15\Delta_0$ at $V = 0.065\,\text{meV}$, as shown in Fig. 3.10.

This final step, adjusting the terms breaking O, is problematic in an experiment. In the setup with a third superconductor, neither Δ' nor w are adjustable after fabricating the probe. Even though in theory it is possible to estimate the required w based on $E_{\max}$ and the coherence length under the superconductor in the 2DEG, we do not know these parameters in a real system during the fabrication. The system with a periodic potential has

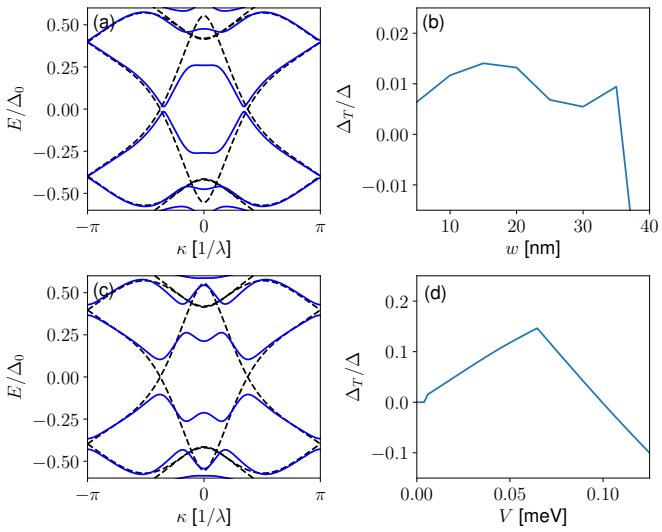

Figure 3.10: (a) The topologically nontrivial band structure with the maximal gap obtained using a third superconductor. (b) The size of the band gap for varying widths of the third supercondutor times 1 for topologically nontrivial systems and -1 otherwise. (c) The topologically nontrivial band structure with the maximal gap obtained using a periodic potential. (d) Like (b), only varying the potential instead of a third superconductor.

a similar problem. In opposition to the period of δV, the winding of the superconducting phase, λ may be freely tuned by varying the supercurrent in the electrodes. Applying a periodic potential δV requires a periodic pattern of electrostatic gates, and its period is then fixed by the period of that gate pattern. But at the same time it must be equal to λ, therefore using the periodic potential to open the topological gap removes λ as a tuning parameter, and it introduces an extra problem of tuning the supercurrent so that the period of δV matches λ.

To finish the discussion of all parameters, we revisit the parameters that we used as scales. Since Δ_0 is the energy scale in the short junction limit, large Δ_0 are preferrable as long as $E_T \ll \Delta_0$. But even if the superconducting gap is larger than in the short junction limit, it can not be detrimental to the topological gap, because the short junction approximation still holds for states with low energies compared to the Thouless energy. In order to maximize the Thouless energy small W, and therefore short l_{so}, are preferrable.

DISCUSSION

In summary, we proved that the winding of a superconducting phase is a sufficient source of time-reversal symmetry breaking to create MBS in absence of an external magnetic field. By performing symmetry analysis we have identified the inversion symmetry and the breaking of the charge-momentum parity conservation law as the necessary ingredients for tuning the system into a gapped topological regime. We further established that an optimal parameter choice creates the topological gap comparable to 10% of the parent superconducting gap, using a periodic potential and comparable to 1% using a third

superconductor (Fig. 3.10).

The only magnetic field in the system is caused by the supercurrents in the electrodes. To find an order of magnitude of the magnetic field, we calculate these currents: $I = hdw_{sc}/(\lambda_L^2 \mu_0 2e\lambda)$, where d is the thickness of the superconductor, w_{sc} its width, λ_L the London penetration depth, and μ_0 the vacuum permeability. Then we approximate the magnetic field as $B = \frac{\mu_0 I}{2\pi w_{sc}}$, therefore an example of $d = 10\,\text{nm}$, $\lambda_L = 50\,\text{nm}$ (aluminum), and $\lambda = 250\,\text{nm}$ yields a very weak magnetic field $B \sim 5\,\text{mT}$.

To verify that the back-action of the junction on the superconducting electrodes is negligible, we compare the critical current of the junction with the current carried by the electrodes. We estimate the critical current (in the short junction limit) to be $I_c = 2ne\Delta_0/h$, where n is the number of modes $n = l/\lambda_F$, with l the length of the junction in x-direction. With the same parameters as before, $\lambda_F \approx 500\,\text{nm}$ and $\Delta_0 = 0.22\,\text{meV}$, $I \gg I_c$ reduces to $8 \cdot 10^5 w_{sc} \gg l$. Since there are no constraints on w_{sc} it is always possible to fulfill this kind of inequality. The large dimensionless factor makes it easier.

Our procedure for identifying the optimal topological gap by finding optimal w after fixing μ and λ is impractical to apply experimentally. Apart from that, the tuning may be performed using standard measurement techniques—for instance tunneling spectroscopy—employed to identify a topological phase and measure the topological gap.

REFERENCES

[1] A. Y. Kitaev, *6. Quantum computing: Unpaired Majorana fermions in quantum wires,* Physics Uspekhi **44**, 131 (2001).

[2] A. Stern, *Non-abelian states of matter,* Nature **464**, 187 (2010).

[3] R. F. Service, *Search for majorana fermions nearing success at last?* Science **332**, 193 (2011).

[4] F. Wilczek, *Majorana returns,* Nat. Phys. **5**, 614 (2009).

[5] H. Bombin, *Topological order with a twist: Ising anyons from an abelian model,* Phys. Rev. Lett. **105**, 030403 (2010).

[6] N. Read and G. Moore, *Fractional quantum hall effect and nonabelian statistics,* Progr. Theor. Phys. Supp. **107**, 157 (1992).

[7] C. Nayak, S. H. Simon, A. Stern, M. Freedman, and S. Das Sarma, *Non-abelian anyons and topological quantum computation,* Rev. Mod. Phys. **80**, 1083 (2008).

[8] J. Alicea, *New directions in the pursuit of Majorana fermions in solid state systems,* Rep. Prog. Phys. **75**, 076501 (2012).

[9] M. Leijnse and K. Flensberg, *Introduction to topological superconductivity and Majorana fermions,* Semiconductor Science and Technology **27**, 124003 (2012).

[10] C. W. J. Beenakker, *Search for Majorana fermions in superconductors,* Annual Review of Condensed Matter Physics **4**, 113 (2013).

[11] T.-P. Choy, J. M. Edge, A. R. Akhmerov, and C. W. J. Beenakker, *Majorana fermions emerging from magnetic nanoparticles on a superconductor without spin-orbit coupling,* Phys. Rev. B **84**, 195442 (2011).

[12] J. Li, T. Neupert, B. A. Bernevig, and A. Yazdani, *Manipulating Majorana zero modes on atomic rings with an external magnetic field,* Nature Communications **7**, 10395 (2016).

[13] M. Ruby, B. W. Heinrich, Y. Peng, F. von Oppen, and K. J. Franke, *Exploring a proximity-coupled Co chain on Pb(110) as a possible Majorana platform,* Nano Lett. **17**, 4473 (2017).

[14] R. M. Lutchyn, J. D. Sau, and S. Das Sarma, *Majorana fermions and a topological phase transition in semiconductor-superconductor heterostructures,* Phys. Rev. Lett. **105**, 077001 (2010).

[15] Y. Oreg, G. Refael, and F. von Oppen, *Helical liquids and Majorana bound states in quantum wires,* Phys. Rev. Lett. **105**, 177002 (2010).

[16] V. Mourik, K. Zuo, S. M. Frolov, S. R. Plissard, E. P. A. M. Bakkers, and L. P. Kouwenhoven, *Signatures of majorana fermions in hybrid superconductor-semiconductor nanowire devices,* Science **336**, 1003 (2012).

[17] A. Das, Y. Ronen, Y. Most, Y. Oreg, M. Heiblum, and H. Shtrikman, *Zero-bias peaks and splitting in an Al-InAs nanowire topological superconductor as a signature of Majorana fermions,* Nat. Phys. **8**, 887 (2012).

[18] M. T. Deng, C. L. Yu, G. Y. Huang, M. Larsson, P. Caroff, and H. Q. Xu, *Anomalous zero-bias conductance peak in a Nb–InSb nanowire–Nb hybrid device,* Nano Lett. **12**, 6414 (2012).

[19] A. D. K. Finck, D. J. Van Harlingen, P. K. Mohseni, K. Jung, and X. Li, *Anomalous modulation of a zero-bias peak in a hybrid nanowire-superconductor device,* Phys. Rev. Lett. **110**, 126406 (2013).

[20] S. M. Albrecht, A. P. Higginbotham, M. Madsen, F. Kuemmeth, T. S. Jespersen, J. Nygård, P. Krogstrup, and C. M. Marcus, *Exponential protection of zero modes in majorana islands,* Nature (London) **531**, 206 (2016).

[21] H. Zhang, Ö. Gül, S. Conesa-Boj, K. Zuo, V. Mourik, F. K. de Vries, J. van Veen, D. J. van Woerkom, M. P. Nowak, M. Wimmer, D. Car, S. Plissard, E. P. A. M. Bakkers, M. Quintero-Pérez, S. Goswami, K. Watanabe, T. Taniguchi, and L. P. Kouwenhoven, *Ballistic Majorana nanowire devices,* arXiv:1603.04069 (2016).

[22] A. Romito, J. Alicea, G. Refael, and F. von Oppen, *Manipulating Majorana fermions using supercurrents,* Phys. Rev. B **85**, 020502 (2012).

[23] F. Pientka, A. Keselman, E. Berg, A. Yacoby, A. Stern, and B. I. Halperin, *Topological superconductivity in a planar Josephson junction,* Phys. Rev. X **7**, 021032 (2017).

[24] M. Hell, M. Leijnse, and K. Flensberg, *Two-dimensional platform for networks of Majorana bound states,* Phys. Rev. Lett. **118**, 107701 (2017).

[25] B. van Heck, S. Mi, and A. R. Akhmerov, *Single fermion manipulation via superconducting phase differences in multiterminal Josephson junctions,* Phys. Rev. B **90**, 155450 (2014).

[26] L. Fu and C. L. Kane, *Superconducting proximity effect and Majorana fermions at the surface of a topological insulator,* Phys. Rev. Lett. **100**, 096407 (2008).

[27] A. Cook and M. Franz, *Majorana fermions in a topological-insulator nanowire proximity-coupled to an s-wave superconductor,* Phys. Rev. B **84**, 201105 (2011).

[28] D. Sticlet, B. Nijholt, and A. Akhmerov, *Robustness of majorana bound states in the short-junction limit,* Phys. Rev. B **95**, 115421 (2017).

[29] C. W. Groth, M. Wimmer, A. R. Akhmerov, and X. Waintal, *Kwant: a software package for quantum transport,* New J. Phys. **16**, 063065 (2014).

[30] I. C. Fulga, F. Hassler, and A. R. Akhmerov, *Scattering theory of topological insulators and superconductors,* Phys. Rev. B **85**, 165409 (2012).

4

DETECTING MAJORANA NONLOCALITY USING STRONGLY COUPLED MAJORANA BOUND STATES

INTRODUCTION

The ability to create, detect, and manipulate Majorana bound states (MBS) is one of the current research goals of condensed matter physics. MBS are the simplest non-Abelian anyons, and a potential building block of a noise-tolerant quantum computer [1–3]. The experiments so far focus on identifying local properties of MBS, such as the zero bias peak in conductance [4], the 4π-periodic Josephson effect [5, 6], or the local maximum in the zero energy density of states [7]. Observing the local signatures of MBS cleanly is an important milestone, but it has its limitations since known local signatures of MBS can be mimicked by regular Andreev bound states subjected to sufficient fine-tuning. For instance, a topologically protected level crossing responsible for the 4π-periodic Josephson effect can be indistinguishable from an unprotected avoided level crossing [8], and a zero bias peak may have nontopological origins [9, 10].

Therefore an unambiguous detection of Majorana fermions requires detecting their nonlocal properties in a falsifiable manner. Braiding statistics of MBS can serve as one such experiment, but even a minimal braiding setup [11] requires time domain manipulation of a complicated superconducting circuit hosting six MBS, or of a large array of gate voltages [12].

Another consequence of the nonlocal nature of MBS is their transport property called electron teleportation [13], discovered by L. Fu. It occurs in superconducting islands hosting MBS and having a finite charging energy. If there are leads coupled to the MBS, Majorana teleportation provides coherent transport of single fermionic excitations be-

tween the leads. The direct signatures of electron teleportation include the period doubling of a Fabry-Perot interferometer [13, 14] and the periodicity change of the ground state energy of a ring made out of a topological superconductor [15]. More advanced consequences of electron teleportation are the appearance of a high symmetry Kondo problem in multi-lead scattering off an island hosting MBS [16] and exotic many-body phases of a network of such islands.

A simple physical interpretation of the electron teleportation is the appearance of an extra term in the Hamiltonian proportional to $i^{n/2}\prod_0^n \gamma_i$ in the presence of charging energy. [1] In other words, the charging energy couples all the MBS γ_i belonging to the island. If there are only two MBS present, this coupling becomes identical to a direct overlap of low energy quasiparticle wave functions in a superconductor due to finite size effects. In other words, charging energy coherently transports a single fermion from one MBS to another. Since it does not require a direct wave function overlap, it is nonlocal. A falsifiable detection of this nonlocal coupling therefore requires verification that it is coherent, that it is single fermion transport, and that it is not arising due to an actual wave function overlap.

The aim of our work is to present and analyze a setup that allows one to detect this coupling while not having any unnecessary ingredients. Our proposed setup has an additional counter-intuitive benefit of not requiring creation of decoupled MBS, unlike required in the previous proposals [13, 14]. This makes our setup perfectly suited for quantum spin Hall insulator (QSHE)-superconductor hybrid structure [5], where isolation of MBS requires creation of magnetic tunnel barriers and remains an open experimental challenge. In addition our setup allows one to distinguish the electron teleportation from local coupling through the superconductor therefore providing the falsifiability of the effect.

THE SETUP

SYSTEM LAYOUT AND QUALITATIVE ARGUMENTS

We begin by considering each requirement for detection of the nonlocal coupling and arguing how to achieve it in the simplest fashion. Once again: we aim to design a setup that has to detect coherent transport of single fermions through a topological superconductor. Additionally it has to ensure that the origin of this transport is not due to quasiparticle current caused by a normal conduction channel.

Coherence of quasiparticle transport is most directly checked by a two-path interferometer. In order to test the electron teleportation, one arm must include the topological superconductor hosting MBS, while the other reference arm should be a normal region. The coherence of quasiparticle transport through such an interferometer manifests in periodic dependence of observed properties on the magnetic flux threaded through it.

The charge of the interfering particle manifests in the flux periodicity of the interferometer's conductance and spectrum. Therefore in the presence of a conduction channel for single fermionic quasiparticles we expect an h/e periodicity of the observed signal, or

[1] The original publication of L. Fu, Ref. [13] uses a gauge choice that contains unphysical degrees of freedom and a fermion parity constraint, and therefore does not contain the MBS coupling term explicitly. We use a physically equivalent gauge of Ref. [15].

Aharonov-Bohm effect. This allows us to distinguish fermion transport from Cooper pair transport flux dependence with period $h/2e$ that corresponds to Josephson effect [17–19].

The 4π-periodic Josephson effect arising from a fermion parity anomaly [5] may obscure the nonlocal coupling by creating a signal with the same periodicity. To suppress this effect, the interferometer must be coupled to a normal metallic reservoir draining out of equilibrium fermionic excitations. On the other hand, the coupling of the superconductor to an external reservoir cannot have high transparency, since then a low RC-time suppresses the Coulomb blockade and the nonlocal coupling. These two requirements are satisfied if a tunnel junction is present between the superconductor and the normal reservoir. In the setups of Refs. [13, 14] the tunnel barrier separates the two interferometer arms and suppresses the coupling strength E_{M} through the reference arm. Locating the tunnel barrier directly between the normal interferometer arm and the metallic lead avoids the coupling strength suppression and simplifies the setup [2].

The final requirement our setup should satisfy is the need to rule out the conventional quasiparticle transport through the nontrivial part of the interferometer. Since the quasiparticle transport appears also without Coulomb energy, suppressing the latter and observing disappearance of the h/e interference signal allows one to conclude that the interference is of nonlocal origin. We propose to use a standard technique [20] to controllably suppress the Coulomb energy E_C by adding a flux- or gate-tunable [21] Josephson coupling E_{J} between the nontrivial interferometer arm and a superconducting reservoir. This leads to a renormalization [20] of the effective charging energy $\tilde{E}_C \propto \exp(-\sqrt{8E_{\mathrm{J}}/E_C})$ when $E_{\mathrm{J}} \gg E_C$.

We arrive at the setup shown in Fig. 4.1, that consists of an interferometer coupled to a normal lead by a tunnel junction and a superconducting lead by a tunable Josephson junction, for example a dc-SQUID. Every element in this system may only be replaced and not removed because all of them have a separate role in detection of nonlocal signatures of MBS. The effective low energy Hamiltonian of this system is

$$\begin{aligned} H_{\mathrm{eff}} &= i\gamma_1\gamma_2\left[E_{\mathrm{M}}\cos(\pi\Phi/\Phi_0) + \tilde{E}_C\cos(\pi n_I)\right] \\ &\equiv i\gamma_1\gamma_2\Delta E, \end{aligned} \tag{4.1}$$

with γ_1, γ_2 the Majorana operators, n_I the induced charge of the interferometer, Φ the flux through it, and $\Phi_0 = h/2e$ the superconducting flux quantum. When $\tilde{E}_C$ is finite, the spectrum of this Hamiltonian is h/e-periodic in Φ, but it becomes $h/2e$-periodic when $\tilde{E}_C$ is suppressed by increasing E_{J}. A corresponding Hamiltonian of a trivial Josephson junction containing a single Andreev bound state has a form $H = [E_J(\Phi) + E_C]a^\dagger a$, with E_J a $h/2e$-periodic function of Φ and a the annihilation operator of the Andreev bound state, so that its periodicity is always constant. Quasiparticles tunneling through the superconductor give rise to a term $it_{\mathrm{SC}}\gamma_1\gamma_2$ with t_{SC} the tunneling amplitude, and keep the spectrum h/e-periodic regardless of $\tilde{E}_C$. As we will show in more detail, measuring either the supercurrent circulating in the interferometer or the conductance between the normal and the superconducting leads as a function of flux reveals the periodicity of the

[2] Two possible strategies to realize the normal lead weakly coupled to a quantum spin Hall edge are either creating a dielectric-normal metal tunnel junction, or a gate-tunable narrow constriction in the quantum spin Hall edge itself.

spectrum and provides an observable signature of the nonlocal properties of Majorana fermions.

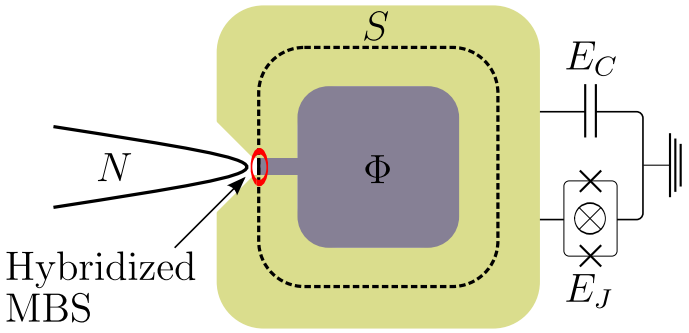

Figure 4.1: Setup consists of a QSHE insulator (dark gray) with its edge (dashed line) partially covered by a superconducting ring. The proximity-induced gap in the QSHE edge forms two hybridized MBS at the part of the edge not covered by the superconductor. A tunable Josephson junction couples the superconducting ring to the superconducting lead. Finally, the normal lead weakly couples to the quantum spin Hall edge in the junction region.

EFFECTIVE HAMILTONIAN

The effective Hamiltonian of the Coulomb Majorana interferometer of Fig. 4.1 is

$$H = H_{\mathrm{CPB}} + \sum_{k,\sigma} \varepsilon(k,\sigma) c^{\dagger}_{k,\sigma} c_{k,\sigma} + H_{\mathrm{c}}. \tag{4.2}$$

Here H_{CPB} is the Cooper pair box Hamiltonian:

$$\begin{aligned} H_{\mathrm{CPB}} = E_C \left(-2i\partial_\phi + n_I + p/2\right)^2 - E_{\mathrm{J}} \cos\phi \\ - E_{\mathrm{M}} p \cos\left(\pi\Phi/\Phi_0\right), \end{aligned} \tag{4.3}$$

and H_{c} is the coupling Hamiltonian between the Cooper pair box and the normal lead

$$H_{\mathrm{c}} = \sum_{k,\sigma} \left[c_{k,\sigma} e^{i(1-p)\phi/2} (t_{\sigma,1}\gamma_1 + t_{\sigma,2}\gamma_2) + h.c. \right]. \tag{4.4}$$

Here ϕ is the superconducting phase of the island, and $p = i\gamma_1\gamma_2$ is the fermion parity of the interferometer. Finally, the tunnel coupling between the lead modes and the MBS is $t_{\sigma,i}$, and it may depend on ϕ.

Rewriting the Hamiltonian in the eigenbasis of the Cooper-pair box yields:

$$H_{\mathrm{CPB}} = E_\Phi(p, b^\dagger b), \tag{4.5a}$$

$$H_{\mathrm{c}} = \sum_{k,\sigma,n} \left[c_{k,\sigma} \left(t_{\sigma,1}\gamma_1 + t_{\sigma,2}\gamma_2\right) \left[\xi^{+}_{n}(p, b^\dagger b)(b^\dagger)^n + \xi^{-}_{n}(p, b^\dagger b) b^n \right] + \mathrm{h.c.} \right], \tag{4.5b}$$

$$\xi^{\pm}_{n}(p,m) \equiv \langle m \pm n, -p | e^{i(1-p)\phi/2} | m, p \rangle. \tag{4.5c}$$

Here we introduced the eigenenergies of the Cooper-pair box $E_\Phi(i\gamma_1\gamma_2, b^\dagger b)$ and the ladder operators of the Cooper-pair box b and $b^\dagger$. An electron/hole tunneling into the

superconducting ring can create excitations in the Cooper-pair box. In the Eq. (4.5) this is expressed by the transition amplitudes ξ between the states $|n,p\rangle$, with n the number of Cooper pair box excitations, and p its fermion parity. In the following we calculate ξ and $E(i\gamma_1\gamma_2, b^\dagger b)$ numerically (for details of our numerical calculations see the Supplemental Material available with the manuscript).

READOUT

ZERO BIAS CONDUCTANCE

The observable steady-state properties in this system, such as conductance, in general have the same flux periodicity as the spectrum, and therefore should exhibit signatures of the nonlocal coupling. However, evaluating conductance at an arbitrary bias is an involved task and to simplify the calculation we focus on the zero bias. Since the quasiparticle lifetime in the interferometer is bounded from above by the inverse coupling to the lead, simultaneous tunneling events of multiple quasiparticles are suppressed at voltages $eV \ll |t|$. Therefore in this regime we may project the Hamiltonian onto the Hilbert space of a single fermionic excitation in order to simplify the problem. The basis states of the single fermion Hilbert space are:

$$|k,\sigma,e\rangle = c^\dagger_{k,\sigma}|\mathrm{gs}_{\mathrm{lead}}\rangle \otimes |\mathrm{gs}_{\mathrm{ring}}\rangle, \tag{4.6a}$$

$$|k,\sigma,h\rangle = c_{k,\sigma}|\mathrm{gs}_{\mathrm{lead}}\rangle \otimes |\mathrm{gs}_{\mathrm{ring}}\rangle, \tag{4.6b}$$

$$|n\rangle = (\gamma_1 + p_{\mathbf{gs}} i\gamma_2)(b^\dagger)^n|\mathrm{gs}_{\mathrm{lead}}\rangle \otimes |\mathrm{gs}_{\mathrm{ring}}\rangle. \tag{4.6c}$$

Here $|\mathrm{gs}_{\mathrm{lead}}\rangle$ and $|\mathrm{gs}_{\mathrm{ring}}\rangle$ are the ground states of the lead and the superconducting ring and $p_{\mathrm{gs}} = \langle \mathrm{gs}_{\mathrm{ring}}|p|\mathrm{gs}_{\mathrm{ring}}\rangle$. The indices e and h correspond to the electron and hole excitations. Projecting the Hamiltonian of Eq. (4.5) on the basis states of Eq. (4.6) we obtain:

$$\begin{aligned} H_{\mathrm{sqp}} = &\sum_{k,\sigma,\tau} |k,\sigma,\tau\rangle \tau_z \varepsilon(k,\sigma)\langle k,\sigma,\tau| \\ &+ \sum_n |n\rangle E_\Phi(-p_{\mathrm{gs}},n)\langle n| \\ &+ \sum_{k,\sigma,\tau,n} \left[|n\rangle \chi_n(p_{\mathrm{gs}},\tau)\langle k,\sigma,\tau| + h.c.\right], \end{aligned} \tag{4.7}$$

with

$$\chi_n(p,\tau) = \langle n|H_{\mathrm{c}}|k,\sigma,\tau\rangle. \tag{4.8}$$

Because of the doubling of degrees of freedom, χ also depends on the particle-hole index τ, even though the previously defined ξ does not.

We use the Mahaux-Weidenmüller formula to calculate the scattering matrix:

$$S = \frac{1 + i\pi W^\dagger (\sum_n |n\rangle E_\Phi(-p_{\mathrm{gs}},n)\langle n| - E)^{-1} W}{1 - i\pi W^\dagger (\sum_n |n\rangle E_\Phi(-p_{\mathrm{gs}},n)\langle n| - E)^{-1} W}. \tag{4.9}$$

Here E is the quasiparticle energy, and W is the coupling to the leads

$$W = \sqrt{\rho} \sum_{\sigma,\tau,n} |n\rangle \chi_n(p_{\mathrm{gs}},\tau)\langle k_E,\sigma,\tau|, \tag{4.10}$$

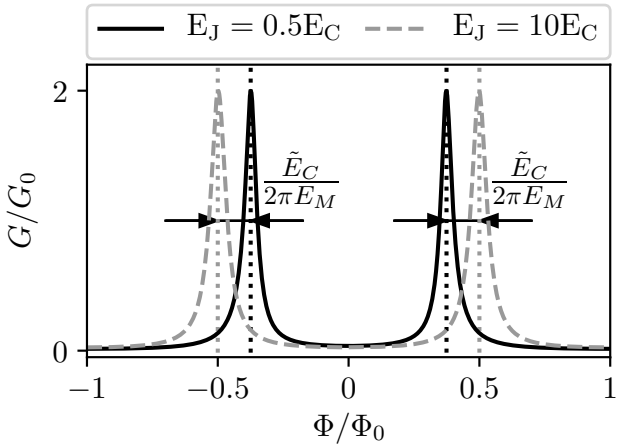

Figure 4.2: Conductance of the interferometer of Fig. 4.1 as a function of magnetic flux through the superconducting ring. It has an h/e periodicity if the effective charging energy $\tilde{E}_C$ is not suppressed. This numerical calculation follows App. A, where more than one excited state of the Cooper-pair box was taken into account.

with $\rho = (d\varepsilon/dk)^{-1}$ the density of states in the lead and k_E the momentum of excitations at energy E.

The differential conductance of the device is $G = 2G_0\|S_{he}\|^2$, with $G_0 = e^2/h$ the conductance quantum. If the tunneling amplitude is much smaller than the level spacing in the ring, H_S is well approximated by truncating it to the two lowest energy states with opposite fermion parity. It yields the conductance of a resonant Andreev level

$$G = \frac{2G_0}{1 + \Delta E^2/(\pi^2\|W\|^4)}, \tag{4.11}$$

with ΔE the splitting between the Majorana states, given by Eq. (4.1). The resonant peaks appear when $\Delta E = 0$, and therefore they have $h/2e$ periodicity in absence of the nonlocal coupling $\tilde{E}_C$ that changes into h/e when $\tilde{E}_C \gtrsim \|W\|$. Andreev conductance calculated using the full excitation spectrum of the ring is shown in Fig. 4.2, and it qualitatively agrees with the behavior of the two-level system. Since the flux dependence of the tunneling amplitudes has to have a period of $h/2e$, it does not impact our result.

MULTIPLE COOPER-PAIR BOX STATES

We relax the restriction that only takes one excited TSC ring state into account by considering the full spectrum of the Cooper-pair box. This yields

$$\sum_{\sigma,\sigma'} |S_{e,h,\sigma,\sigma'}|^2 = \sum_{\sigma,\sigma'} \left| \sum_{n,n'} \frac{4W_{n,\sigma,e}W^*_{n,\sigma',h}W_{n',\sigma,e}W^*_{n',\sigma',h}}{\left(\frac{i}{\pi}H_n + \|W_n\|^2\right)\left(\frac{-i}{\pi}H_{n'} + \|W_{n'}\|^2\right)} \right|, \tag{4.12}$$

with $H_n = E_\Phi(-p_{\mathrm{gs},n})$ and W_n is the n-th row of W. Since the relative phases between $W_{n,\sigma,\tau}$ and $W_{n,\sigma',\tau'}$ do not depend on n, we interchange the absolute value and the sum,

arriving at:

$$\sum_{\sigma,\sigma'} |S_{e,h,\sigma,\sigma'}|^2 = \sum_{n,n'} \frac{4\sum_{\sigma,\sigma'} |W_{n,\sigma,e} W_{n,\sigma',h} W_{n',\sigma,e} W_{n',\sigma',h}|}{\sqrt{\left(\frac{1}{\pi^2}E^2 + \|W_n\|^4\right)\left(\frac{1}{\pi^2}H_{n'}^2 + \|W_{n'}\|^4\right)}} \tag{4.13}$$

$$= \sum_{n,n'} \frac{\|W_n\|^2 \|W_{n'}\|^2}{\sqrt{\left(\frac{1}{\pi^2}H_n^2 + \|W_n\|^4\right)\left(\frac{1}{\pi^2}H_{n'}^2 + \|W_{n'}\|^4\right)}}. \tag{4.14}$$

Each of the excited states of the ring yields a Lorentzian contribution to the conductivity. In addition there are interference contributions for $n \neq n'$ that are suppressed if $|H_n - H_{n'}| \gg \|W_n\|^2$ or $|H_n - H_{n'}| \gg \|W_{n'}\|^2$.

SUPERCURRENT

Supercurrent carried by the interferometer in its ground state is also sensitive to the h/e periodicity of the Hamiltonian. It can be measured using SQUID magnetometry [22], and is thus an alternative pathway to observe the nonlocal coupling of Majoranas in the same interferometer. The current with h/e periodicity in the interferometer is an equilibrium phenomenon, and therefore different from the 4π-periodic Josephson effect, which is a non-equilibrium effect appearing due to a fermion parity anomaly. Since the coupling to the normal lead breaks the fermion parity conservation, it also suppresses the 4π-periodic Josephson effect in the interferometer.

We calculate the supercurrent in the ring using the definition

$$I = \frac{\partial E_{\text{gs}}}{\partial \Phi}, \tag{4.15}$$

with E_{gs} the ground state energy of the interferometer including the lead. We obtain E_{gs} by integrating the density of states

$$\frac{\partial n}{\partial E} = \frac{1}{2\pi}\text{ImTr}\frac{\partial S_{\alpha\beta}^\dagger}{\partial E} S_{\alpha\beta} \tag{4.16}$$

over negative quasiparticle energies. The ground state energy $E_{gs} = E_0 + E_1$ has contributions E_0 and E_1 from the lowest even and odd parity states (we neglect higher energy states).

$$E_0 = \int_{-\infty}^{0} (E + H_0)\text{Re}\left[\frac{1 - 2\pi i \|W\|^2 \left(H_1 - H_0 - E + i\pi\|W\|^2\right)^{-1}}{\|W\|^2 \left(H_1 - H_0 - E - i\pi\|W\|^2\right)^2}\right] dE, \tag{4.17}$$

$$E_1 = \int_{-\infty}^{0} (E + H_1)\text{Re}\left[\frac{1 - 2\pi i \|W\|^2 \left(H_0 - H_1 - E + i\pi\|W\|^2\right)^{-1}}{\|W\|^2 \left(H_0 - H_1 - E - i\pi\|W\|^2\right)^2}\right] dE. \tag{4.18}$$

Here H_0 and H_1 are the energies of the ring without level broadening. The expressions are equivalent, except for interchanging H_0 and H_1. We calculate the supercurrent using the definition $I = (2e/\hbar)\partial_\Phi E_{gs}$, so we need to calculate

$$\partial_\phi E_0 = \partial_\phi \int_{-\infty}^{H_0 - H_1} (E + H_1)\left[\frac{\|W\|^2}{E^2 + \pi^2\|W\|^4}\right] dE. \tag{4.19}$$

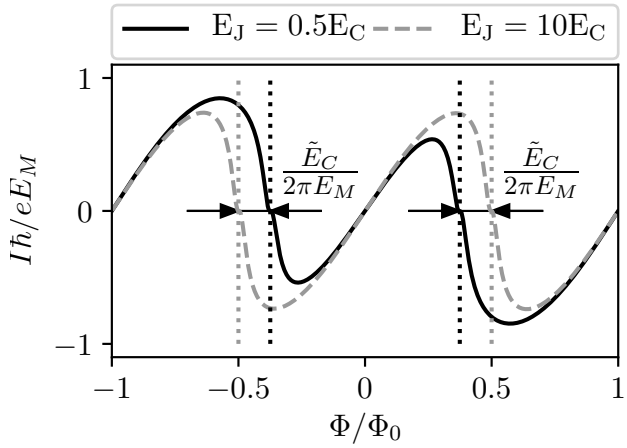

Figure 4.3: Supercurrent response of the interferometer of Fig. 4.1 to a magnetic flux through the superconducting ring. The current-flux relationship has a period of h/e if the effective charging energy is not negligible (black solid line). The Josephson $h/2e$ periodicity is restored when $\tilde{E}_C$ is suppressed by a large E_J. The supercurrent vanishes near the level crossing of the even and odd parity ring states; the low energy spectrum is symmetric around that flux.

Evaluating this integral and summing the contributions of both states yields

$$\partial_\phi E_{gs} = \frac{\|W\|^2 \left(\partial_\Phi H_0 - \partial_\Phi H_1\right)\left(H_0 - H_1\right)}{\left(H_0 - H_1\right)^2 + \pi^2 \|W\|^4} + \frac{1}{2}\left(\partial_\Phi H_1 + \partial_\Phi H_0\right) + \left(\partial_\Phi H_1 - \partial_\Phi H_0\right)\frac{1}{\pi}\arctan\left(\frac{H_0 - H_1}{\pi\|W\|^2}\right). \tag{4.20}$$

The resulting current-flux relationship is shown in Fig. 4.3, and in agreement with our expectations we observe that a finite effective capacitive energy makes supercurrent h/e-periodic.

PARAMETER VALUE ESTIMATION

The Majorana coupling in a short junction is comparable to the induced superconducting gap, $E_\mathrm{M} \approx \Delta$ [5]. Maximizing E_M is unfavorable for the observation of nonlocal coupling since the magnitude of the h/e-periodic component is proportional to $\tilde{E}_C/E_\mathrm{M}$. This argument together with the high availability of Al make it the optimal superconductor for observing the nonlocal coupling, and hence we use $E_\mathrm{M} \approx \Delta_\mathrm{Al} \approx 0.1$meV.

We assume that the capacitance is dominated by the coupling between the superconductor and the back-gate required to tune the quantum spin Hall device into the insulating regime. If the superconducting ring has a circumference $L = 3\mu$m, width $w = 0.1\mu$m, the distance to the gate is $d = 0.1\mu$m, and the gate dielectric has $\varepsilon_r = 10$, then the capacitance $C = \varepsilon_0\varepsilon_r Lw/d \approx 1.8$fF, or $E_C \approx 0.1$meV. The bare Coulomb energy is comparable to E_M, and therefore the Josepshon energy should change within a range between $E_J^\mathrm{Max} \gtrsim 10E_C$ and $E_J^\mathrm{Min} \lesssim E_C$.

Finally, the coupling strength of the normal lead to the MBS needs to be smaller

than the energy scales E_{M} and $\tilde{E}_C$, since otherwise the ground and excited states are overlapping due to level broadening.

SUMMARY

Due to the experimental progress towards the controllable creation of MBS, the planning of next steps in coherent control of MBS becomes a timely and relevant question. The currently existing proposals include braiding [11], a simpler nontopological qubit rotation [23], or a Bell inequality violation [24]. We have developed an alternative measurement aiming to probe the nonlocal properties of MBS focusing on simplicity and falsifiability. While being applicable to any implementation of MBS, our proposal has an additional advantage in quantum spin Hall devices, because it does not require spatial separation of MBS or inducing a magnetic gap in the edge states.

Our proposed setup is a Coulomb Majorana interferometer that measures a known phenomenon of Majorana teleportation through appearance of Aharonov-Bohm periodicity of conductance or supercurrent. According to our estimates such an interferometer can be made using existing fabrication techniques and provide a sufficiently strong nonlocal signal.

REFERENCES

[1] C. W. J. Beenakker, *Search for Majorana fermions in superconductors,* Ann. Rev. Cond. Mat. Phys. **4**, 113 (2013).

[2] J. Alicea, *New directions in the pursuit of Majorana fermions in solid state systems,* Rep. Prog. Phys. **75**, 076501 (2012).

[3] M. Leijnse and K. Flensberg, *Introduction to topological superconductivity and Majorana fermions,* Semicond. Sci. Technol. **27**, 124003 (2012).

[4] V. Mourik, K. Zuo, S. M. Frolov, S. R. Plissard, E. P. A. M. Bakkers, and L. P. Kouwenhoven, *Signatures of Majorana fermions in hybrid superconductor-semiconductor nanowire devices,* Science **336**, 1003 (2012).

[5] L. Fu and C. L. Kane, *Josephson current and noise at a superconductor/quantum-spin-Hall-insulator/superconductor junction,* Phys. Rev. B **79**, 161408 (2009).

[6] L. P. Rokhinson, X. Liu, and J. K. Furdyna, *The fractional a.c. Josephson effect in a semiconductor-superconductor nanowire as a signature of Majorana particles,* Nat. Phys. **8**, 795 (2012).

[7] S. Nadj-Perge, I. K. Drozdov, J. Li, H. Chen, S. Jeon, J. Seo, A. H. MacDonald, B. A. Bernevig, and A. Yazdani, *Observation of Majorana fermions in ferromagnetic atomic chains on a superconductor,* Science **346**, 602 (2014).

[8] J. D. Sau, E. Berg, and B. I. Halperin, *On the possibility of the fractional ac Josephson effect in non-topological conventional superconductor-normal-superconductor junctions,* arXiv:1206.4596 (2012).

[9] E. J. H. Lee, X. Jiang, R. Aguado, G. Katsaros, C. M. Lieber, and S. De Franceschi, *Zero-Bias anomaly in a nanowire quantum dot coupled to superconductors,* Phys. Rev. Lett. **109**, 186802 (2012).

[10] D. I. Pikulin, J. P. Dahlhaus, M. Wimmer, H. Schomerus, and C. W. J. Beenakker, *A zero-voltage conductance peak from weak antilocalization in a Majorana nanowire,* New J. Phys. **14**, 125011 (2012).

[11] T. Hyart, B. van Heck, I. C. Fulga, M. Burrello, A. R. Akhmerov, and C. W. J. Beenakker, *Flux-controlled quantum computation with Majorana fermions,* Phys. Rev. B **88**, 035121 (2013).

[12] J. Alicea, Y. Oreg, G. Refael, F. von Oppen, and M. P. A. Fisher, *Non-Abelian statistics and topological quantum information processing in 1d wire networks,* Nat. Phys. **7**, 412 (2011).

[13] L. Fu, *Electron teleportation via Majorana bound states in a mesoscopic superconductor,* Phys. Rev. Lett. **104**, 056402 (2010).

[14] J. D. Sau, B. Swingle, and S. Tewari, *Proposal to probe quantum nonlocality of Majorana fermions in tunneling experiments,* Phys. Rev. B **92**, 020511 (2015).

[15] B. van Heck, F. Hassler, A. R. Akhmerov, and C. W. J. Beenakker, *Coulomb stability of the 4π-periodic Josephson effect of Majorana fermions,* Phys. Rev. B **84**, 180502 (2011).

[16] B. Béri and N. R. Cooper, *Topological Kondo effect with Majorana fermions,* Phys. Rev. Lett. **109**, 156803 (2012).

[17] M. Büttiker and T. M. Klapwijk, *Flux sensitivity of a piecewise normal and superconducting metal loop,* Phys. Rev. B **33**, 5114 (1986).

[18] F. Pientka, A. Romito, M. Duckheim, Y. Oreg, and F. von Oppen, *Signatures of topological phase transitions in mesoscopic superconducting rings,* New J. Phys. **15**, 025001 (2013).

[19] F. Crépin and B. Trauzettel, *Flux sensitivity of quantum spin Hall rings,* Physica E **75**, 379 (2016).

[20] J. Koch, T. M. Yu, J. Gambetta, A. A. Houck, D. I. Schuster, J. Majer, A. Blais, M. H. Devoret, S. M. Girvin, and R. J. Schoelkopf, *Charge insensitive qubit design derived from the Cooper pair box,* Phys. Rev. A **76** (2007).

[21] T. Larsen, K. Petersson, F. Kuemmeth, T. Jespersen, P. Krogstrup, J. Nygård, and C. Marcus, *Semiconductor-nanowire-based superconducting qubit,* Phys. Rev. Lett. **115**, 127001 (2015).

[22] I. Sochnikov, L. Maier, C. A. Watson, J. R. Kirtley, C. Gould, G. Tkachov, E. M. Hankiewicz, C. Brüne, H. Buhmann, L. W. Molenkamp, and K. A. Moler, *Nonsinusoidal current-phase relationship in Josephson junctions from the 3d topological insulator HgTe,* Phys. Rev. Lett. **114**, 066801 (2015).

[23] B. van Heck, T. Hyart, and C. W. J. Beenakker, *Minimal circuit for a flux-controlled Majorana qubit in a quantum spin-Hall insulator,* Phys. Scr. **2015**, 014007 (2015).

[24] D. J. Clarke, J. D. Sau, and S. Das Sarma, *A practical phase gate for producing bell violations in majorana wires,* Phys. Rev. X **6**, 021005 (2016).

5

THE AC JOSEPHSON LASER

M. C. Cassidy, A. Bruno, S. Rubbert, M. Irfan, J. Kammhuber,
R. N. Schouten, A. R. Akhmerov and L. P. Kouwenhoven

INTRODUCTION

Josephson junctions are natural voltage to frequency converters via the AC Josephson effect. For a Josephson junction without an applied DC voltage bias, Cooper pairs tunnel coherently from one superconducting condensate to the other, resulting in a supercurrent flowing without dissipation. However, for a nonzero DC voltage bias (V_b) less than the superconducting energy gap, transport is prohibited unless the excess energy ($hf = 2eV_b$, with Planck's constant h, frequency f, and the charge of the Cooper pair $2e$) can be dissipated into the environment. The analogy between a single Josephson junction and a two-level atom was first proposed theoretically in the 1970's [1]. The voltage difference across the junction provides the two energy levels for the Cooper pairs, and spontaneous emission as well as stimulated emission and absorption were predicted to occur [1, 2]. Emission from Josephson junctions into low-quality cavities (either constructed artificially or intrinsic to the junction's environment) in the so-called weak-coupling regime has been studied extensively [3–8]. However, because the total output power of these systems is low, coherent radiation has not been directly demonstrated. By using a tightly confined cavity mode coherent interaction of a single Josephson junction and the cavity can be achieved. Lasing results when the transfer rate of Cooper pairs across the junction, Γ_{CP}, exceeds the cavity decay rate, κ, of the microwave photons (Fig. 5.1a)). Photon emission from alternative single emitters coupled to superconducting resonators has been the subject of several recent investigations [8–10].

We demonstrate lasing in the microwave frequency domain from a dc voltage-biased Josephson junction strongly coupled to a superconducting coplanar waveguide resonator. Our device obeys several properties present in conventional optical lasers, including injection locking, and frequency comb generation, with an injection locked linewidth

My contribution to this work included modelling and simulating the circuit.

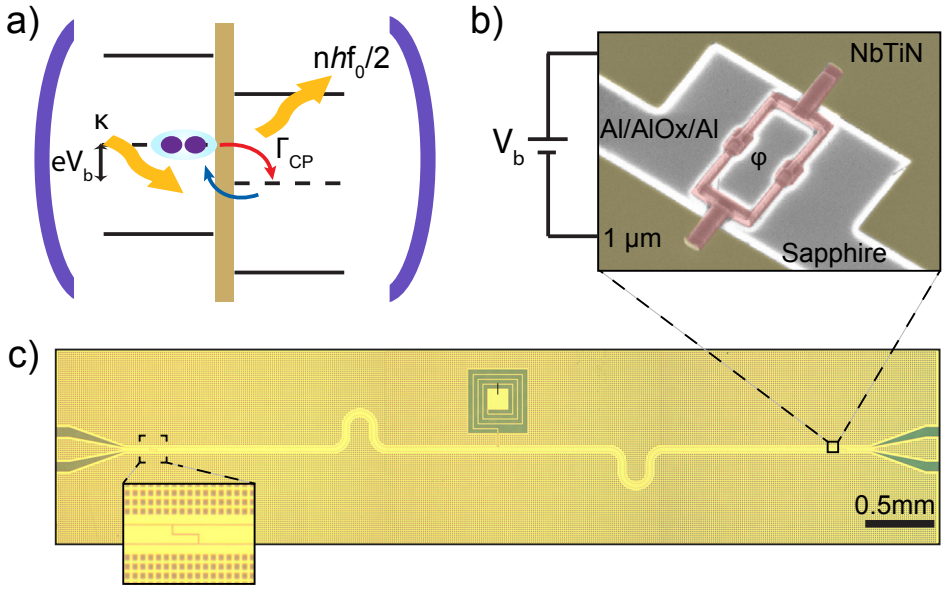

Figure 5.1: An ac Josephson laser. **a)** Illustration of the operating principle of the device. A DC voltage bias V_b applied across the Josephson junction results in photon emission into the cavity when twice the bias voltage is equal to a multiple of the cavity frequency. If the emission rate Γ_{CP} into the cavity exceed the cavity lifetime κ, these photons can be reabsorbed and reemitted by the junction, a process akin to stimulated emission in atomic laser systems. Dashed lines depict the superconducting condensate; solid lines represent the superconducting gap, Δ. **b)** Scanning electron microscope (false color) and **c)** optical microscopy images of the device. A DC SQUID (red), acting as a tunable Josephson junction, is strongly coupled to the electric field antinode of a half-wave superconducting coplanar waveguide resonator (yellow).

of $\lesssim$ 1Hz, which exceeds performance of other state of the art laser systems. The laser consists of a half-wave coplanar waveguide (CPW) resonator with resonant frequency $f_0 \approx 5.6$GHz made from thin (20nm) NbTiN (Fig. 5.1, b) and c)). A DC superconducting quantum interference device (SQUID), located at the electric field anti-node of the cavity, effectively acts as a single junction with Josephson energy tunable via the magnetic flux ϕ threading its loop: $E_J = E_{J0}|\cos(\pi\phi/\phi_0)|$, with $E_{J0} \sim 78$GHz, and $\phi_0 = h/2e$ the superconducting flux quantum. One side of the SQUID is tied to the central conductor of the CPW, with the other end attached directly to the ground plane to enhance the coupling to the cavity. An on-chip inductor positioned at the electric field node of the cavity allows for a stable DC voltage bias to be applied across the SQUID [11]. Coupling capacitors at each end of the cavity provide an input and output for microwave photons at a rate of κ_{in} and κ_{out}, respectively, as in standard circuit-QED experiments [12]. The device is mounted in a dilution refrigerator with base temperature $T = 15$mK, and the magnetic flux through the SQUID is tuned via a superconducting vector magnet.

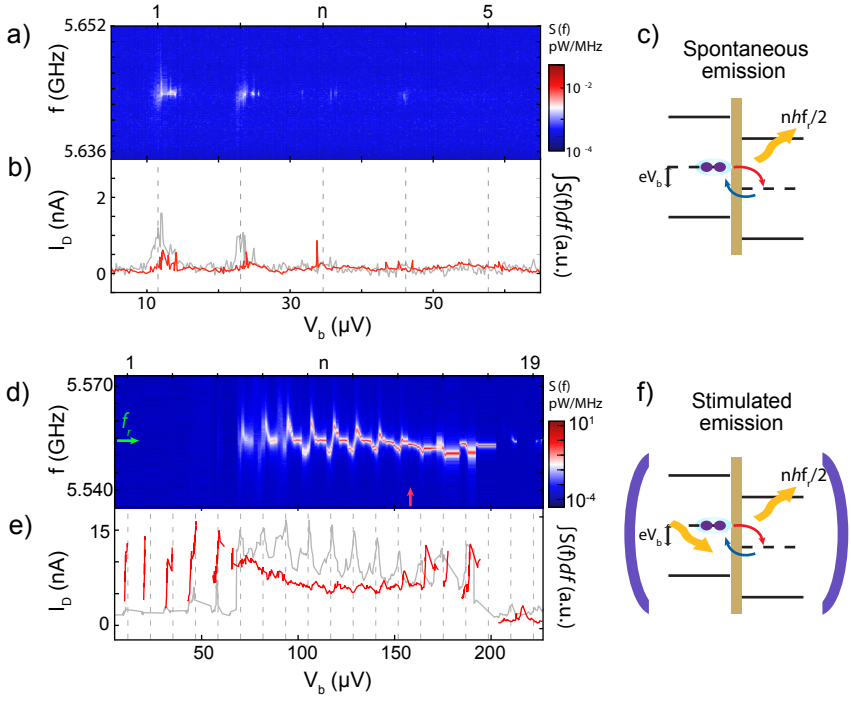

Figure 5.2: Microwave emission from the Josephson laser. **a)** Power spectrum of the emitted radiation $S(f)$, **b)** integrated emission (grey) and corresponding current flowing through the Josephson junction (red) as a function of V_b when the coupling strength $\lambda \ll 1$. **c)** Cooper pair transport can occur at discrete voltage biases corresponding to multiples of the cavity resonance frequency f_0, resulting in spontaneous photon emission into the cavity. When $\lambda > 1$, the emission **d)** and corresponding current flow **e)** become continuous across a range of bias values, peaking at bias voltages corresponding to multiples of the cavity frequency. **f)** Cooper pair transport is accompanied by the release of multiple photons into the cavity at the fundamental frequency, as well as emission of photons into the higher-order resonator modes, resulting in a cavity photon occupancy large enough for stimulated emission to occur.

DEVICE DESIGN

A 20nm NbTiN film was reactively sputtered on a cleaned 2" sapphire substrate. An SF_6/O_2 dry etch was then used to define the CPW resonator, coupling capacitors and spiral inductor. The junction sizes were ~ 180nm × 150nm, and had a total normal state resistance of $R_D = 2.4\text{k}\Omega$, with an estimated junction capacitance $C_J = 2\text{fF}$ per junction. The device is therefore in the strongly underdamped regime ($\beta_C = 2eI_cR_D^2C_J/\hbar \gg 1$).

The emission frequency of the laser is set by the resonant frequency of the bare cavity $\omega_0 = 2\pi f_0 = 1/\sqrt{LC}$, which is determined by its geometric design as well as the kinetic inductance of the thin NbTiN film ($L = L_g + L_k$). For our geometry, which consists of a 30μm wide central conductor of length $\lambda/2 = 5650\mu$m, with 1.5μm spacings to the ground plane, with $C \sim 1.4\text{pF}$ and $L_g \sim 1.2\text{nH}$ determined using elliptical integrals [13], while $L_k \sim 4.2\text{nH}$ is determined experimentally for the film from characterization resonators. Based on this we calculate a kinetic inductance fraction $\alpha = 0.78$. The total impedance $Z(\omega)$ seen by the tunneling Cooper pairs consists of the combination of the impedance of the Josephson junction and that of the parallel LC resonance with finite Q factor. As the capacitance of the resonator is much greater than the junction ($C \gg C_J$), the impedance is dominated by that of the resonator. The capacitance of each of the coupling capacitors was simulated to be 11.1fF, which results in a calculated coupling quality factor of $Q_c \sim 10^4$, giving $\kappa_{in} = \kappa_{out} = 0.27\text{MHz}$. The intrinsic quality factor of the resonator without the SQUID was much higher. Bare resonators fabricated on the same film showed $Q_i > 10^5$. However, the presence of the SQUID provides an additional damping mechanism due to the finite resistance, reducing the loaded quality factor $Q_l^{-1} = Q_c^{-1} + Q_i^{-1} + Q_r^{-1} \sim 1200$, resulting in a total cavity decay rate $\kappa = 4.7\text{MHz}$.

MICROWAVE EMISSION AND LASING

We first examine the response of the device without applying any microwave power to the cavity input. At the output, we measure the power spectral density, *S(f)*, of the emitted microwave radiation as a function of voltage bias V_b. Simultaneously, we record the corresponding current flowing through the device, $I_D = 2e\Gamma_{CP}$. The coupling between a dc voltage-biased Josephson junction and a cavity $\lambda = E_J/\phi_0^2 L$ is set by the junction's Josephson energy, E_J, together with the cavity inductance, $L = 1/C\omega_0^2$, with the cavity capacitance C and $\omega_0 = 2\pi f_0$. When the device is configured in the weak Josephson coupling regime ($\lambda \ll 1$, Fig. 5.2a)), by tuning the external flux close to $\phi = \phi_0$, a series of discrete microwave emission peaks are visible at bias voltages corresponding to n multiples of the bare cavity resonance V_r: $V_b = nV_r = nhf_0/2e \approx n \times 11.62\mu\text{V}$). At each of these emission bursts, we observe an increase in dc current (Fig. 5.2b)), a measure of inelastic Cooper pair transport across the Josephson junction. In this weak coupling regime, both the current and microwave emission are dominated by linear effects, with the rate of photon emission determined by the environmental impedance [7, 14] (Fig. 5.2c)).

We increase the microwave emission by increasing E_J via the applied flux, to the extent that the junction and cavity become strongly coupled and the system transitions to nonlinear behavior ($\lambda \gg 1$) [15]. In contrast to the discrete emission peaks seen at low Josephson energy, the emission now shifts to higher bias voltages, persisting

continuously even when the voltage bias is detuned from resonance (Fig. 5.2d)), and is accompanied by a constant flow of Cooper pairs tunneling across the junction (Fig. 5.2e)). The emission peaks at voltages corresponding to multiples of the cavity resonance, exhibiting bifurcations common to nonlinear systems under strong driving. Between these points of instability, the emission linewidth narrows to ~ 22kHz, well below the bare cavity linewidth of ~ 5MHz, corresponding to a phase coherence time $\tau_c = 1/\pi\nabla f_0 = 15\mu$s. The enhancement in emission originates from stimulated emission, as a larger photon number in the cavity increases the probability of reabsorption and coherent reemission by the junction. Notably, the emission power increases here by more than three orders of magnitude, while the average dc power input, $P_{\text{in}} = V_b I_D$, varies by only a factor of three. By comparing P_{in} with the integrated output power, we estimate a power conversion efficiency $P_{\text{out}}/P_{\text{in}} > 0.3$, several orders of magnitude greater than achieved for single junctions without coupling to a cavity [4] and comparable only to arrays containing several hundred synchronized junctions [5]. Similar power conversion efficiencies have been seen in other strongly coupled single emitter-cavity systems [8, 9]. Application of a larger perpendicular magnetic field adjusts the cavity frequency, directly tuning the laser emission frequency by more than 50MHz.

To directly confirm lasing, we measure the emission statistics in the high-Josephson coupling regime at $V_b = 192.5\mu$V. The emitted signal is mixed with an external local oscillator and the resulting quadrature components digitized with a fast acquisition card (Fig 5.3a)). A time series of the demodulated free-running laser emission over a period of 100μs (Fig. 5.3b)) shows a clear sinusoidal behavior, never entering a sub-threshold state.

This is in contrast to recently demonstrated lasers made from quantum dots [10] or superconducting charge qubits [8, 16], which are strongly affected by charge noise. Instead, we note that the coherence of our system is disrupted by occasional phase slips (Fig. 5.3, inset). To quantify the effect of these phase slips, we plot the autocorrelation $g^{(1)}$ (Fig. 5.33c)) and extract a phase coherence time of 14μs, in good agreement with the value extracted from the free running linewidth.

To confirm coherence over longer time scales, we plot the in-phase and quadrature components of the downconverted signal from 5×10^5 samples on a two-dimensional histogram (Fig. 5.3d)). The donut shape of the histogram confirms lasing, with the radius $A = \sqrt{\bar{N}} = 172$ (with the average photon number $\bar{N}$) representing the average coherent amplitude of the system, whereas the finite width $\sigma_l = \sqrt{(2\delta A^2 + N_{noise})/2} = 6.89$ is a result of amplitude fluctuations in the cavity emission $\delta A = 2.66$ broadened by the thermal noise in the amplifier chain, N_{noise}. When the device is not lasing ($V_b = 18\mu$V in Fig 5.2a)), we record a Gaussian peak of width $\sigma_{th} = \sqrt{N_{noise}/2} = 6.36$, corresponding to thermal emission (Fig 5.3e)).

To extract the photon number distribution at the output of the cavity, the contribution of thermal fluctuations due to the amplifier chain in Fig. 5.3e) is subtracted from the emission data in Fig. 5.3d). The extracted distribution takes the form $p_n \propto \exp\left[-(\mathrm{n}-\bar{\mathrm{N}})^2/(2\bar{\mathrm{N}}(1+4\delta\mathrm{A}^2))\right]$ and is centered $\bar{N} \approx 2.96 \times 10^4$, (red curve in Fig 5.3f)). In contrast, a perfectly coherent source is expected to show a shot noise limited Poissonian distribution, which tends to a Gaussian distribution of the form $p_n \propto \exp\left[-(\mathrm{n}-\bar{\mathrm{N}})^2/2\bar{\mathrm{N}}\right]$ in the limit of large $\bar{N}$ (blue curve in Fig 5.3f)). The residual fluctuations in the cavity amplitude are most probably due to E_J fluctuations which change the instantaneous photon emission

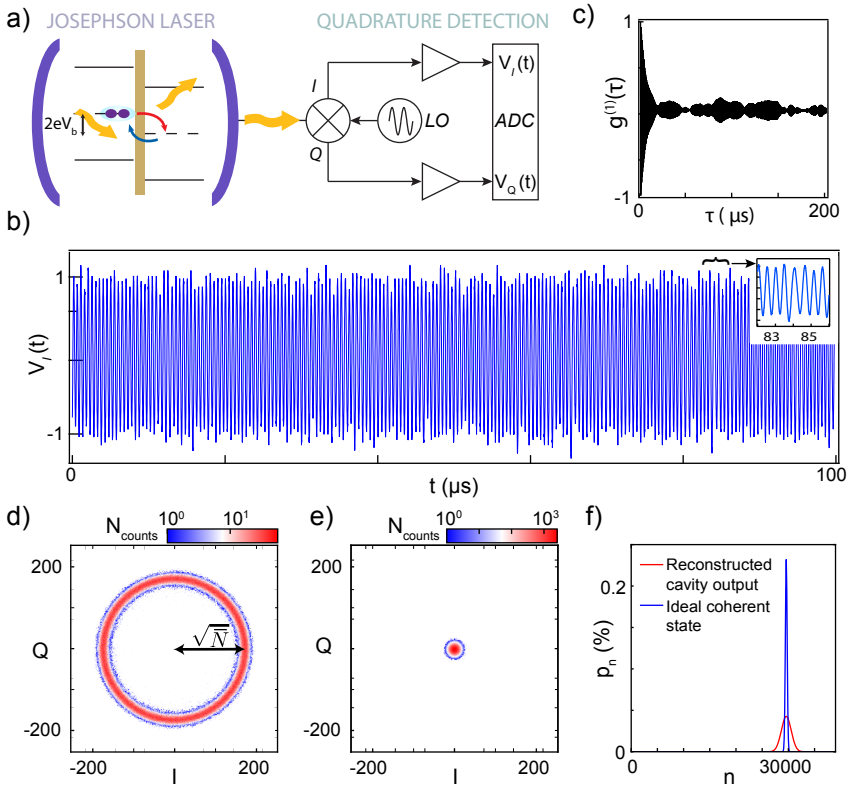

Figure 5.3: Coherence and emission statistics of the free running Josephson laser. **a)** Real-time evaluation of the emission statistics of the free-running Josephson laser is performed with a heterodyne measurement setup. **b)** Time series $V_I(t)$ of the emission over 100μs (Inset) Small phase slips in the emission result in loss of coherence, resulting in an artificially broadened emission line. **c)** Autocorrelation $g^{(1)}(\tau)$ of the time series shows a phase coherence of $\sim 14\mu$s. **d)** The IQ histogram acquired above the lasing threshold shows a clear donut shape, a characteristic of coherent emission. **e)** The IQ histogram obtained when the device is not emitting shows a Gaussian peak centered at zero, corresponding to thermal emission. **f)** The reconstructed photon number distribution p_n at the cavity output (red) is well fit by a single Gaussian peak centered around an average photon number $\bar{N} \approx 2.96 \times 10^4$, slightly broader than what expected for and ideal coherent source (blue).

rate into the cavity.

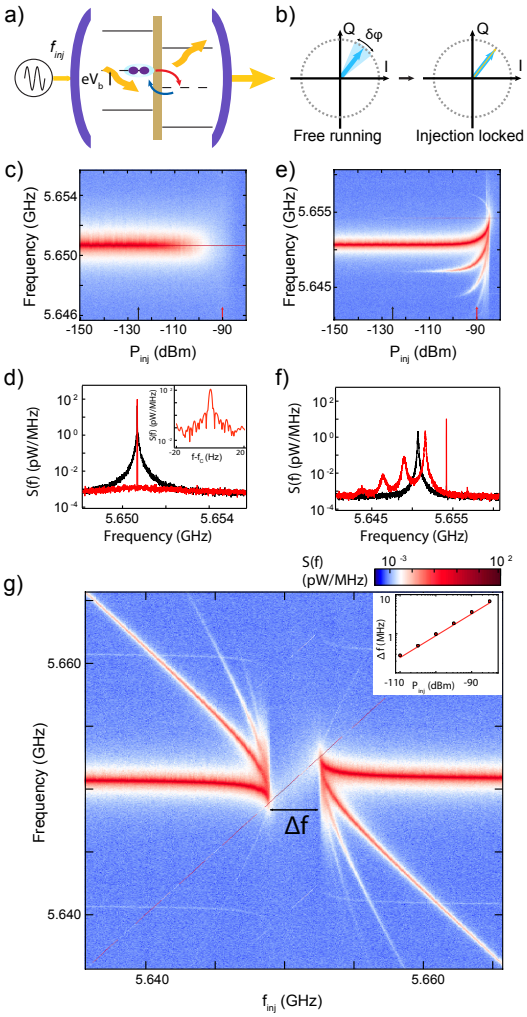

Figure 5.4: Injection locking of the Josephson laser. **a)** Schematic illustration and **b)**, phasor diagram of the injection-locking process. Injection of a low-power input tone into the cavity drives stimulated emission of photons synchronous with the input tone, reducing the phase fluctuations $\delta\phi$ experienced in the free running mode. **c)** *S(f)* as a function of input power (P_{inj}) for an on-resonance input tone. **d)** Linecuts of c) at $P_{\text{inj}} = -90$dBm (red) and -127dBm (black). (Inset) The linewidth of the injection-locked laser is $\lesssim 1$Hz **e)** *S(f)* as a function of P_{inj} for an off-resonance input tone, demonstrating frequency pulling. **f)** Linecuts of e at $P_{\text{inj}} = -90$dBm (red) and -127dBm (black). **g)** *S(f)* at fixed input power $P_{\text{inj}} = -90$dBm as the frequency of the input tone f_{inj} is swept.For probe frequencies f_{inj} in the range Δf, the laser emission frequency locks to the frequency of the input signal. (Inset) The bandwidth of frequency locking Δf scales proportionally with the square root of the input power, in agreement with the Adler theory of coupled oscillators.

LINEWIDTH AND OUTPUT POWER MEASUREMENTS

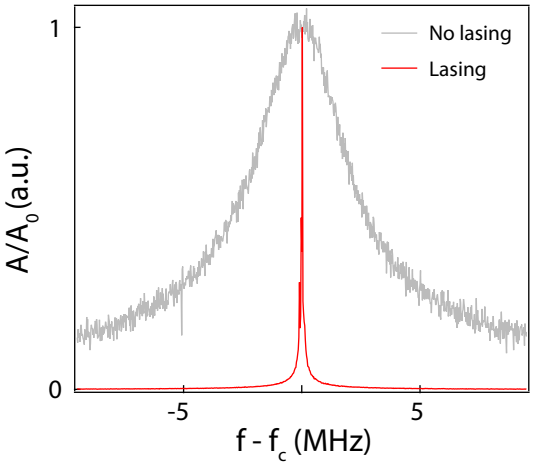

Figure 5.5: Linewidth narrowing under lasing. Normalized cavity transmission with the device lasing (red) and with the device off (grey). The device shows linewidth narrowing of more than two orders of magnitude when configured for lasing. The transmission when the laser was not lasing was measured at $V_b = 31\mu$V, between the second and third emission peaks in Fig. 5.2a), while the trace when the laser was emitting was recorded at $V_b = 162\mu V$ in Fig. 5.2c). For both measurements $P_{inj} = -140$dBm, below the single photon power in the cavity.

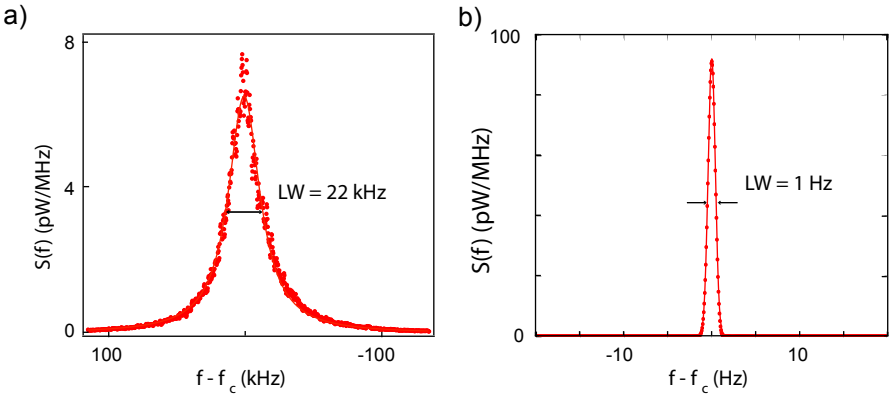

Figure 5.6: Emission linewidth of the Josephson laser. Power spectral density *S(f)* of **a)** the free running laser and **b)** the injection locked laser, measured in the large Josephson coupling regime. In free running mode, the laser is well fit by a Lorentzian function from which we extract a full-width at half maximum linewidth $\sigma = 21.4$kHz. This corresponds to a laser coherence time $\tau_{coh} = 1/(\pi\sigma) = 15\mu$s and a coherence length $l_{coh} = \tau_{coh} c = 4.45$km. When injection locked, the injection locked linewidth of the laser is ~ 1Hz, which is limited by the linewidth of the injected tone.

By integrating the emission data in Fig. 5.6a), we estimate the output power $P_{out} =$

$\int S(f)df = 0.255$pW. The DC input power to the device is calculated as $P_{in} = I_D V_b = 0.81$pW, with $I_D = 5$nA and $V_b = 162\mu$V, which gives a power conversion efficiency $P_{out}/P_{in} > 0.3$.
The quantum limited laser linewidth is predicted by the Schawlow-Townes formula [17]:

$$\sigma_{ST} = hf_0 \frac{\gamma^2}{P_{out}}, \tag{5.1}$$

with, P_{out} the power at the cavity output and γ the linewidth of the atomic transition, and is valid in the limit where $\gamma \ll \kappa$, with κ the cavity linewidth. In the case where $\kappa \leq \gamma$, as is common for many semiconductor-based laser systems, this expression is modified by replacing γ with an effective linewidth $l_{ST}^{-1} = \gamma^{-1} + \kappa^{-1}$, which tends to $l_{ST} = \kappa$ for $\kappa \ll \gamma$ [18]. In our case, the atomic transition is the voltage bias on the Josephson junction V_b, and its linewidth is set by the residual voltage noise, which is of order 30 kHz, much less than κ. Using the output power calculated from by integrating the emission data in Fig. 5.6a), we calculate the Schawlow-Townes linewidth to be ~ 14mHz.

FLUX TUNING OF THE JOSEPHSON COUPLING AND EMISSION FREQUENCY

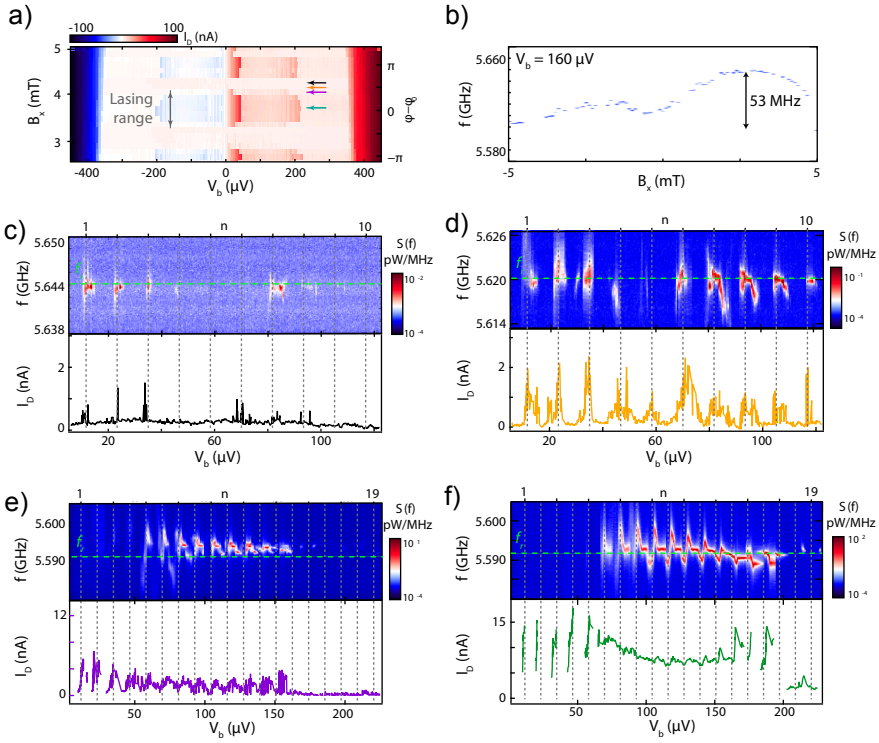

Figure 5.7: Flux tuning of the Josephson coupling and emission frequency. **a)** The Josephson coupling strength is tuned by the application of a perpendicular magnetic field through the SQUID loop. The supercurrent and subgap emission features show a characteristic SQUID oscillation with periodicity ~ 1 mT, which is in good agreement for a SQUID of area ~ $1.5\mu m^2$. The arrows show the approximate values for the magnetic flux tuning for the data shown in (c – f). **b)** Application of a larger perpendicular magnetic field shifts the resonant frequency of the cavity, tuning the laser emission over a frequency range of more than 50MHz. Shown is the power spectral density *S(f)* as a function of perpendicular magnetic field B_x at fixed voltage bias $V_b = 160\mu V$. In a) and b), the applied external magnetic field has a small offset from the true magnetic field due to hysteresis in the superconducting magnet and residual magnetic fields in the setup. **c) – f)** Power spectral density *S(f)* of the emission for increasing Josephson couplings corresponding to the location of arrows in a). By tuning the applied magnetic flux, the device evolves from weak coupling between the SQUID and the cavity to being strongly coupling, where significant line narrowing takes place. The current spikes present at low bias voltages in f) occur due to instabilities in the load circuit at low bias, and correspond to retrapping to the zero-voltage state, as is common for many measurements of voltage biased Josephson junctions. As these points are analogous to the case of a zero bias supercurrent flow, they are not accompanied by photon emission.

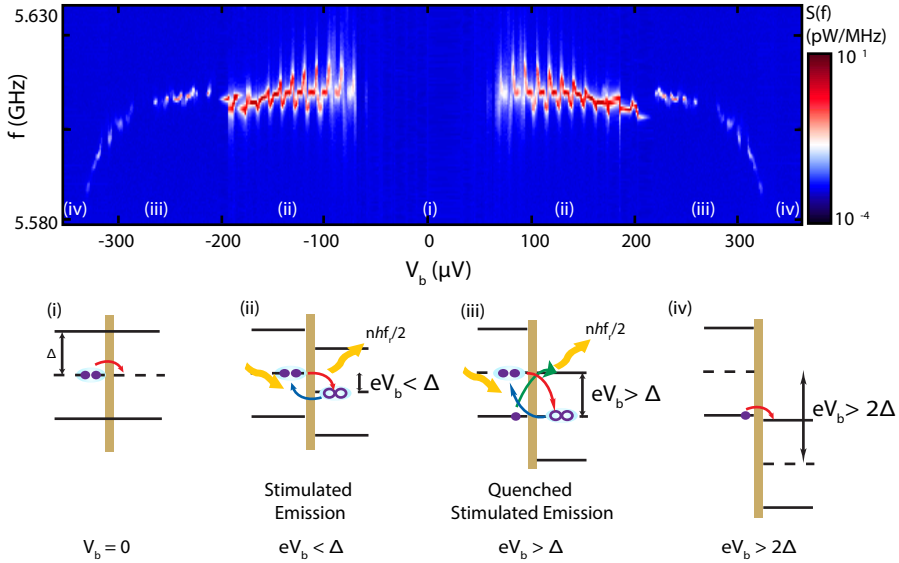

Figure 5.8: Operating regimes of the Josephson laser. Power spectral density $S(f)$ over a wider range of applied voltage bias at large Josephson coupling. (i) Dissipationless supercurrent. At $V_b = 0$, Cooper pairs can directly tunnel across the junction without additional energy being dissipated. (ii) Stimulated emission. At a large Josephson coupling and a voltage bias equal to a multiple of the cavity resonance, many photons are released into the cavity. The cavity photon population is large enough that the junction can reabsorb and re-emit some of these photons. (iii) Quenched stimulated emission. When the voltage bias exceeds the superconducting gap $eV_b > \Delta$, absorption of cavity photons can also allow quasiparticles to tunnel across the junction, damping the junction and quenching the emission (iv) Resistive transport. When the voltage bias exceeds twice the superconducting gap $eV_b > 2\Delta$, direct quasiparticle transport can take place without any accompanying photon emission.

TEMPERATURE DEPENDENCE OF LASING

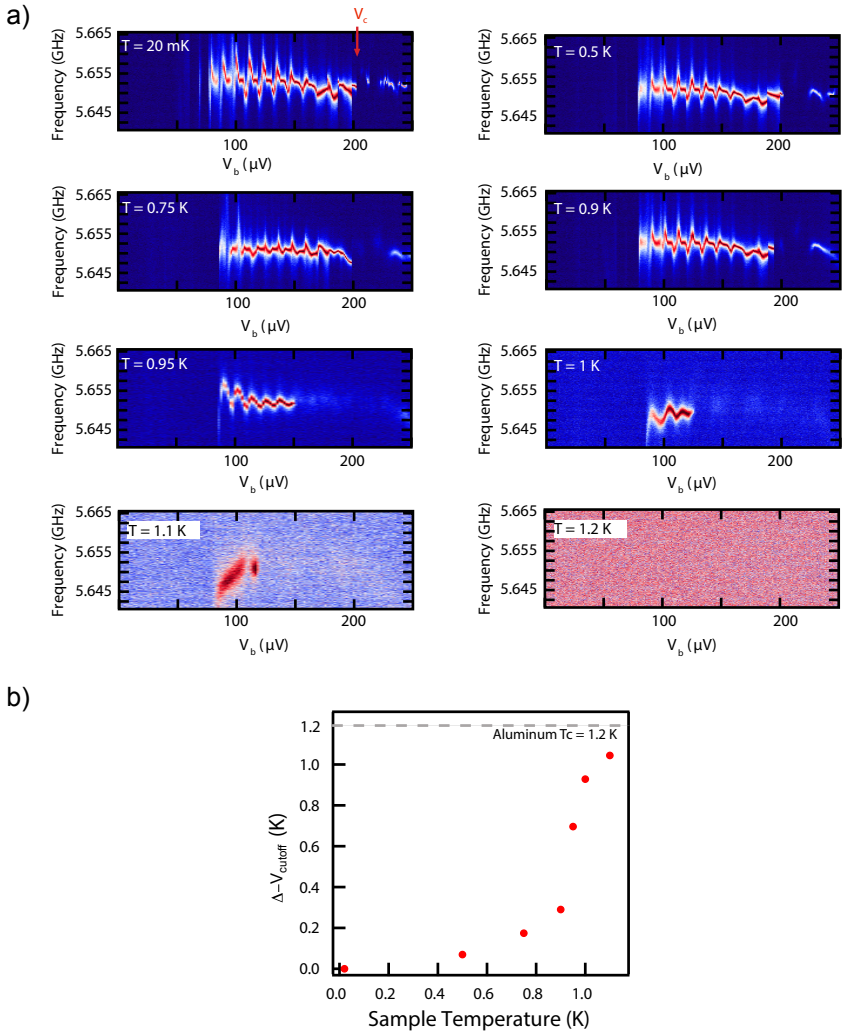

Figure 5.9: Temperature dependence of the emission. **a)** Power spectral density *S(f)* of the emission as a function of voltage bias for different sample temperatures. **b)** The emission cutoff point V_c scales strongly with temperature close to the superconducting critical temperature of Aluminium, indicating that the upper cutoff of the emission V_c is set by excitation of quasiparticles that damp the junction.

INJECTION LOCKING

Emission linewidth is a key figure of merit for lasers. A narrow linewidth implies high frequency stability and resolution, which is important for a range of technologies including spectroscopy, imaging and sensing application. One technique commonly used for stabilizing lasers is injection locking [19, 20] (Fig. 5.4, a) and b)). The injection of a seed tone of frequency f_{inj} into the cavity generates stimulated emission in the Josephson junction at this injected frequency, narrowing the emission spectrum. Figure 5.4c) shows *S(f)* as a function of input power P_{inj} for an injected signal with frequency $f_{\text{inj}} = 5.651$GHz, well within the emission bandwidth of the free running source [linecuts at $P_{\text{inj}} = -127$dBm and $P_{\text{inj}} = -90$dBm (Fig. 5.4d)]. For very low input power, $P_{\text{inj}} < -140$dBm, the average photon occupation of the cavity is $\bar{N} < 1$, and the device remains unaffected by the input tone. Once the photon occupancy exceeds $\bar{N} \approx 1$, the injected microwave photons drive stimulated emission in the device, causing the emission linewidth to narrow with increasing power, reaching an ultimate (measurement-limited) linewidth of 1Hz (Fig. 5.4d), inset), which is more than three orders of magnitude narrower than the free-running emission peak and approaches the Schawlow-Tones limit of $\sim$ 15 mHz. In this regime, our device acts as a quantum limited amplifier, similar to other Josephson junction based amplifiers [21, 22]; however, no additional microwave pump tone is required to provide amplification. Figure 5.4e) shows the effect when the input tone is applied at a frequency $f_{\text{inj}} = 5.655$GHz, outside the cavity bandwidth. At low input powers the emission remains unaffected, similar to the on-resonant case shown earlier. When $P_{\text{inj}} > -130$dBm, distortion side-bands appear at both positive and negative frequencies, and the free running emission peak is pulled towards the input tone, eventually being locked when $P_{\text{inj}} > -85$dBm [linecuts at $P_{\text{inj}} = -127$dBm and $P_{\text{inj}} = -90$dBm (Fig 5.4f)]. The positions and intensities of these emission sidebands are well described by the Adler theory for the synchronization of coupled oscillators [23], similar to what has been observed for both traditional and exotic laser systems [19, 20].

The frequency range over which the device can be injection locked is strongly dependent on the injected power. Figure 5.4g) shows the *S(f)* as a function of f_{inj} at an input power $P_{\text{inj}} = -90$dBm, with an injection locking range Δf of almost 5MHz. Here, the distortion sidebands span more than 100MHz. Measurements of Δf as a function of P_{inj} are shown in the inset of Fig. 5.4g). Adler's theory predicts that the injection locking range should fit a square-root relation $\Delta f = \alpha\sqrt{P_{\text{inj}}}$, with a measured prefactor $\alpha = 3.66 \pm 1.93\text{MHz}/\sqrt{\text{W}}$.

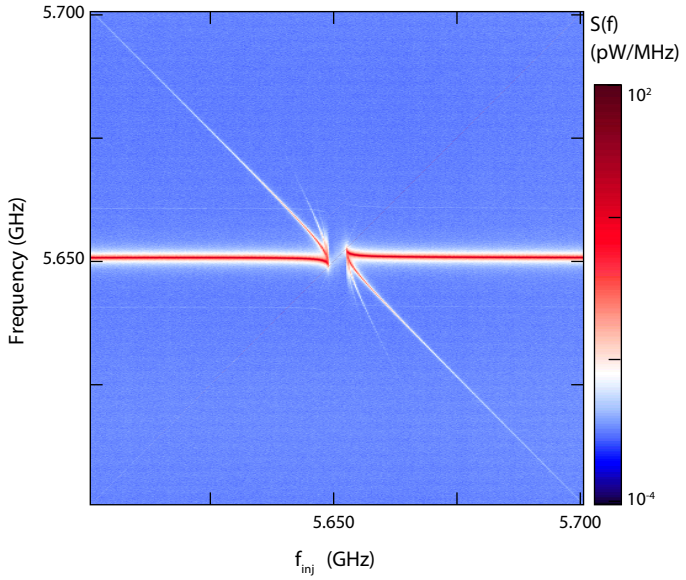

Figure 5.10: Injection locking - Sideband range. Power spectral density *S(f)* as a function of frequency of the injected tone for an input power $P_{inj} = -90$dBm showing creation of sidebands spanning more than 100MHz.

COMPARISON TO THEORY

We compare our injection locking data in Fig. 5.4 to the predictions of the Adler theory for coupled oscillators [23]. Following from [20, 24], for a given input power P_{inj}, the frequency range Δf over which the input signal can be locked is given by

$$\Delta f = C_\kappa \kappa_t \sqrt{P_{inj}/P_{out}} = \alpha \sqrt{P_{inj}}. \tag{5.2}$$

Here the prefactor $C_\kappa = 2\sqrt{\kappa_{in}\kappa_{out}}/\kappa = 0.11$ accounts for internal cavity losses. This gives $\alpha = 1.07\text{MHz}/\sqrt{\text{W}}$, which is in reasonable agreement with the experimentally determined value of $\alpha = (3.66 \pm 1.93)\text{MHz}/\sqrt{\text{W}}$, as extracted from the fit to the data in Fig. 5.4. Outside the region of injection locking, the injection of an off-resonant tone at frequency f_{inj} results in generation of higher harmonics to the bare emission at frequency $f_0 = 5.65067$GHz. As the frequency of the injected signal approaches that of the bare emission, both the emitted signal and higher harmonics are pulled towards the injected tone until they are locked across the frequency range Δf. The positions of the pulled emission signal and the nth harmonics are given by

$$f_n = f_{inj} + (n+1) f_h, \tag{5.3}$$

with

$$f_h = (f_0 - f_{inj}) \sqrt{1 - \left(\frac{\Delta f/2}{f_0 - f_{inj}} \right)}. \tag{5.4}$$

Figure 5.11a) shows the calculated positions of the pulled emission signal f_e (n = 0) and higher harmonics located at n=-2,1,2,3,4 overlaying the raw data for an input power P =

f_{in} (GHz)	5.6447		5.6481		5.6619	
	Calc.	Exp.	Calc.	Exp.	Calc.	Exp
f_e (GHz)	5.650	5.650	5.650	5.650	5.651	5.651
f_1 (GHz)	5.656	5.656	5.651	5.652	5.640	5.640
f_2 (GHz)	5.662	5.662	5.653	5.654	5.629	-
f_3 (GHz)	5.667	-	5.654	5.656	5.618	-
f_4 (GHz)	5.673	-	5.656	5.658	5.607	-
f_{-2} (GHz)	5.639	-	5.647	5.646	5.673	-
P_1/P_0	2.9×10^{-2}	1.1×10^{-2}	2.2×10^{-1}	1.2×10^{-1}	8.1×10^{-3}	3.5×10^{-3}
P_2/P_0	8.8×10^{-4}	3.2×10^{-4}	4.8×10^{-2}	1.0×10^{-2}	6.5×10^{-5}	-
P_3/P_0	2.6×10^{-5}	-	1.0×10^{-2}	1.6×10^{-3}	5.2×10^{-7}	-
P_4/P_0	7.7×10^{-7}	-	2.3×10^{-3}	9.3×10^{-4}	4.2×10^{-9}	-
P_{-2}/P_0	7.7×10^{-7}	-	2.3×10^{-3}	9.3×10^{-4}	4.2×10^{-9}	-

Table 5.1: Calculated and experimentally determined peak positions and relative intensities of sideband harmonics under injection locking.

−90dBm, which results in an injection locking frequency range of $\Delta f \approx 5$MHz. As seen from Eq. 5.3, the harmonic at $n = -1$ overlaps with the injected input tone, and so is not observed.
Adler's equation also predicts the relative powers of the sidebands when compared to the free emission power:

$$P_n/P_0 = |a_n/a_0|^2 = \left(\frac{(-f_0 + f_{inj} + f_h) + i\Delta f/2}{(f_0 - f_{inj} + f_h) - i\Delta f/2}\right)^{2n}. \tag{5.5}$$

Linecuts of the injection locking data in Fig. 5.11a) are shown in Fig. 5.11b)-d). Fits to the experimental data are shown as black solid lines. Each emission peak is fit with a Lorentzian lineshape, with the input frequency fit with a Gaussian of width $\sigma = 10$kHz. Table 5.1 shows a comparison of the experimental and calculated harmonic frequencies f_n for each of the sidebands and the pulled emission, together with their relative emission power P_n/P_0 from solving Eq. 5.5. Frequencies are extracted by fitting the raw data with a multi-peaked Lorentzian function.

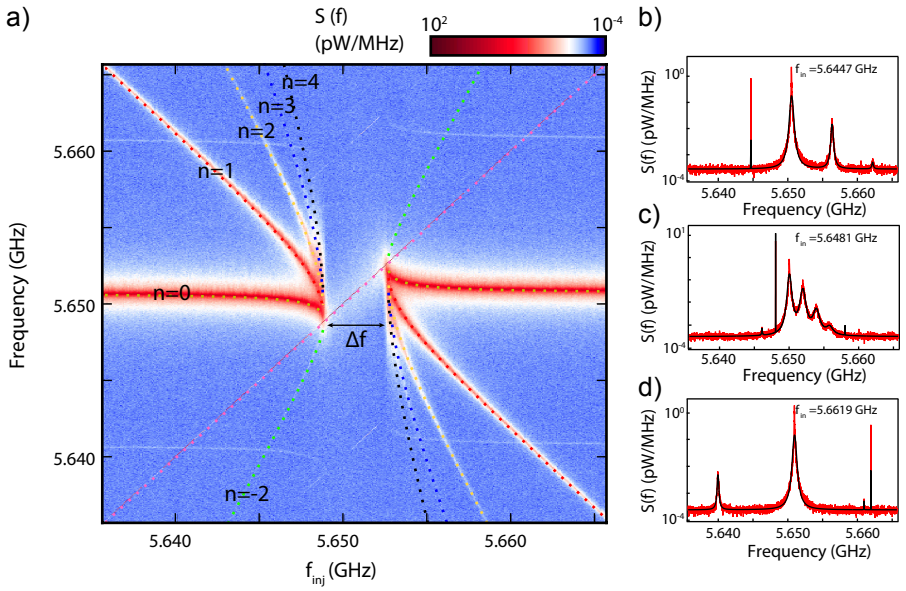

Figure 5.11: Injection locking - Comparison to theory. **a)** Power spectral density *S(f)* as a function of frequency of the injected tone for an input power $P_{inj} = -90$dBm. The emission is injection locked for a frequency range $\Delta f \approx 5$MHz. Overlaying the data are the calculated positions of the pulled emission f_e and sidebands $f_{-2,1,2,3,4}$. Faint modulation sidebands can be seen at $f_e \pm 10$MHz due to noise on the input line to the cavity. **b) – d)** Linecuts of a) corresponding to **b)** $f_{inj} = 5.6447$GHz, **c)** $f_{inj} = 5.6481$GHz and **d)** $f_{inj} = 5.6619$GHz. The solid lines are fits to S(f).

FREQUENCY COMB GENERATION

Optical frequency combs have generated significant interest in recent years [25], making it possible to extend the accuracy of the atomic clocks from the radio to the optical frequency region, leading to breakthroughs in optical metrology, high precision spectroscopy and telecommunication technologies. Recently, microwave frequency combs have also been generated using four-wave mixing in superconducting resonators [26]. Here we demonstrate a similar frequency comb by applying a voltage modulation to the Josephson junction (Fig. 5.12a), as recently described theoretically in [27]. As an example, we configure the device in the on-resonance injection locked regime ($P_{inj} = -110$dBm in Fig. 5.4c) and apply a small ac excitation of frequency $f_{\mathrm{mod}} = 111$Hz to the DC bias. This generates a comb around the central pump tone with frequency separation 111Hz, as seen in Fig. 5.12b). The total width of the comb is set by the amplitude of the modulation (Inset, 5.12b), as well as the input power of the injection lock signal.

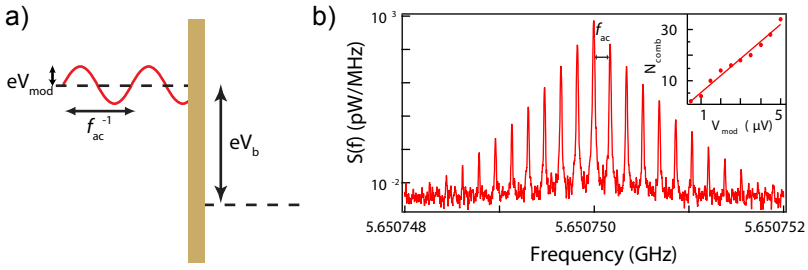

Figure 5.12: Frequency comb generation. **a) – b)** Low frequency ($f_{\mathrm{ac}} = 111$Hz) modulation of the voltage bias across the SQUID under injection locking conditions generates a frequency comb of phase coherent signals spaced f_{ac} in frequency around the center emission frequency. (Inset) The comb width, N_{comb}, is controlled by V_{mod}, the amplitude of the modulation on the voltage bias.

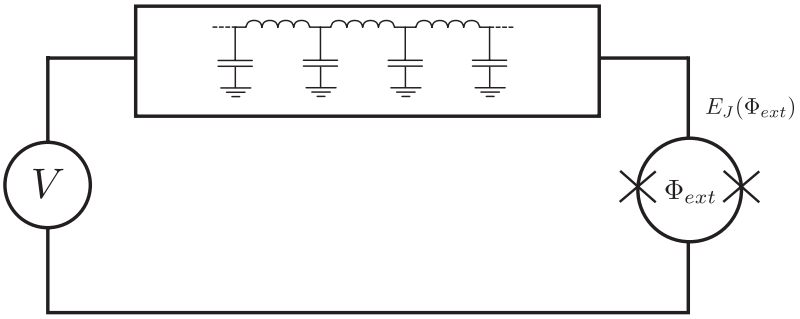

Figure 5.13: Circuit schematic. Circuit diagram of a voltage-biased Josephson junction in series with a resonator. The Josephson energy of the junction $E_J(\Phi_{ext})$ can be tuned by an external magnetic flux Φ_{ext}.

NUMERICAL MODEL

To understand the strong emission characteristics, we numerically simulate the time evolution of the coupled resonator-Josephson junction circuit for increasing E_J. We model the circuit as an LC resonator in series with a dc-SQUID with an applied voltage bias shown in Fig. 5.13. We begin our analysis with the single mode resonator approximation as studied in Ref.'s [15, 28, 29], with the equations of motion

$$C\ddot{\varphi} = L^{-1}\varphi - \gamma\dot{\varphi} + \phi_0^{-2}E_J \sin\left(2\pi f_J t + \varphi\right), \tag{5.6}$$

with f_J the Josephson frequency, φ the resonator phase variable, C and L the capacitance and inductance of the main resonator harmonic [$f_0 = 1/(2\pi\sqrt{LC})$], and γ the dissipation rate. The drive term is proportional to E_J and it is characterized by a dimensionless coupling strength $\lambda = E_J/\phi_0^2 C\omega_0^2$. Solving the time evolution numerically, we find that a strongly detuned drive $V_b/V_r = n \gg 1$ cannot produce a response that is only weakly dependent on f even for $\lambda \gtrsim 1$, contrary to the experimental observations (see left panels in Fig. 5.14).

Going beyond the approximation of Ref. [15] we find that a necessary extension of the model allowing for efficient down-conversion from large n is the effect of the higher resonator modes leading us to:

$$C\ddot{\varphi}_i = i^2 L^{-1}\varphi_i - \gamma\dot{\varphi}_i + \phi_0^{-2}E_J\alpha_i \sin\left(2\pi f_J t + \sum_{i=1}^{M}\alpha_i\varphi_i\right), \tag{5.7}$$

with φ_i the phase variables of M resonator harmonics. Due to the strong nonlinearity of the equations of motion at small γ and large E_J, including the higher harmonics modes is a necessary extension of Eq. (5.6). We also verify that including Kerr nonlinearity or including the load circuit in the single mode dynamics (5.6) are not alone sufficient to reproduce the lasing behavior. The variation of the coupling strengths α_i of different modes to the Josephson junction is geometry-dependent, however we verify that the specific ratios of α_i do not influence our conclusions. For simplicity we present the results for $\alpha_i = 1$. A precise simulation of the coupling to the transmission line is beyond

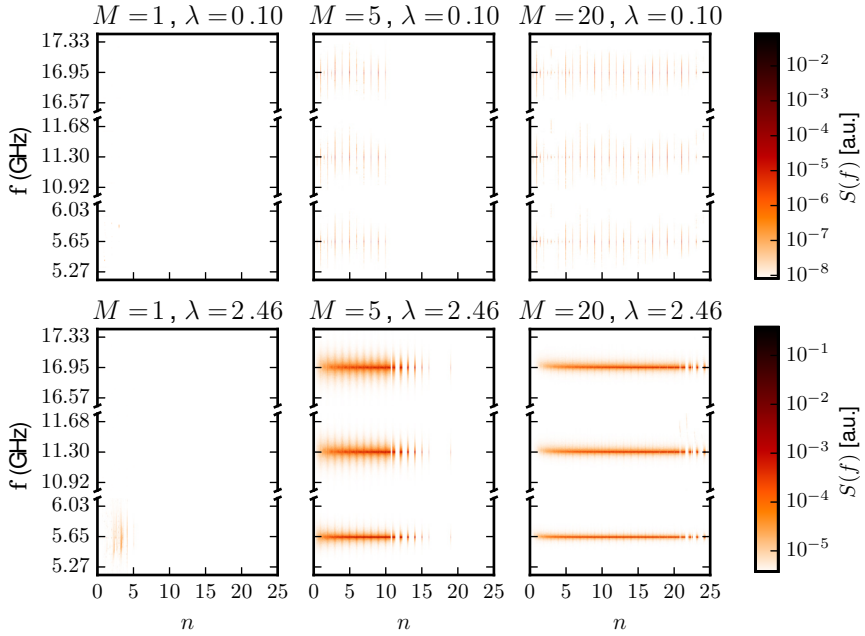

Figure 5.14: Dependence of the numerical emission spectra for different coupling strength and numbers of modes of the lowest three resonator modes.

the scope of Eq. 5.7. In order to estimate the emitted power we therefore assume that all of the dissipation happens due to emission into the transmission line. This is supported by comparing the intrinsic resonator quality factor $Q \approx 10^5$ with the quality factor of the resonator coupled to the transmission line $Q \approx 2 \cdot 10^4$. This allows us to estimate the emitted power spectrum using $S(f) = \gamma f^2 \varphi_f^2$, with φ_f the Fourier component of φ at frequency f. Our numerical results are summarized in Fig. 5.14. The mode mixing results in approximate equipartition of emission power between the different resonator modes, and the number of available resonator modes determines the higher cutoff for the efficient down-conversion of f_J into the main harmonic of the resonator. A low E_J produces a series of disconnected peaks, as shown in the top panels of Fig. 5.14.

Studying the response of the lowest resonator harmonic more closely (see Fig. 5.15), we observe several features similar to the experimental observations. Specifically, the linewidth exhibits periodic modulation, becoming broader on resonance. The emission amplitude is continuous until a certain upper threshold, above which it separates into disconnected intervals.

Finally, we relax the assumption of equal mode spacing, unexpected in a realistic line resonator. To study the effect of incommensurate mode frequencies, we consider the detuning of mode frequencies by a small random amount: $\omega_i = (i + r_i)\omega_0$ for $i > 1$. We choose detuning r_i to be a uniformly distributed random variable in the interval

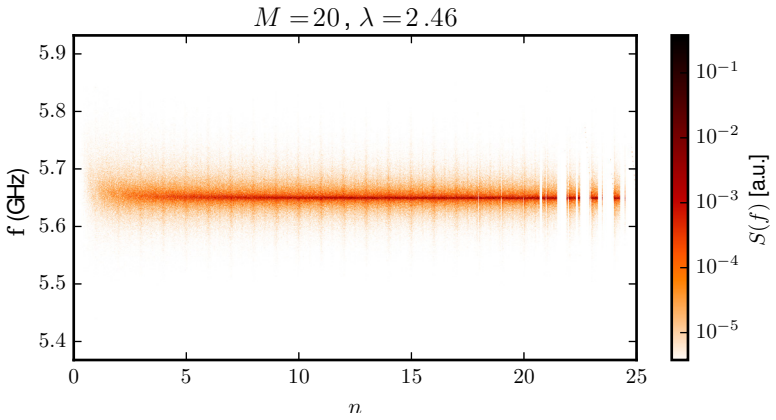

Figure 5.15: The emission spectrum of the lowest resonator mode for large coupling and in presence of multiple resonator modes.

5

$[-0.1, 0.1]$ or $[-0.3, 0.3]$. Our results are shown in Fig. 5.16. We observe that the detuning of the higher harmonics does not change the overall spectral shape of the emitted signal, except for washing out the resonant peaks corresponding to the frequencies of the higher modes.

DISCUSSION

We can also use the device to generate a microwave frequency comb, an alternative to recently demonstrated four-wave-mixing methods [26] The time-frequency duality implies that a voltage modulation applied to the junction will create a comb in the frequency domain [27]. By configuring the device in the on-resonance injection-locked regime ($P_{inj} = -110$dBm in Fig. 5.4c) and applying a small ac excitation frequency $f_{\text{mod}} = 111$Hz to the dc bias, we generate a comb around the central pump tone, with frequency separation 111Hz. The total width of the comb is set by the amplitude of the modulation, as well as the input power of the injection lock.

Our results conclusively demonstrate lasing from a dc-biased Josephson junction in the strong coupling regime. Analysis of the output emission statistics shows 15μs of phase coherence, with no sub-threshold behavior. The Josephson junction laser does not suffer from charge-noise-induced linewidth broadening inherent to semiconductor gain media [10, 30], and thus reaches an injection locked linewidth of < 1Hz. The device produces frequency tunability over 50MHz via direct tuning of the cavity frequency and over 100MHz through the generation of injection-locking sidebands. Additional frequency control may be achieved by using a broadband tunable resonator [31], and pulse control may be provided with a tunable coupler. The phase coherence is likely limited by fluctuations in E_J, either due to $1/f$-dependent flux noise from magnetic impurities [32], or due to defects within the Josephson junction, as well as thermal fluctuations in the biasing circuit that vary V_b. We anticipate that improvements to the magnetic shielding and passivating magnetic fluctuators, together with using a cryogenically generated voltage bias

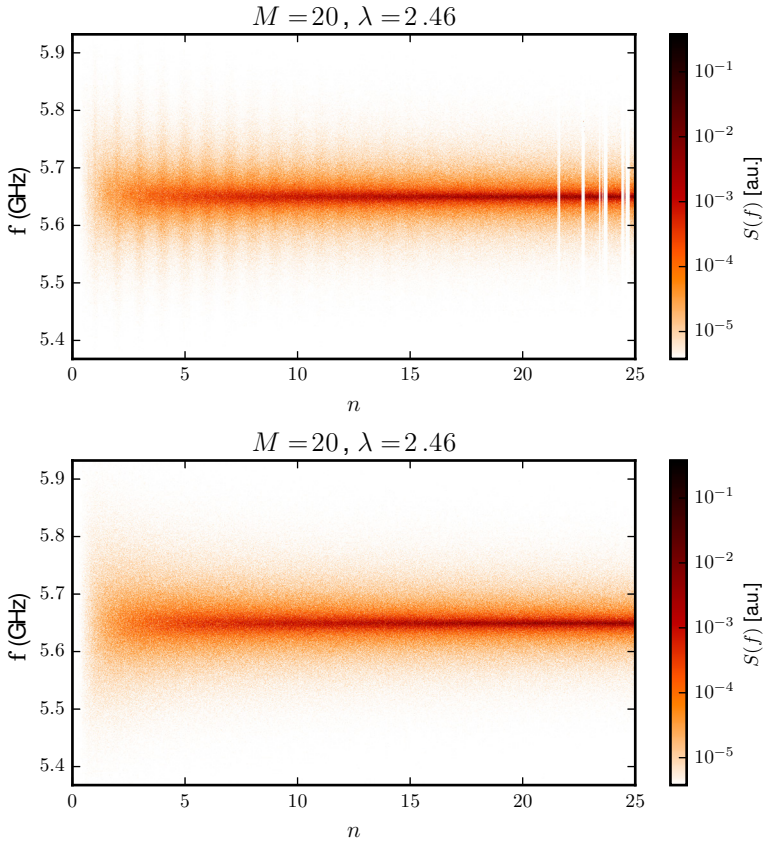

Figure 5.16: Emission spectrum of the lowest mode with **a)** 10% detuning, or **b)** 30% detuning

will further stabilize the emission. In this case the device would perform at the quantum limit, with a linewidth that would then only be limited by residual fluctuations in the photon number in the cavity. Along with the high efficiency, the possibility of engineering the electromagnetic environment and guiding the emitted microwaves on demand lends this system to a versatile cryogenic source for propagating microwave radiation.

REFERENCES

[1] D. R. Tilley, *Superradiance in arrays of superconducting weak links,* Physics Letters A **33**, 205 (1970).

[2] D. Rogovin and M. Scully, *Superconductivity and macroscopic quantum phenomena,* Physics Reports **25**, 175 (1976).

[3] N. F. Pedersen, O. H. Soerensen, J. Mygind, P. E. Lindelof, M. T. Levinsen, and T. D. Clark, *Direct detection of the Josephson radiation emitted from superconducting thinfilm microbridges,* Applied Physics Letters **28**, 562 (1976).

[4] C. Varmazis, J. E. Lukens, and T. F. Finnegan, *Broadband generation of tunable Josephson radiation at microwave frequencies,* Applied Physics Letters **30**, 660 (1977).

[5] P. Barbara, A. B. Cawthorne, S. V. Shitov, and C. J. Lobb, *Stimulated emission and amplification in Josephson junction arrays,* Physical Review Letters **82**, 1963 (1999).

[6] L. Ozyuzer, A. E. Koshelev, C. Kurter, N. Gopalsami, Q. Li, M. Tachiki, K. Kadowaki, T. Yamamoto, H. Minami, H. Yamaguchi, T. Tachiki, K. E. Gray, W.-K. Kwok, and U. Welp, *Emission of coherent THz radiation from superconductors,* Science **318**, 1291 (2007).

[7] M. Hofheinz, F. Portier, Q. Baudouin, P. Joyez, D. Vion, P. Bertet, P. Roche, and D. Esteve, *Bright side of the Coulomb blockade,* Physical Review Letters **106**, 217005 (2011).

[8] F. Chen, J. Li, A. D. Armour, E. Brahimi, J. Stettenheim, A. J. Sirois, R. W. Simmonds, M. P. Blencowe, and A. J. Rimberg, *Realization of a single-Cooper-pair Josephson laser,* Physical Review B **90**, 20506 (2014).

[9] O. Astafiev, K. Inomata, A. O. Niskanen, T. Yamamoto, Y. A. Pashkin, Y. Nakamura, and J. S. Tsai, *Single artificial-atom lasing,* Nature **449**, 588 (2007), arXiv:0710.0936 .

[10] Y.-Y. Liu, J. Stehlik, C. Eichler, M. J. Gullans, J. M. Taylor, and J. R. Petta, *Semiconductor double quantum dot micromaser,* Science **347**, 285 (2015).

[11] F. Chen, A. J. Sirois, R. W. Simmonds, and A. J. Rimberg, *Introduction of a dc bias into a high-q superconducting microwave cavity,* Applied Physics Letters **98**, 132509 (2011), http://aip.scitation.org/doi/pdf/10.1063/1.3573824 .

[12] A. Wallraff, D. I. Schuster, A. Blais, L. Frunzio, R.-S. Huang, J. Majer, S. Kumar, S. M. Girvin, and R. J. Schoelkopf, *Strong coupling of a single photon to a superconducting qubit using circuit quantum electrodynamics,* Nature **431**, 162 (2004).

[13] R. N. Simons, *Coplanar waveguide circuits, components, and systems*, Wiley Series in Microwave and Optical Engineering (Wiley, 2004).

[14] M. H. Devoret, D. Esteve, H. Grabert, G.-L. Ingold, H. Pothier, and C. Urbina, *Effect of the electromagnetic environment on the Coulomb blockade in ultrasmall tunnel junctions,* Physical Review Letters **64**, 1824 (1990).

[15] S. Meister, M. Mecklenburg, V. Gramich, J. T. Stockburger, J. Ankerhold, and B. Kubala, *Resonators coupled to voltage-biased Josephson junctions: From linear response to strongly driven nonlinear oscillations,* Physical Review B **92**, 174532 (2015).

[16] O. Astafiev, K. Inomata, A. O. Niskanen, T. Yamamoto, Y. A. Pashkin, Y. Nakamura, and J. S. Tsai, *Single artificial-atom lasing,* Nature **449**, 588 (2007).

[17] A. L. Schawlow and C. H. Townes, *Infrared and optical masers,* Physical Review **112**, 1940 (1958).

[18] H. Wiseman, *Light amplification without stimulated emission: Beyond the standard quantum limit to the laser linewidth,* Physical Review A **60**, 4083 (1999).

[19] H. L. Stover, *Locking of laser oscillators by light injection,* Applied Physics Letters **8**, 91 (1966).

[20] Y.-Y. Liu, J. Stehlik, M. J. Gullans, J. M. Taylor, and J. R. Petta, *Injection locking of a semiconductor double-quantum-dot micromaser,* Physical Review A **92**, 053802 (2015).

[21] B. Yurke, P. G. Kaminsky, R. E. Miller, E. A. Whittaker, A. D. Smith, A. H. Silver, and R. W. Simon, *Observation of 4.2-K equilibrium-noise squeezing via a Josephson-parametric amplifier,* Physical Review Letters **60**, 764 (1988).

[22] I. Siddiqi, R. Vijay, F. Pierre, C. M. Wilson, M. Metcalfe, C. Rigetti, L. Frunzio, and M. H. Devoret, *RF-driven Josephson bifurcation amplifier for quantum measurement,* Physical Review Letters **93**, 207002 (2004).

[23] R. Adler, *A Study of locking phenomena in oscillators,* Proceedings of the IRE **34**, 351 (1946).

[24] M. Armand, *On the output spectrum of unlocked driven oscillators,* Proceedings of the IEEE **57**, 798 (1969).

[25] S. T. Cundiff and J. Ye, *Colloquium: Femtosecond optical frequency combs,* Reviews of Modern Physics **75**, 325 (2003).

[26] R. P. Erickson, M. R. Vissers, M. Sandberg, S. R. Jefferts, and D. P. Pappas, *Frequency comb generation in superconducting resonators,* Physical Review Letters **113**, 187002 (2014).

[27] P. Solinas, S. Gasparinetti, D. Golubev, and F. Giazotto, *A Josephson radiation comb generator,* Scientific Reports **1**, 12260 (2015).

[28] V. Gramich, B. Kubala, S. Rohrer, and J. Ankerhold, *From Coulomb-blockade to nonlinear quantum dynamics in a superconducting circuit with a resonator,* Physical Review Letters **111**, 247002 (2013).

[29] A. D. Armour, M. P. Blencowe, E. Brahimi, and A. J. Rimberg, *Universal quantum fluctuations of a cavity mode driven by a Josephson junction,* Physical Review Letters **111**, 1 (2013), arXiv:1307.2498 .

[30] J. Faist, F. Capasso, D. L. Sivco, C. Sirtori, A. L. Hutchinson, and A. Y. Cho, *Quantum cascade laser,* Science **264**, 553 (1994).

[31] Z. L. Wang, Y. P. Zhong, L. J. He, H. Wang, J. M. Martinis, A. N. Cleland, and Q. W. Xie, *Quantum state characterization of a fast tunable superconducting resonator,* Applied Physics Letters **102**, 163503 (2013).

[32] F. C. Wellstood, C. Urbina, and J. Clarke, *Low frequency noise in dc superconducting quantum interference devices below 1 K,* Applied Physics Letters **50**, 772 (1987).

CURRICULUM VITÆ

Sebastian RUBBERT

03-02-1989	Born in Engelskirchen, Germany.

EDUCATION

2008	Abitur Gymnasium Moltkestraße, Gummersbach Germany (1999–2005, 2006–2008) Basha Highschool, Chandler USA (2005–2006)	
2008–2009	Civil service in a retirement home Wohnstift Aureliusstraße, Aachen Germany	
2009–2013	Bsc. and Msc. in Physics Rheinisch-Westfälische Technische Hochschule Aachen, Germany	
	Bsc. Thesis:	Performance of feedback schemes to suppress nuclear spin fluctuations in quantum dots
	Promotor:	Prof. dr. H. Bluhm
	Sc. assistant:	Simulations and development of high frequency chips for GaAs singlet-triplet qubits
	Supervisor:	Prof. dr. H. Bluhm
	Msc. Thesis:	Tuneable Long Range Interactions in an Array of coupled Cooper Pair Boxes
	Promotor:	Prof. dr. F. Hassler
2013–2017	PhD. in Physics Delft University of Technology, Delft Netherlands	
	Thesis:	Creation and Detection of Majorana states
	Supervisor:	Prof. dr. A. Akhmerov

LIST OF PUBLICATIONS

1. Stefanie Tenberg, Robert P.G. McNeil, Sebastian Rubbert, Hendrik Bluhm, *Narrowing of the Overhauser field distribution by feedback-enhanced dynamic nuclear polarization*, Phys. Rev. B 92, 195428 (2015).

2. Daniel Otten, Sebastian Rubbert, Jascha Ulrich, Fabian Hassler, *Universal power-law decay of electron-electron interactions due to nonlinear screening in a Josephson junction array*, Phys. Rev. B 94, 115403 (2016).

3. S. Rubbert, A. R. Akhmerov, *Detecting Majorana nonlocality using strongly coupled Majorana bound states*, Phys. Rev. B 94, 115430 (2016).

4. M.C. Cassidy, A. Bruno, S. Rubbert, M. Irfan, J. Kammhuber, R.N. Schouten, A.R. Akhmerov, L.P.Kouwenhoven, *Demonstration of an ac Josephson junction laser*, Science 355, 939 (2017).